Fast Ion Dynamics in ASDEX Upgrade and TEXTOR Measured by Collective Thomson Scattering

Moseev, Dmitry; Korsholm, Søren Bang; Meo, Fernando

Publication date:
2011

Document Version
Publisher's PDF, also known as Version of record

Fast Ion Dynamics in ASDEX Upgrade and TEXTOR Measured by Collective Thomson Scattering

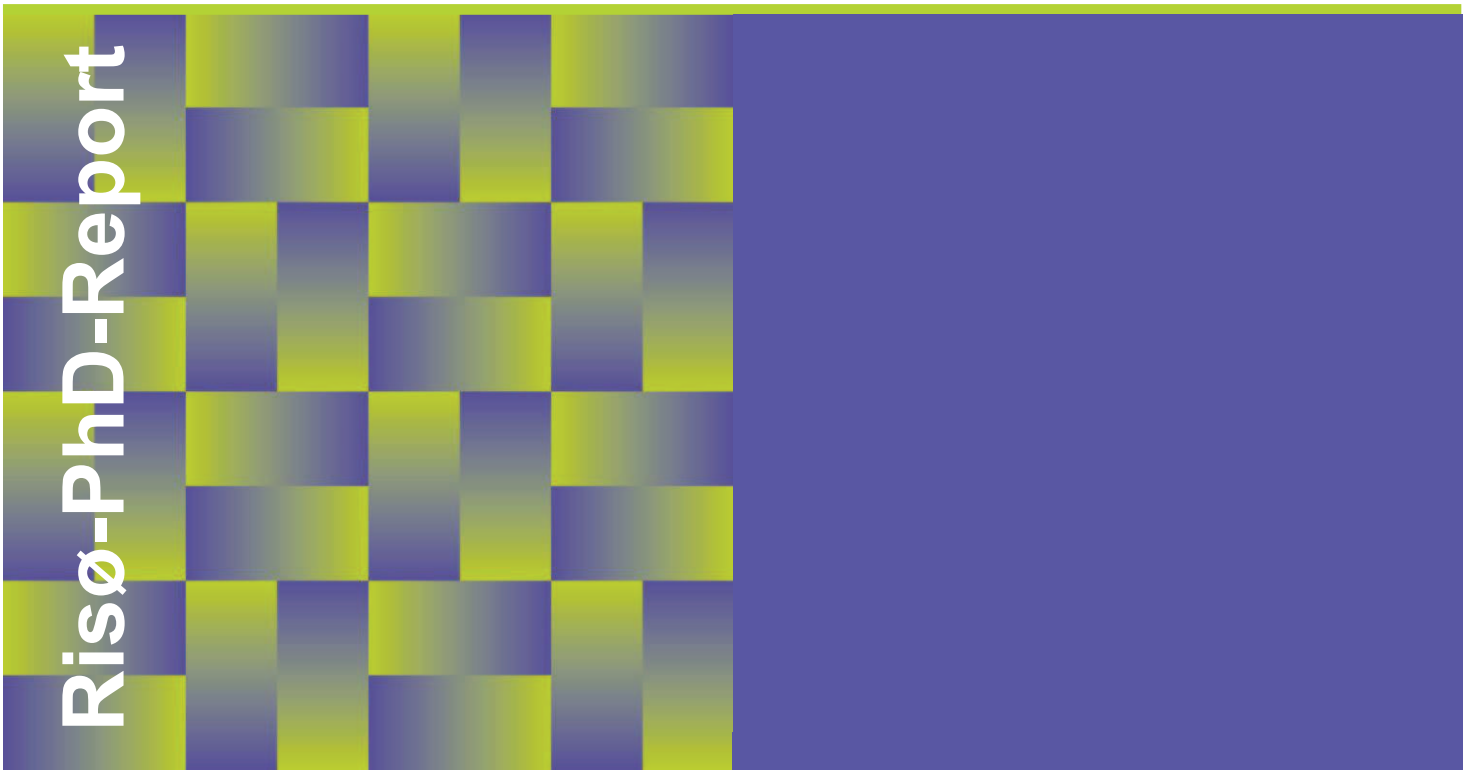

Risø DTU
National Laboratory for Sustainable Energy

Dmitry Moseev
Report number Risø-PhD-91
Publication date November 2011

Author: Dmitry Moseev
Title: Fast Ion Dynamics in ASDEX Upgrade and TEXTOR Measured by Collective Thomson Scattering
Division: Plasma Physics and Technology Programme

Abstract:
Fast ions are an essential ingredient in burning nuclear fusion plasmas: they are responsible for heating the bulk plasma, carry a significant amount of plasma current and moreover interact with various magnetohydrodynamic (MHD) instabilities. The collective Thomson scattering (CTS) diagnostic is sensitive to the projection of fast ion velocity distribution function. This thesis is mainly devoted to investigations of fast ion physics in tokamak plasmas by means of CTS.

Report number Risø-PhD-91
Publication date November 2011

ISSN 0106-2840
ISBN 978-87-550-3958-2

Contract no.:

Group's own reg. no.:
(Føniks PSP-element)

Sponsorship:

Contents

Chapter 1

Foreword

This thesis represents the work which was carried out in the course of three years of my PhD studies at Risø DTU. It would have not been possible to finish the work without help of my supervisors, Søren Bang Korsholm and Fernando Meo. I could always get an advice and discuss any technical, experimental or physical difficulties with any member of the CTS group: Henrik Bindslev, Vedran Furtula, Frank Leipold, Poul Kerff Michelsen, Stefan Kragh Nielsen, Morten Stejner Pedersen, and Mirko Salewski. I am especially grateful to Mirko for his extensive help in reviewing my scientific texts. I would also like to express a lot of gratitude to John Hammer Holm, Martin Jessen, Søren Robert Nimb, Nina Bendix, Connie Munch Westergaard and to the head of the PLF program Jens Juul Rasmussen.
The author is grateful to Valentin Igochine from IPP Garching for support and fruitful discussions. It was a big pleasure to work with Tuomas Koskela and Otto Asunta from Aalto University, and with Mattia Albregante from EPFL on the comparison of the CTS measurements with the ASCOT and VENUS codes. The experiments, which this thesis is based on, would not be possible without help of the TEXTOR and ASDEX Upgrade teams. I got a lot of assistance from the ECRH teams from FOM and IPP Garching. A lot of support was given by my wife Susanne, who was always very patient and encouraging.

1.1 Introduction

Nuclear fusion is foreseen as a vital source of energy in the context of scarcity of fossil fuels and pollution of the environment. The research on magnetically confined high temperature plasmas, where fusion is supposed to take place, started more than 50 years ago. Presently the first experimental fusion reactor, ITER, is under construction in Cadarache, France. In fusion plasmas, supra-thermal particles, particularly ions, play an important role. They are responsible for plasma heating, damping and destabilizing instabil-

ities, and are crucial for advanced scenarios with non-inductive generation of plasma current in tokamaks. However, the physics of energetic ions is not completely understood. This dissertation is mainly devoted to the fast ion results obtained by means of the collective Thomson scattering diagnostic at the TEXTOR and ASDEX Upgrade tokamaks during the author's PhD studies at Risø DTU. Further development of the CTS diagnostic is also discussed in the thesis.

Chapter 2 gives background information on plasma physics necessary for reading the rest of the thesis, principles of the CTS diagnostic, and the current stage of fast ion research. Chapter 3 gives a brief description of the TEXTOR and ASDEX Upgrade tokamaks, including a description of the CTS diagnostics at these machines. Methodology of the CTS measurements, as well as preparatory steps for the experiments are explained in chapter 4. Recently published results from the CTS group with contributions from the PhD work, are highlighted in chapter 5. Chapter 6 is dedicated to a comprehensive comparison of the measured fast ion velocity distribution function by CTS in the TEXTOR tokamak at different radial locations and resolved angles with Monte Carlo simulations. Experiments on investigation of the influence of resonant magnetic perturbations on fast ion confinement are described in chapter 7. Fast ion induced instabilities, detected and characterized by the CTS diagnostic at TEXTOR, is presented in chapter 8. Experiments on sawtooth destabilization by means of electron cyclotron current drive, in which author participated apart form the CTS activities, are described in chapter 9. Section 1.2 explains what the personal contribution of the author to the presented research is.

1.2 Personal Contribution of the Author

The author participated in all CTS activities of the group in the course of his PhD training. In Section 2.4 the author was involved in some of the derivations. The diodes, described in Section 3.2 were characterized by the author. He participated in the alignment of the ASDEX Upgrade CTS transmission line (Section 4.1), developed a technique for post factum elevation alignment check at TEXTOR described in Section 4.3. He performed the feasibility analysis of the hot source calibration with SiC (Section 4.4.1) and developed programs for cross-calibration of the TEXTOR CTS receiver with incoherent Thomson scattering and cross-calibration of the ASDEX Upgrade CTS receiver with the ECE diagnostic (Section 4.4.2). The author took part in investigations of the origin of the secondary emission signal in the CTS spectra (Section 4.5).
In the experiments on strong scattering of the electromagnetic radiation (Section 5.1) the author operated the diagnostic during a part of the cam-

paign. In the section devoted to the comparison of the ASDEX Upgrade results to the Monte Carlo simulations (Section 5.3), the author was involved in the discussion and participated in the conduction of the experiments. For the fuel ion ratio measurements (Section 5.4), the author participated in the diagnostic upgrade described in Section 3.5, experimental planning and conduction of the experiment. In the experiments on fast ion redistrinbution due to sawteeth, the author was operating the diagnostic and participated in the physics discussion (Section 5.2). Normally, during the course of campaigns, the author was in charge of operating the steerable mirrors, as well as finding the scattering geometries by means of the ray-tracing code described in Section 4.2.
Experiments, described in chapter 6 were planned primarily by the author. He was also in charge of the data analysis and coordination between the CTS, ASCOT, and VENUS groups. The author wrote the paper [1]: "Comparison of measured and simulated fast ion velocity distributions in the TEXTOR tokamak", *Plasma Physics and Controlled Fusion*, 2011. Experiments, described in chapter 7 were also planned and primarily analysed by the author. Even though they were inconclusive regarding their main objective, valuable experimental data necessary for the previous chapter were obtained. The experiments described in chapter 8 were partly designed (together with M. Stejner) and analysed by the author. Future experiments on the topic, which are described in the chapter, are coordinated by the author. The author's contribution to the experiments, described in chapter 9 was in discussion, ECCD profiles calculations with the TORBEAM code and in data analysis.
During the PhD studies, the author participated in three EPS conferences, and in a DFS (Danish Physical Society) conference. He became a co-author of 13 journal publications.

List of Acronyms

CTS	Collective Thomson scattering
ECCD	Electron cyclotron current drive
ECE	Electron cyclotron emission
ECRH	Electron cyclotron resonance heating
ICE	Ion cyclotron emission
ICRH	Ion cyclotron resonance heating
LH	Lower hybrid
MHD	Magnetohydrodynamics
NBI	Neutral beam injection
SPD	Spectral power density
(T)AE	(Toroidicity induced) Alfvén eigenmode
VCVA	Voltage controlled variable attenuator

List of Symbols

$\mathbf{B}$	Magnetic field
$\mathbf{E}$	Electric field
E	Energy
I_p	Plasma current
$\mathbf{k}$	Wave vector
$\mathbf{k}^i$	Wave vector of incident radiation
$\mathbf{k}^s$	Wave vector of scattering radiation
$\mathbf{k}^\delta$	Resolved fluctuation wave vector
m	Mass
m	Poloidal mode number
n	Toroidal mode number
$n_{i,e}$	Ion/electron density
O_b	Beam overlap
p	Pressure
P^i	Incident power
q	Safety factor
q_e	Electron charge
R	Tokamak radial coordinate
r_e	Classical electron radius
$T_{i,e}$	Electron/ion temperature
v	Velocity
v_A	Alfvén velocity
Z	Particle charge, in elementary charges
z	Tokamak vertical coordinate
α	Salpeter parameter
Γ	Flux
ϵ	Dielectric tensor
ϵ_0	Vacuum permittivity
λ_D	Debye length
λ	Wavelength
μ	Magnetic moment
μ_0	Vacuum permeability
Σ	Scattering function
σ	Standard deviation
σ	Conductivity
ϕ	Toroidal angle
ϕ	Projection angle, $\angle(\mathbf{k}^\delta, \mathbf{B})$
Ω_c	Cyclotron angular frequency
ω^i	Angular frequency of incident radiation
ω_p	Plasma angular frequency
ω^s	Angular frequency of scattering radiation
ω^δ	Angular frequency of resolved fluctuations

Chapter 2

Background

Energy consumption grows rapidly worldwide. It is seen from Fig. 2.1, that even in the most optimistic scenario the demand in energy will double in one century. At the same time, due to environmental problems, it is unwise to increase the consumption of fossil fuels. Renewable energy is developing very fast but the sources of it are intermittent. Transition to intermittent energy sources requires major investments in the infrastructure. Fission power plants can in principle satisfy increasing demands but other problems arise. The biggest one is radioactive waste treatment since there is no proper technology on how to recycle the waste or depose it. Inherent in the nuclear fission process, the chain reaction can go out of control, is in itself of a great concern (e.g. Chernobyl disaster in April 1986). However, nuclear fusion could be one of the solutions to the global energy problem.

2.1 Nuclear Fusion

Nuclear fusion is a process where two light nuclei fuse together and create a heavier one. In cases when the product of fusion is lighter than iron, energy is released from the reaction. In order to achieve it, one should bring nuclei close enough to overcome the Coulomb (potential energy) barrier. For instance, during the formation of a star, interstellar gas is compressed and confined by the gravitational field. Gas heats up due to compression and two nuclei can be close enough to each other so that the nuclear fusion process happens. If a sufficient part of energy from fusion is confined, the reaction becomes self-sustainable. When a gas heats up to high temperature, its atoms start loosing electrons and the gas becomes ionized. This ionized quasineutral gas is called *plasma*.
A fusion reaction between deuterium and tritium has the largest potential for implementation in a power plant due to a large cross-section at relatively low energies:

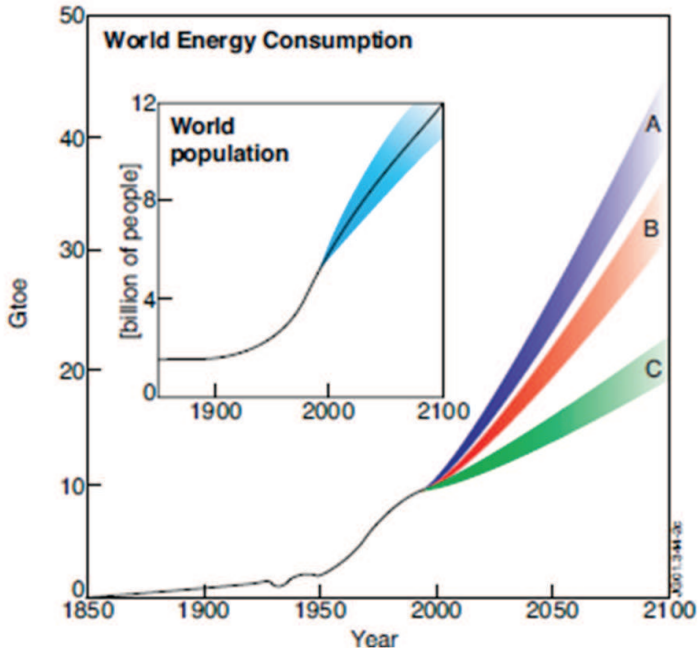

Figure 2.1: World energy consumption in Giga tonnes of oil equivalent per annum, forecast for the XXI century [2]. Curves **A** - **C** represent different models

$$D + T \rightarrow {}^4He + n + 17.6\,\mathrm{MeV}$$

Energy released in the reaction is distributed between ^{4}He nuclei (so called α-particle) and a neutron according to the energy and momentum conservation laws, i.e. 3.5 MeV carried by the α-particle and 14.1 MeV by the neutron. The D-T fusion reaction is characterized by a very large energy gain per mass of reacting species. Comparison of the average fuel consumption of power plants running on different types of fuel with a future nuclear fusion reactor is shown in Table 2.1. Taking into account the amount of deuterium in water (one part of heavy water in 1600 parts of light water) and crude material for tritium (lithium) the D-T nuclear fusion reaction is provided with practically infinite amount of fuel.. Tritium needs to be produced out of lithium because tritium is a radioactive isotope with half-life of 12.6 years, so it does not exist on Earth.
In order for a fusion reactor to reach ignition, i.e. the state when the reaction becomes self-sustainable, the so called Lawson criterion [4] should be fulfilled. The Lawson criterion for the D-T fusion reaction is shown in Eq. (2.1):

$$n_e \cdot T \cdot \tau_E \geq 10^{21}\,\mathrm{keV} \cdot \mathrm{s/m^3}\,, \tag{2.1}$$

Method	Annual fuel consumption for a power plant of 1000 MW of electricity
Coal	$2.7{\cdot}10^6$ tonnes
Oil	$1.9{\cdot}10^6$ tonnes
Nuclear fission (if breeder technology is employed)	28 tonnes of UO_2
Nuclear fusion	100 kg of D_2 and 150 kg of T_2

Table 2.1: Annual fuel consumption for a power plant of 1000 MW el. Data for the table are taken from reference 3

where n_e is electron density of plasma in m^{-3}, T is temperature of reacting species in keV and τ_E is energy confinement time in s.
Maximum cross-section for this reaction is achieved at the centre of mass kinetic energy of reacting species at around 80 keV. Such energies can be achieved in accelerators. Due to the low efficiency, accelerator fusion was left behind the scope of fusion research already in 1950's. Uncontrolled nuclear fusion was achieved in 1952 with the first hydrogen bomb. An explosive type of reaction is difficult to use for electricity production, even though so called inertial confinement is a very active field of research [5].
So far magnetic confinement of high-temperature plasmas looks like the most promising method to produce net energy from the nuclear fusion reaction.

2.1.1 Magnetic Confinement of Plasma

The concept of magnetic confinement of plasma in a magnetic field is based on the fact that charged particles move freely along the magnetic field whereas movement across the magnetic field is restricted. The first experiments on magnetic confinement of plasma were made on the linear devices called Θ - and Z - pinches. In these cylindrical devices, the plasma is confined by the magnetic field generated by external coils or by electrical current running through the plasma. These devices significantly improved understanding of plasma physics. However, due to extremely high losses along the magnetic field lines, good confinement was not possible.
Initially, magnetic mirrors were suggested for reducing particle loss from the open ends. In the machines with magnetic mirrors, the magnetic field in the centre is lower than at the open ends. If a magnetic field varies slowly, the magnetic moment of particles is conserved, thus particles which have a ratio between parallel and perpendicular velocities to the magnetic field direction which is low enough are reflected from magnetic mirrors at the ends of the device, while other particles can leave the confinement volume. The critical ratio between parallel and perpendicular velocities create a cone of losses, i.e. the cone in velocity space which determines a velocity boundary be-

tween confined and lost particles. However, due to collisions there is always a steady transport of particles into the cone of losses. Moreover, strongly anisotropic distribution function creates a number of kinetic instabilities which increase particle transport. Finally, magnetic mirror devices are not considered as a possible prototype of a future fusion reactor, although they are still used for research purposes.
Another way of avoiding problems with open ends of the pinch devices is to bend the device and connect open ends. The improved design is called a magnetised torus. For convenience, physical processes in the torus are usually described in toroidal coordinates. The illustration of it is presented in Fig. 2.2. Despite of a significant improvement, the confinement time in the magnetised torus is still very short. This is due to the fact that the magnetic field lines are bent in toroidal geometry (only toroidal field is present). In this case electrons and ions experience curvature and gradient drifts, which are described by Eq. (2.2) and Eq. (2.3):

$$\mathbf{V}_R = \frac{mV_{||}^2}{qB}\frac{\mathbf{R_c}\times\mathbf{B}}{R_c^2 B} \tag{2.2}$$

$$\mathbf{V}_{\nabla B} = \frac{mV_{\perp}^2}{2qB}\frac{\mathbf{B}\times\nabla B}{B^2} \tag{2.3}$$

where $\mathbf{V}_R$ and $\mathbf{V}_{\nabla B}$ are drift velocities, $V_{||}$ and $V_{\perp}$ are velocities of a particle along and perpendicular to the magnetic field, respectively; q is the electrical charge of the particle, $\mathbf{R_c}$ is a curvature radius of the magnetic field line. The drift velocity depends on many parameters, particularly electrical charge of the particle and its sign. It means that these drifts will result in charge separation and finally an electric field builds up. The electric field leads to the $E \times B$ drift (Eq. (2.4)):

$$\mathbf{V}_{E\times B} = \frac{\mathbf{E}\times\mathbf{B}}{B^2} \tag{2.4}$$

where $\mathbf{V}_{E\times B}$ is a drift velocity. The $E \times B$ drift is charge-independent and ejects the plasma from the confinement volume, as illustrated in Fig. 2.3. Due to the difference of transport coefficients in direction parallel and perpendicular to the magnetic field (the coefficients are much higher along the magnetic field lines), introducing a helical topology of the magnetic field lines would short-cut the charged regions and this problem will be mitigated.

2.1.2 Tokamaks and Stellarators

Currently there are two major approaches of creating a helical configuration of magnetic field lines (reversed field pinches are not discussed here). One of

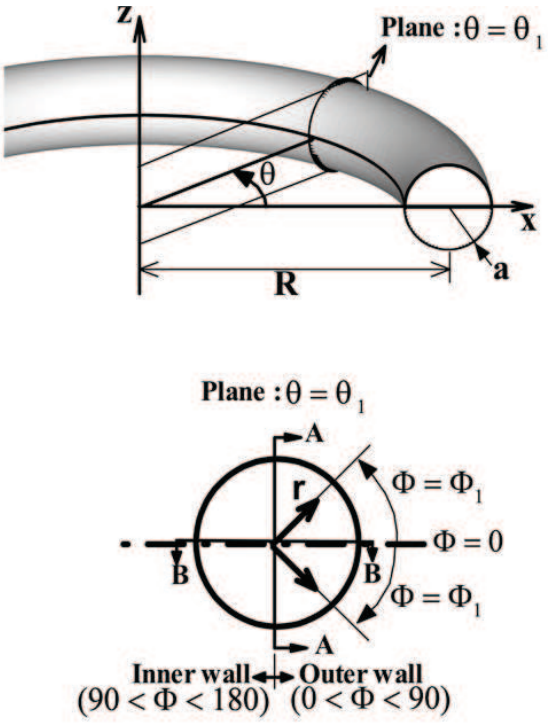

Figure 2.2: Sketch explaining the notations in toroidal geometry. Θ angle is called a toroiadal angle, Φ angle is called a poloidal angle. Plain $\Theta = const$ is called a poloidal plain. Illustration is taken from www.emeraldinsight.com.

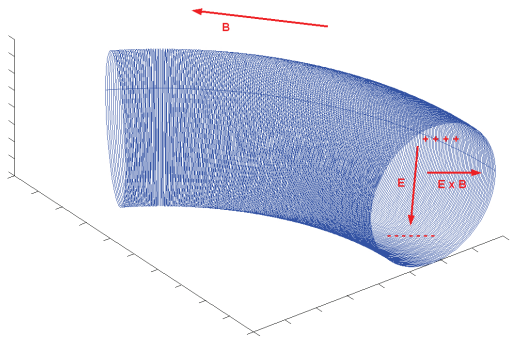

Figure 2.3: A sketch of the drift occurring in the magnetised torus due to the curved magnetic field lines

them was introduced by L. Spitzer in the 1950's. In this concept, the helical transformation of the magnetic field lines is created by external coils. Indeed, stellarators improved confinement a lot compared to magnetized tori or devices with magnetic mirrors. However, stellarator operations showed that plasma confinement is very sensitive to tolerances in the magnetic coils production and accuracy of magnetic field calculations in the stage of design. This fact slowed down the development of stellarators.
Another alternative concept is the tokamak, suggested in 1955 by I. Tamm and A. Sakharov. In tokamaks, the poloidal magnetic field is created by the induction current from a central solenoid or by other non-inductive currents propagating in the plasma in the toroidal direction, as it is illustrated in Fig. 2.4. This configuration is more stable and tolerant to uncertainties in the design and manufacture. Despite the advantages, there are many complicated problems. The first challenge is plasma heating. This is a general difficulty for all machines with magnetic confinement. The intended heating scenario for tokamaks initially included only ohmic heating. It was believed that it would be sufficient to reach fusion-relevant parameters. However, it was impossible to achieve necessary temperatures because efficiency of ohmic heating is decreasing with increase of temperature: $\sigma \sim T_e^{1.5}$, where σ is conductivity and T_e is electron temperature. Stellarators do not have ohmic heating because the poloidal magnetic field is created by external coils, therefore plasma current would strongly perturb the equilibrium magnetic field topology. Thus, auxiliary heating methods have been developed: electron-cyclotron resonance heating (ECRH), ion-cyclotron resonance heating (ICRH), lower-hybrid heating, neutral beam injection (NBI), and even adiabatic magnetic compression. The latter one did not show a significant results and presently is not used. Secondly, electrical current in tokamaks is generated by induction. This means that the current which flows through the solenoid should always increase in order to keep plasma current at constant level. It imposes a limitation on the duration of the discharge, which makes it difficult to use tokamaks as future fusion power plants working in a steady-state regime. Non-inductive operation scenarios when plasma current is generated by means of injection of electromagnetic waves and NBI are actively studied now.

Stability of plasma in any magnetic configuration is a big challenge which has faced the whole area of research for the last half a century. Enormous effort is put in understanding physical mechanisms of various instabilities. Another key topic is the feedback control of plasmas and controlled plasma shutdowns in order to prevent machines from damage due to disruptions. However, there are a lot of phenomena which still have no clear physical interpretation and no method of how to deal with these events. Helicity of the magnetic field is of a crucial importance for plasma stability and is often described by the *safety factor*, which is denoted by q in the litera-

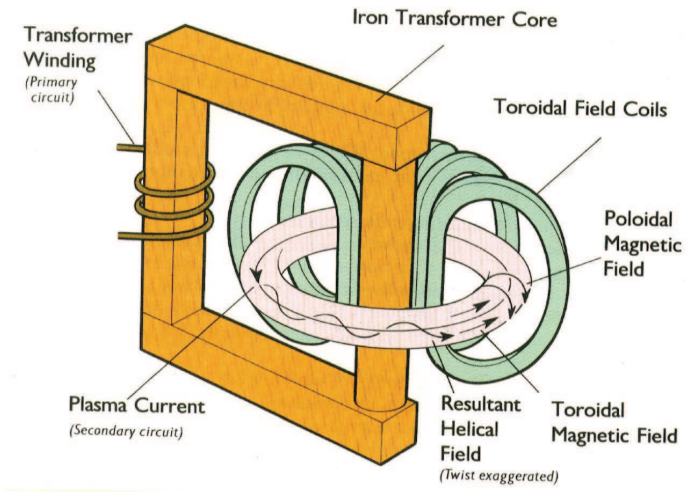

Figure 2.4: A schematic which shows a principle of poloidal magnetic field generation in tokamaks. Illustration is taken from http://woodruffscientific.com.

ture. The safety factor describes how many times the magnetic field line turns toroidally until it makes one poloidal turn. In toroidal geometry, an expression for the safety factor is:

$$q = \frac{B_t}{B_p}\frac{r}{R} \tag{2.5}$$

Here B_t and B_p are toroidal and poloidal magnetic fields, respectively; r and R are minor and major radii, respectively. Normally, q-values are irrational, which means that the magnetic field line never closed on itself. The length of magnetic field line is infinite in this case and it will create a magnetic surface. At some particular radii and magnetic field values the value of q is a rational number, which means that length of the magnetic field line is finite. It allows resonances of various magnetohydrodynamic waves. Thus, at radii with rational values of the safety factor, instabilities are more likely to happen.

2.2 Fast Ion Physics

In fusion plasmas fast ions (i.e. ions with non-Maxwellian distribution function and energies much higher than thermal) account for about 1% of the total amount of particles. At the same time, the fast ion pressure is around 10% of the total pressure, they also carry a significant amount of current and influence the formation of the q-profile. Thus fast ion physics is of crucial importance for fusion plasmas in general and particularly for future

ITER operation. Understanding of the behaviour of fusion-born α-particles in ITER is very important for achieving burning conditions. In this sense current fast ion research with anisotropic fast ion distribution function acts as an important building block for successful ITER operation.
Fast ions in present-day tokamaks and stellarators may originate from several sources. Firstly, nuclear fusion itself should be emphasised. In supershots in TFTR (plasma discharges in D-T gas mixture) and during the D-T campaign on JET, a significant fusion yield was achieved, resulting in a large amount of alphas [6–8]. High frequency heating at ion cyclotron or lower hybrid range of frequencies provides particles with MeV energies [9]. Neutral beam injection (NBI) produces fast ions with energies of up to approximately 100 keV. This is an energy limit for injectors whose operation is based on acceleration of positive ions, therefore a new generation of injectors based on negative ions is being developed [10–12]. Fast ions originating from various sources posses qualitatively different distribution functions. Fusion-originated α-particles are born with fixed energy and expected to have isotropic distribution of velocities at birth. Energetic particles which originate from ICRH exhibit a different behaviour. They are steadily accelerated by resonant interaction with a wave. ICRH-accelerated particles typically have very large velocities in the direction perpendicular to the magnetic field and stay at trapped orbits (when the perpendicular velocity of a fast ion is too high compare to parallel, and the particle is reflected from regions with stronger magnetic field), i.e. similar to particles in mirror devices they cannot penetrate into the regions with high magnetic field, thus being reflected.
Over the years, there are a number of diagnostics developed for fast ion measurements, e.g. fast ion D_α spectroscopy [13,14], γ-ray spectroscopy [15,16], neutral particle analysers (NPA) [17,18], scintillator probes (FILD) [19–21], neutron spectroscopy [22], and collective Thomson scattering (CTS) diagnostic [23–27].
Fast ion research over the last decade concentrated on following topics:

- Fast ion losses due to toroidal magnetic field ripples (so-called ripple losses)
- Energetic particle interaction with low-frequency MHD instabilities
- Fast ion interaction with resonant Alfvén waves
- Turbulent transport of fast ions

A brief literature survey on the highlighted topics is presented below.

2.2.1 Fast Ion Losses Due to Toroidal Magnetic Field Ripples

The toroidal magnetic field in tokamaks are created by external coils which are installed around the torus. There are typically 15 - 30 toroidal field coils

installed in a machine [28]. Due to the discrete number of coils, the toroidal magnetic field is inhomogeneous. The degree of inhomogeneity is described by a ripple amplitude:

$$\delta = \frac{B_{max} - B_{min}}{B_{max} + B_{min}} \tag{2.6}$$

Ripple-induced diffusion of fast ions depends on the energy of ions, on pitch to the magnetic field ($p = v_{||}/v$, where $_{||}$ denotes a component parallel to the magnetic field. It is often expressed in degrees and then called a pitch angle), and on ripple amplitude [29, 30]. Ripple magnitude for instance on JET which is equipped with 32 toroidal coils is in the order of one percent at the outboard limiter. Experiments on fast ion losses due to ripples were conducted at JET [31]. In some of the discharges 16 out of 32 toroidal field coils are switched off in order to increase a ripple magnitude at the outboard limiter by a factor of 10. An influence of the ripple on energetic particles in the range of 100 keV - 3 MeV have been studied. In NBI-heated discharges plasma rotation drops from 10^5 m/s down to undetectable values. A strong correlation between fast ion losses from the ripple cone due to pitch angle scattering and drop of total stored energy in plasma by 30% and reduction in ion heating is observed. The confinement of ICRH-accelerated fast ions reduces if the ICRH resonance layers are moved towards the low field side. The ripple losses are also detected in Tore Supra [32], TFTR [33], and JFT-2M [34–36]. The JFT-2M team found that insertion of ferritic steel boards reduces the amplitude of the ripples significantly [34–36]. Such insertions will be used in ITER in order to improve the fast ions confinement and reduce heat load on the first wall components. Simulations predict that the use of the ferritic insertions will lead to a reduction of fast ion related heat loads from 0.8 MW/m^2 down to approximately 0.025 MW/m^2, when the acceptable value would be 0.1 MW/m^2 [37].

2.2.2 Energetic Particle Interaction with Fishbones

In the early 80s (in PDX [38]) it was found that fast ions from NBI could interact with core localized kink modes known as fishbones. An example of the fishbone instability is shown in Fig. 2.5. Both theoretical and experimental works concluded that the resonant interaction of fast ions with MHD modes at low sub-Alfvénic frequency is possible. Fast ions which interact with such modes have energies in sub-MeV range. Thus no problems for fusion plasmas were foreseen.

Fishbone instability causes large losses of fast ions. The energy of lost energetic particles depends on the amplitude of fishbones. For small amplitudes the fast ion losses on PDX were detected (by NPA) at energies between full and a half of injection energy of NBI. For large amplitude oscillations, the losses were detected for particles with energies from as low as thermal and up to $1.5E_{inj}$, where E_{inj} is injection energy of NBI. Detection of a flux of

particles with energies that exceed the injection energy of NBI suggesting some mechanism that accelerates particles. Recent experiments at JET [39]

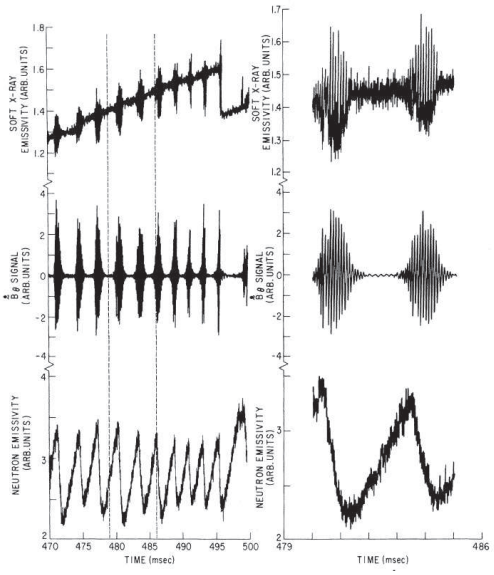

Figure 2.5: Evolution of soft X-ray signal (top), $\dot{B}_\theta$ (middle) from the coil next to the outer wall of the PDX machine, and neutron flux (bottom). Signal during two fishbones is zoomed in and shown on right side of the graph. Figure is taken from reference 38.

have shown that ICRH-accelerated protons with MeV energies are lost due to non-resonant interaction with fishbones induced by 130 keV NBI. Results obtained with FILD showed that lost ions originated from trapped orbits. Simulations made with the HAGIS code [40] showed that another source of lost ions was counter passing protons in the plasma centre which change to the unconfined orbits due to orbit stochastisation.

2.2.3 Energetic Particle Interaction with Sawtooth

In addition to fishbones, fast ions strongly interact with the sawtooth instability. On one hand, sawteeth redistribute and eject fast ions from inside of the plasma core which decreases fusion yield (see Fig. 2.6 for example). On the other hand fast ions may stabilize the sawteeth. The stabilization leads to so-called monster sawteeth - crashes of enormous size which often trigger neoclassical tearing mode and possibly lead to a disruption. Experiments on sawtooth instability are discussed in chapters 5 and 9 in this thesis, therefore a more coherent description of the background knowledge is necessary.

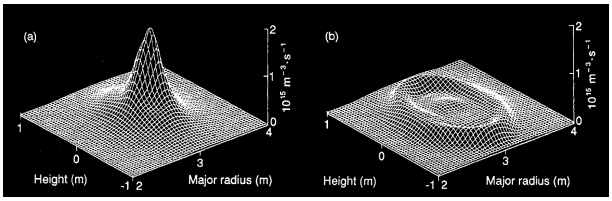

Figure 2.6: Neutron emissivity profile right before (a) and after the sawtooth crash in JET. Figure is taken from reference 17.

2.2.4 Theory of Sawtooth Instability

The sawtooth oscillations were first observed in 1974 as a sudden drop in core temperature and density and expelling them outside the magnetic surface with $q = 1$ [41]. Core temperature and density recover slowly until the next event takes place which looks like sawtooth, hence the name. The sawtooth oscillations are caused by reconnection event at the $q = 1$ magnetic surface [42]. The first theory of sawtooth oscillations was developed by B. Kadomtsev [42–44]. According to electron temperature and density measurements, their profiles are peaked in the plasma center, thus the current density profile has even more peaked shape because plasma conductivity $\sigma \propto T_e^{1.5}/n_e$. Sharp gradient of the current density makes plasma unstable against a kink mode with $(m, n) = (1, 1)$. According to Kadomtsev, magnetic reconnection takes place on the low field side of the $q = 1$ surface. An island starts growing inside the $q = 1$ surface, making the temperature, density and current density profiles flat, thus demolishing the source of free energy. The safety factor in the plasma center becomes flat after the crash and equal to unity $q(0) = q(r_{inv}) = 1$. An illustration of Kadomtsev model is shown in Fig. 2.7. A big advantage of this theory is that it is very intuitive. However, many experiments showed contradictory results. Firstly, the spontaneous onset of the sawtooth is not explained. According to Kadomtsev, the kink mode should have a growth rate which is rather small in the beginning of the sawtooth cycle so that the instability emerges slowly and is visible by diagnostics. However, very often sawtooth oscillations appear spontaneously without any precursor. Secondly, the safety factor in the plasma core never relaxes back to unity [45, 46]. The sawtooth crash time is typically in the order of 0.1 ms which is typically three orders of magnitude less than Sweet-Parker time (time needed for resistive reconnection of magnetic field lines, around 10 ms for typical tokamak parameters). That is because in collisionless plasmas thermal conductivity and electron diffusivity in the case of reconnection are in the order of parallel thermal conductivity and diffusivity [47]. Pressure gradient decreases to almost zero values during the crash time and the source of free energy for the kink instability vanishes. Kadomtsev's model predicts that the reconnection region would

appear at the low field side of the $q = 1$ surface, but the electron cyclotron emission (ECE) imaging measurements in TEXTOR showed that the reconnection region is likely to appear on both low and high field sides [48]. The sawtooth crash takes place when changes in the mode potential energy δW reaches a critical value δW_{cr} [49]. The following effects contribute to δW:

$$\delta W = \delta W_{MHD} + \delta W_{KO} + \delta W_{fast} \tag{2.7}$$

Where δW_{MHD} is the ideal MHD term and includes effects due to particular geometry of the plasma, δW_{KO} is so-called Kruskal-Oberman term which accounts for collisionless thermal trapped particle, δW_{fast} takes potential energy changes due to fast ions into account.

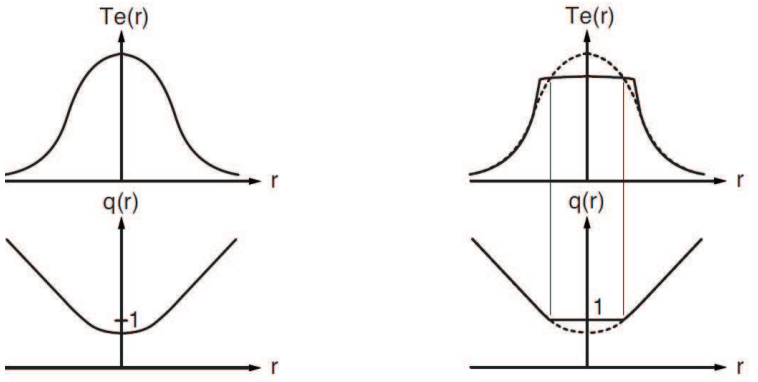

(a)

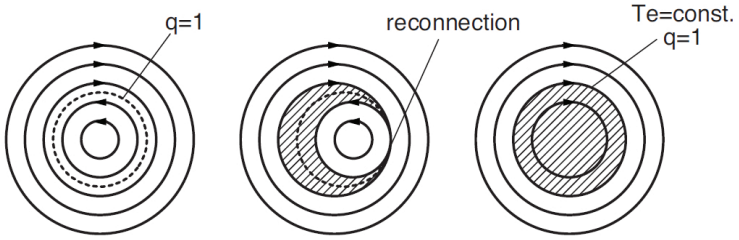

(b)

Figure 2.7: Illustration of the theory of sawtooth crash according to Kadomtsev [43]. (a) Sketch of T_e and q evolution during the sawtooth crash; (b) Sketch of reconnection process, illustrating Kadomtsev's theory. Figure is taken from reference 47.

2.2.5 Fast Ion Interaction with Resonant Alfvén Waves

Alfvén waves play a very important role in the plasma physics. This section briefly describes an interaction between Alfvén waves and energetic ions. Two topics of fast ion physics are of particular interest in conjunction with Alfvén waves. These are the drive of the instability and fast ion losses due to them. Frequency of the instability may vary from very low values and up to harmonics of ion cyclotron frequency. Low frequency instabilities are typically driven by fast ion pressure gradients [50], and the high frequency modes are typically excited by gradients in velocity space of fast ion distribution function [51]. In order for the wave to be excited, the total fast ion related growth rate should overcome total damping from thermal electrons and ions, as well as damping from fast ion component of the distribution function. It was shown in reference 52 that fast ions may excite Alfvén waves at sub-Alfvénic velocities, particularly when $v_{||} \approx 0.3 v_A$.
Fast ions strongly interact with shear Alfvén waves. Losses could be both diffusive and convective, it is illustrated in Fig. 2.8. It is clearly visible that incoherent fast ion losses measured with FILD scale quadratically with the amplitude of the toroidicity induced Alfvén eigenmode (TAE) n = 5 magnetic fluctuations. This proves the diffusive character of the losses. However, coherent losses are mainly convective which is shown by a linear dependence between fast ion losses measured with FILD and the MHD amplitude at TAE n = 3 frequency. The n = 3 mode exists in the experiment at much higher frequency than the mode of n = 5. Moreover, at the time when n = 3 mode is detected, activity at neighbour frequencies is observed. One can read more in reference 53 and in the review in reference 37. The rate of fast ion losses are strongly related to their gyroradii [54]. Reversed shear Alfvén modes which appear in the start-up phases in modern tokamaks and are relevant to advanced scenarios in ITER are discussed in details in reference [55].
Future experiments on investigation of fast ion transport due to interaction with Alfvénic waves in ASDEX Upgrade were recently proposed. Using multi-diagnostic approach in fast ion measurements, the part of phase space (i.e. energy and pitch angle to the magnetic field) where the energetic particles resonate the wave is to be determined and compared with measurements by FILD on lost fast ions. Using CTS and FIDA systems at ASDEX Upgrade because they both measure a projection (CTS) or weighted projection (FIDA) of velocity distribution function of confined fast ions, the direction of the transport will be investigated, i.e. whether the transport is directed only outwards (from the Alfvén eigenmode radial location), or both inwards and outwards.

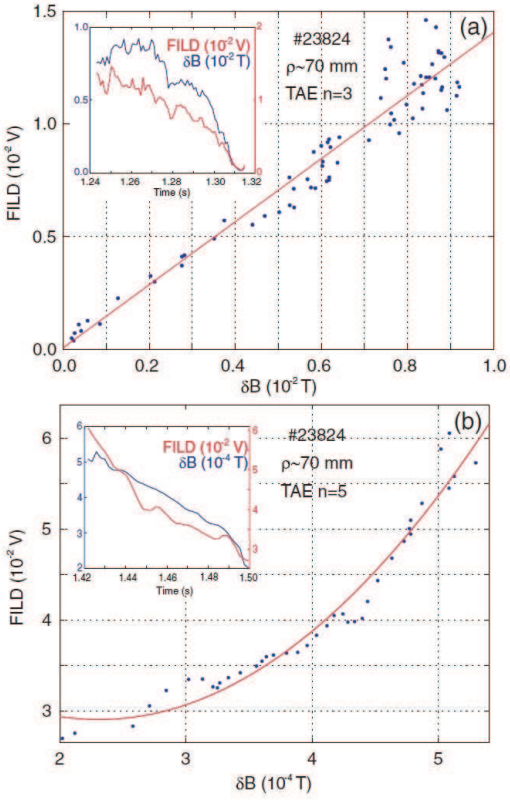

Figure 2.8: Fast ion loss rate in ASDEX Upgrade discharge 23824. (a) shows a dependence of coherent losses at TAE n = 3 frequency as a function of MHD amplitude; (b) depicts a dependence of incoherent losses on TAE n = 5 fluctuation amplitude. Figure is taken from reference 53.

2.2.6 Turbulent Transport of Fast Ions

Fast ion transport due to turbulence has recently been predicted theoretically, for instance in references 56–58. Two types of turbulence, electrostatic and magnetic, could affect fast ion transport differently [56]. Diffusion coefficient of fast ions due to electrostatic turbulence scales like $1/E$, where E is fast ion energy, with the fast ion energy, and it is also pitch-dependent. However, transport due to magnetic turbulence is not energy-selective and acts equally on all energetic particles, see Fig. 2.9.

Experimentally, an evidence of fast ion transport due to microturbulence

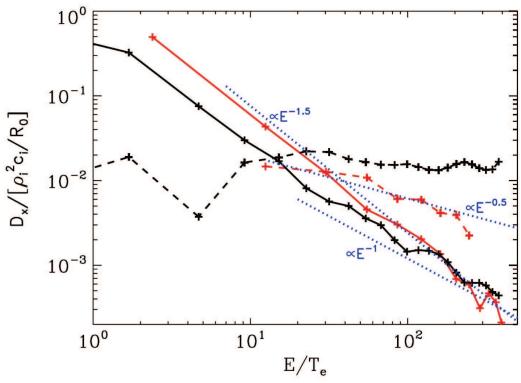

Figure 2.9: Fast ion diffusivity calculated with the GENE code. Solid lines show diffusivity for electrostatic turbulence for large (black) and small (red) values of pitch of fast ions to the magnetic field. Dashed line show diffusivity for magnetic turbulence. Figure is taken from reference 56.

was found at DIII-D [59]. There the fast ion diffusion diagnosed by FIDA, neutron spectroscopy and motional Stark effect is found to be higher in hotter plasmas and increases with minor radius. However, this is the only work where experimental evidence of turbulence-induced fast ion transport is shown. Experimental results from other machines are pending.

2.3 Principles of the Collective Thomson Scattering

Diagnostics of high temperature plasmas is limited to methods with no direct contact between equipment and a plasma. In this context methods involving electromagnetic waves play an important role in plasma diagnostics because plasma actively interact with them. Thomson scattering is elastic scattering of photons from free charged particles and is basically a low-energy limit of Compton scattering. In fusion research, two types of Thomson scattering diagnostics which measure various parameters of plasmas are used:

Incoherent Thomson Scattering

- Electron temperature
- Electron density

Collective Thomson Scattering

- Ion temperature
- Fast ion velocity distribution function
- Isotope content of plasmas

In both cases scattering is mainly originating from electrons. The reason being that the radiated power of the charged particle depends on the acceleration squared [60], i.e. $P_e \approx (m_i/m_e)^2 P_i$. Thus the direct contribution from ions is later neglected. Scattering of electromagnetic waves off free electrons is called Thomson scattering. In plasmas, electron fluctuations are correlated, thus scattering can be represented as a wave-mixing process where the wave of the scattered radiation is a mixing product of incident wave with fluctuations:

$$(\omega^s, \mathbf{k}^s) = (\omega^i + \omega^\delta, \mathbf{k}^i + \mathbf{k}^\delta) \tag{2.8}$$

where ω and $\mathbf{k}$ denote angular velocity and wave vector. Superscripts i, s, δ denote incident, scattering, and fluctuation in plasma, respectively. It is also sketched in Fig. 2.10. The regime of scattering is determined by the value of the Salpeter parameter (Eq. (2.9)), the ratio between the wavelength of the resolved fluctuations and the Debye length, $\lambda_D^2 = \frac{\epsilon_0 T_e}{n_e q_e^2}$ [61]:

$$\alpha = \frac{1}{k^\delta \lambda_D} \tag{2.9}$$

$\alpha \ll 1$ corresponds to incoherent Thomson scattering, $\alpha \gg 1$ corresponds to collective Thomson scattering. In tokamak plasmas, the difference between incoherent and collective Thomson scattering is determined by the frequency of incident radiation and the scattering angle. Using microwaves, there is a large flexibility in the choice of scattering geometries where the Salepeter parameter (see Eq. (2.9) is much greater than one.
Collective Thomson scattering is sensitive to fluctuations induced by fast ions in plasma. In a simple picture, background electrons tend to screen a perturbation of electric field induced by a fast ion. It creates a wake in a background electron distribution. Approximately, the frequency shift in the scattering radiation may be written as follows:

$$\Delta\omega \approx \mathbf{k}^\delta \cdot \mathbf{v}_{ion} \tag{2.10}$$

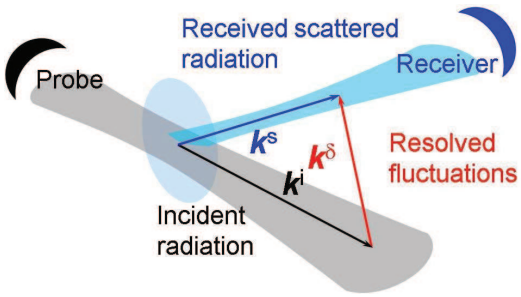

Figure 2.10: Scattering geometry of the CTS diagnostic. $\mathbf{k}^\delta$, $\mathbf{k}^\mathbf{i}$, and $\mathbf{k}^\mathbf{s}$ denote wave vectors of resolved fluctuations and of the incident and scattered waves, respectively. The blue ellipse at the intersection of the beams denotes the scattering volume.

Where $\mathbf{k}^\delta$ is a wavelength of resolved fluctuation and $\mathbf{v}_{ion}$ is fast ion velocity. In order to generate scattering field, the source currents in plasma must exist. The currents are created by the incident wave, which interact non-linearly with fluctuations in plasma (because of non-linearity of Vlasov equation [62]) and set up the third wave of scattering radiation. The source current in the cold plasma approximation is following [63]:

$$\begin{aligned} j_t^\sigma &= -\frac{i\omega^s\epsilon_0}{n^{(0)}}(\chi^s_{tl}(n^\sigma E^i_l + n^i E^\delta_l \\ &\quad +\epsilon_{lmh}(\Gamma^i_m B^\delta_h + \Gamma^\delta_m B^i_h)) + X^s_{tmh}\frac{1}{c}(\Gamma^i_m E^\delta_h + \Gamma^\delta_m E^i_h)) \quad (2.11) \\ & \quad (2.12) \end{aligned}$$

Where density and flux are:

$$n^{i,\delta} = \int f^{i,\delta} d^3v \quad (2.13)$$

$$\Gamma^{i,\delta}_m = \int v_m f^{i,\delta} d^3v \quad (2.14)$$

Here the Einstein summation rule is applied. An expression for the tensor X^s_{tmh} can be found in reference 64. χ^s_{tl} represents plasma susceptibility and expression for it can be found in reference 65. ϵ_{lmh} is the Levi-Cevita symbol. The first term in the Eq. (2.11) represents scattering off electron density and electric field fluctuations. The second term denotes scattering off electron flux and magnetic field fluctuations, the third term describes the physics of scattering off electron flux and electric field fluctuations. It is important to mention that all these terms are taken into account when the experimental results are evaluated, because depending on scattering geometry and plasma parameters the values of different terms in the equation

may change. Measured spectral power density is given by the equation of transfer [66]:

$$\frac{\partial P^s}{\partial \nu^s} = P^i O_b (\lambda_0^i r_e)^2 n_e \frac{\Sigma}{2\pi} \tag{2.15}$$

Here $\frac{\partial P^s}{\partial \nu^s}$ is spectral power density (SPD) of the scattering radiation [J], P^i is power of probing radiation [W], λ_0^i is vacuum wavelength of probing radiation [m], r_e is classical electron radius ($2.82 \cdot 10^{-15}$ m) and Σ is scattering function [s^{-1}], O_b is an overlap integral [m^{-1}]. The overlap integral is defined as

$$O_b = \int_V I^i I^s d^3 r \tag{2.16}$$

where I^i and I^s are normalized intensities of incident and scattering beams, respectively. The scattering function Σ takes into account microscopic fluctuations (e.g. caused by fast ions) and the way they influence scattering of the probing radiation, see Eq. (2.17). It contains nearly all information about the frequency dependence of the scattering signal [66]:

$$\Sigma = \frac{(\omega^i \omega^s)^2 \hat{G}_l^{(\alpha)} < \tilde{\alpha}_l \tilde{\beta}_m > \hat{G}_m^{(\beta)*}}{\omega_p^4 S^i S^s} \tag{2.17}$$

where $\tilde{\alpha}$ and $\tilde{\beta}$ refer to fluctuating quantities such as density, flux, electric and magnetic fields. Summation over repeating indexes is implied. $\hat{G}$ is a coupling operator which describes how the source currents from the incident wave and waves in plasma couple into a propagating mode of the scattering waves (two different modes of electromagnetic waves propagate in plasma in presence of the external magnetic field, ordinary O-mode and extraordinary X-mode. The difference is in the polarisation of the electric field of the wave with respect to the external magnetic field). $S^{i,s}$ are normalized fluxes. Detailed expressions for them can be found in appendix B in reference 65.

In the electrostatic limit, the CTS signal depends on the projection of the fast ion velocity distribution function on a given direction:

$$g(u, R, z) = \int f(\mathbf{v}, R, z) \delta(u - \frac{\mathbf{k}^\delta \cdot \mathbf{v}}{k^\delta}) d\mathbf{v} \ , \tag{2.18}$$

where g is the projection of the velocity distribution function on $\mathbf{k}^\delta$ introduced in Eq. (2.8), u is the velocity along the direction of projection, $f(\mathbf{v})$ is a 3D velocity distribution function and δ is the Dirac delta function. The purpose of the fast ion CTS diagnostic is to infer the $g(u, R, z)$ (later just $g(u)$) from the scattering spectrum. This is done by forward modelling and using Bayesian least-square fitting technique which takes information on all relevant plasma parameters including their uncertainties into account [67].

2.4 How To Interpret Fast Ion CTS Results

It is important to describe the relationship between the 2D fast ion distribution function and the diagnostic measurement. The results discussed here have been published in reference 68.
As we know from Section 2.3, the model which is used to infer the projection of the fast ion velocity distribution function implies that the plasma inside the scattering volume is uniform and isotropic in the direction transversal to the magnetic field. Thus the movement of fast ions with such approximation is truly 2D, i.e. does not depend on the gyroangle. There are several ways how the fast ion velocity distribution function can be represented (see Fig. 2.11). Usually fast ion velocity distribution function is shown in 2D coordinates $(v_{||}, v_{\perp})$ or (E, p), where p is a pitch of fast ion to the magnetic field, E is the kinetic energy of the energetic ion, $v_{||}$ and $v_{\perp}$ denote velocities parallel and perpendicular to the magnetic field, respectively. The 3D coordinate system $(v_{||}, v_{\perp 1}, v_{\perp 2})$ contains no additional information to the coordinate system $(v_{||}, v_{\perp})$ since the movement in the direction transverse to the magnetic field is assumed to be isotropic, leaving no dependence on the gyroangle. In the 3D description this information is present, even though it is not of practical importance. The parameters $v_{\perp 1}$ and $v_{\perp 2}$ denote two orthogonal axes perpendicular to the magnetic field in a 3D Cartesian coordinate system, the third coordinate, $v_{||}$, is directed along magnetic field. The $g(u)$ representation (see Section 2.3) obviously lacks information on the 2D fast ion velocity distribution function. As it is shown in reference 68, a reasonable reconstruction of the 2D distribution function can be found from two or more simultaneous measurements of $g(u)$ at the same location with different resolved angles.

Fig. 2.12 illustrates where particles with particular velocity vectors elicits a response in the $g(u)$ projection. A particle with velocity $(v_{||}^p, v_{\perp}^p)$ with a particular gyroangle γ^p will have the projection on $\mathbf{k}^\delta$ at u according to Eq. (2.19):

$$u^p = v_{||}^p cos(\phi) + v_{\perp}^p sin(\phi) cos(\gamma^p) \tag{2.19}$$

where ϕ is a projection angle of the measurement.

Now we know where to expect the response of fast ion with given velocities and a gyroangle. However, the CTS measurements give us an information on the projection of the fast ion distribution function. Obtaining this information, one would like to know which part of the 2D distribution gives rise to the projection at a particular u. In order to understand that we can employ a method of weight functions proposed by W. W. Heidbrink and developed by M. Salewski [68]. The $g(u)$, as it was written in Section 2.3, is defined as

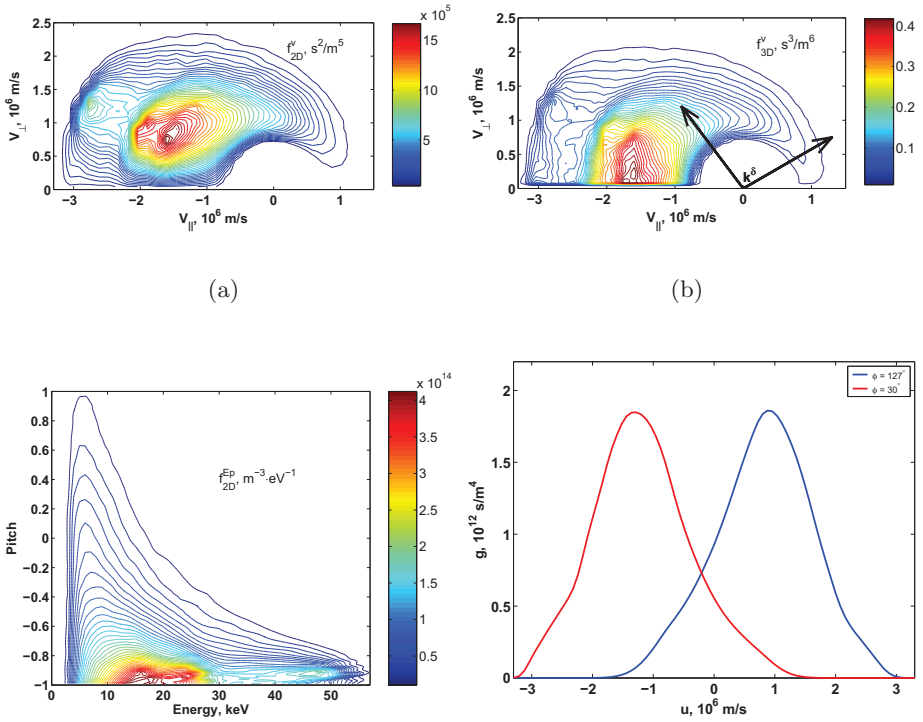

Figure 2.11: Simulated by ASCOT steady-state slowing down velocity distributions of the fast ions for the TEXTOR discharge 111822 at R = 1.8 and z = 0; (a) 2D fast ion velocity distribution function (integrated over the gyroangle); (b) 3D fast ion velocity distribution function (isotropic in the transversal direction), black arrows shows the direction along which the projections are taken; (c) 2D fast ion distribution function in energy - pitch description; (d) The projections of the fast ion velocity distribution function on the $\mathbf{k}^{\delta}$ directions indicated in Fig. 2.11(b).

$$g(u) = \int_{-\infty}^{\infty}\int_{-\infty}^{\infty}\int_{-\infty}^{\infty} f_{3D}^{v}\delta(u - \frac{\mathbf{k}^{\delta}\cdot\mathbf{v}}{k^{\delta}})dv_{||}dv_{\perp 1}dv_{\perp 2}$$

It can alternatively be expressed in cylindrical coordinates $(v_{||}, v_{\perp}, \gamma)$, where γ is a gyroangle:

$$g(u) = \int_{-\infty}^{\infty}\int_{0}^{\infty} f_{2D}^{v}dv_{||}dv_{\perp}\int_{0}^{2\pi}\delta(u - v_{||}cos(\phi) + v_{\perp}sin(\phi)cos(\gamma))d\gamma$$

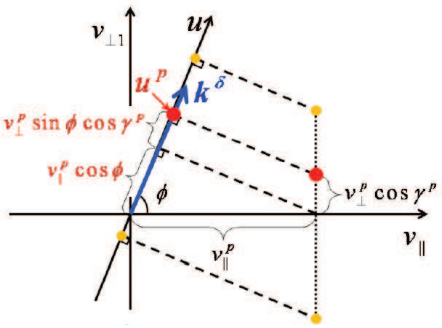

Figure 2.12: $(v_{||}, v_{\perp 1})$ plane. Large red dot represents a particle in the velocity space at a particular of phase of the gyration. The coordinate of this particle in the $(v_{||}, v_{\perp 1})$ velocity plane is $(v_{||}^p, v_\perp^p \cdot cos(\gamma^p))$ and it is depicted as a bold red dot. This particle at different phases of the gyromotion might be located in the velocity space in the following limits: $[(v_{||}^p, v_\perp^p), (v_{||}^p, -v_\perp^p)]$. The limits are depicted as yellow dots. The projection of this interval (dashed lines are perpendiculars to the $\mathbf{k}^\delta$) on $\mathbf{k}^\delta$ indicate an interval on u direction where the particle will elicit a response: $[v_{||}^p cos(\phi) - v_\perp^p sin(\phi), v_{||}^p cos(\phi) + v_\perp^p sin(\phi)]$, where ϕ is an angle between $\mathbf{k}^\delta$ and $v_{||}$ axis. The figure is taken from reference 68

At the same time weight function is defined like in Eq. (2.20):

$$g(u,\phi) = \int_{-\infty}^{\infty}\int_{0}^{\infty} w(u,\phi,v_{||},v_\perp) f_{2D}^v dv_{||} dv_\perp \tag{2.20}$$

From this one can conclude that the weight function is

$$w(u,\phi,v_{||},v_\perp) = \int_0^{2\pi} \delta(u - v_{||}cos(\phi) + v_\perp sin(\phi)cos(\gamma)) d\gamma \tag{2.21}$$

Using the properties of the Dirac's δ - function and performing the integration, we find that the weight function is

$$w(u,\phi,v_{||},v_\perp) = \frac{1}{\pi\sqrt{v_\perp^2 sin^2(\phi) - (u - v_{||}cos(\phi))^2}} \tag{2.22}$$

An example of the inner product of the weight function for the same u and different projection angles are shown in Fig. 6.9.
It should be noticed here that the weight functions for FIDA can be derived in the same way. The weight functions approach is very important for future multi-diagnostic studies of fast ions because it allows using experimental results from both CTS and FIDA for the reconstruction of the 2D velocity distribution function.

Chapter 3

Experimental Setup

The Risø DTU CTS group utilizes the CTS diagnostics at ASDEX Upgrade and TEXTOR. This chapter is devoted to the description of the experimental setup used for the experiments. The tokamaks and auxiliary heating systems are briefly discussed.

3.1 ASDEX Upgrade

ASDEX Upgrade is a mid-size tokamak located in Garching, Germany. The main parameters of the ASDEX Upgrade tokamak are listed in Table 3.1. The tokamak has a very large power density of auxiliary heating. It is equipped with 8 NBIs, ECRH, and ICRH systems. The NBIs provide different injection geometries where it can make both on- and off-axis injection. Injection species and target plasma are usually deuterium. The NBI sources are grouped into two NBI boxes with different injection energies, 60 keV (NBI box 1, NBI sources 1-4) and 93 keV (NBI box 2, NBI sources 5-8). A sketch of the ASDEX Upgrade NBI geometry is shown in Fig. 3.1.

ASDEX Upgrade is well-equipped for fast ion studies. The sources of fast

Plasma limitation	Single X-point configuration
Major radius	1.65 m
Minor horizontal radius, a	0.5 m
Minor vertical radius, b	0.8 m
B_t	up to 3.1 T
I_p	400 - 1600 kA
Plasma volume	14 m^3
Pulse duration	up to 10 s
Total installed aux. heating power	up to 26 MW
Heating methods	NBI, ICRH, ECRH

Table 3.1: Main parameters of the ASDEX Upgrade tokamak.

ions are NBI (60 - 93 keV) and ICRH (up to MeV energies). A large set of fast ion diagnostics is installed in the tokamak: CTS, FILD, FIDA, NPA, neutron and γ-ray spectroscopy. A systematic multi-diagnostic approach towards fast ion physics studies on ASDEX Upgrade is planned for the future.

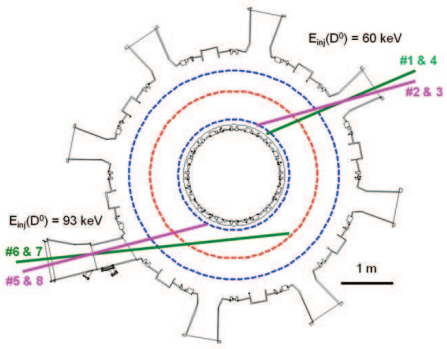

Figure 3.1: Schematic of the ASDEX Upgrade NBI system. NBI box 1 operates four 60 keV deuterium injectors with different launching geometry (NBI1 - NBI4), NBI box 2 operates four 93 keV deuterium injectors with different launching geometry (NBI5 - NBI8)

3.2 CTS on ASDEX Upgrade

Currently, the CTS diagnostics on ASDEX Upgrade consists of one receiver and a source of probing radiation. The new ECRH system at ASDEX Upgrade is intended for four dual-frequency gyrotrons 140/105 GHz (currently three of them are installed). The CTS diagnostic uses a gyrotron at 105 GHz frequency as a probing source because at standard ASDEX Upgrade operating scenario (B_t = 2.5 T) the probing frequency does not coincide with any harmonic of electron cyclotron resonance in the plasma, thus the probing beam is not absorbed during the experiments. Four transmission lines, one for each gyrotron, are used to transmit radiation from the sources to the plasma, see Fig. 3.2. The CTS diagnostic shares transmission line with the ECRH system. Currently, the CTS receiver at ASCDEX Upgrade shares the transmission line with gyrotron no 2 and uses gyrotron no 1 (see Fig. 3.2) as source of probing radiation.

The gyrotron radiation, after leaving the transmission line, is launched in O-mode into the plasma using steerable mirrors. The O-mode of scattering radiation is coupled to the waveguide also by means of a steerable mirror. Use of steerable mirrors for the receiver and the probe (see Fig. 3.2) provides the CTS diagnostic with flexibility in choosing different scattering geometries. Mirror 1 in Fig. 3.2 is used for launching the probe beam into the plasma and mirror 2 collects the scattering signal. Fig. 3.3 illustrates the nomenclature of the antenna angles that will be described in this thesis.
Radiation from the plasma is coupled to the HE11 mode and propagates through a 70 m long waveguide which ends at a matching optics unit (MOU box, see Fig. 3.4) in the free-space propagation regime. The MOU box is designed and primarily used for ECRH. It contains necessary quasioptical components for launching high power microwaves into the plasma, namely phase-correcting mirrors, broadband polarisers, and an HE11 coupling mirror. Shown in Fig. 3.4, two additional mirrors are installed for the CTS operating mode of the ECRH transmission line. One of the mirrors is mounted on the frame of the MOU box on the side closer to the reader. Another mirror is installed on a movable arm (see Fig. 3.4). When the movable arm is in the outward position (Fig. 3.4(a)), the gyrotron radiation propagates freely onto the phase correcting mirror, polarizers and finally into the waveguide. The MOU box operates in the CTS regime when the movable mirror is placed at the inward position shown on the Fig. 3.4(b). In this mode, the received radiation propagating from the plasma through the waveguide is intercepted between the polarizer and the the second phase correcting mirror. The movable mirror reflects the radiation onto the fixed mirror which couples it into the receiver horn.

A schematic of the CTS receiver [69] is depicted on Fig. 3.5.
The CTS receiver is of a heterodyne type and is designed to acquire signal

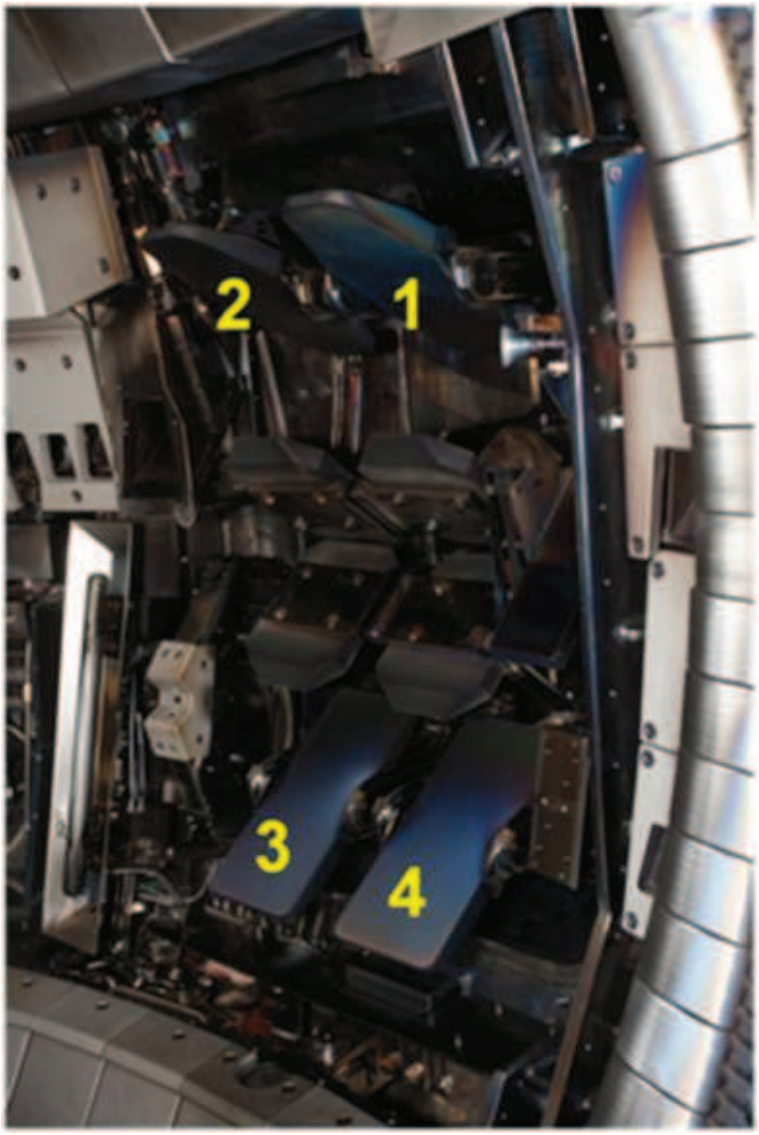

Figure 3.2: Photo of the ECRH launchers on ASDEX Upgrade. Mirror no. 1 is used to launch probing radiation into the plasma, mirror no. 2 is used to direct scattered radiation from the overlap volume into the waveguide.

in the range of 100-110 GHz. The main challenge which the CTS receiver on ASDEX Upgrade faces is similar to the one on TEXTOR (see Section 3.3) - it has to have a very large dynamic range to resolve a signal in the order of a few eV with the background level of 30 - 200 eV depending on plasma parameters and experimental geometry.

When the radiation enters the receiver, it propagates through the radio frequency (RF) line in the receiver (shown in red in Fig. 3.5). The radiation

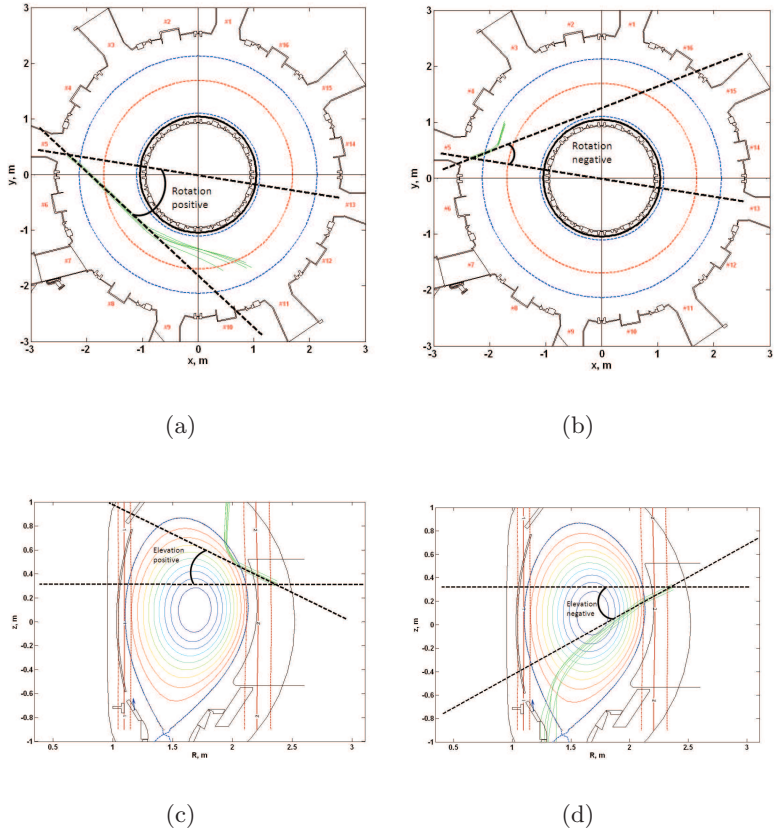

(a) (b)

(c) (d)

Figure 3.3: Illustration of the geometrical angles which are used to describe mirror position. Top view of ASDEX Upgrade is shown in (a) and (b), poloidal view is shown in (c) and (d). The figure shows the sign convention used for the elevation and rotaitons angles which are angles with respect to the mirror normal and the axis displayed in the figures (a) - (d).

contains scattering signal, ECE background and stray radiation from the gyrotron. In order to protect the receiver from intense stray radiation from the gyrotron, which can be many orders of magnitude larger than the ECE background and the scattering signal, a series of two notch filters is installed in the RF line of the receiver right after the horn. The stopband of the filters is centred around 104.95 GHz and each has a bandwidth of 130 MHz. The notch filters were characterized separately because the dynamic range of the network analyser was not sufficient for such measurements. However, because the impedances of filters are matched, the combined transmittance of two notch filters can be obtained by multiplication of their individual transmittances (or summation in logarithmic scale). Thus, the combined

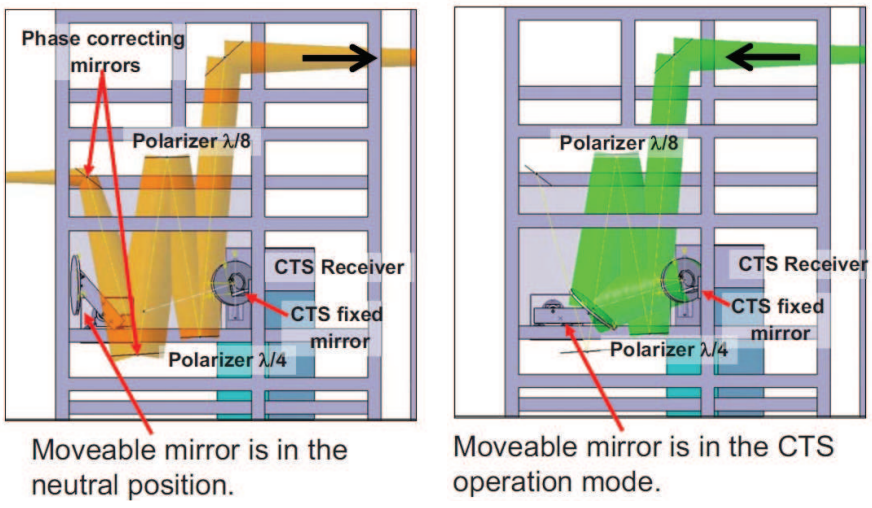

(a) (b)

Figure 3.4: The MOU box in the normal (ECRH) operating mode (a) and in the CTS operating mode(b). The steerable mirror diverts the radiation propagating into the MOU box into the CTS receiver. Figure is taken from reference 26.

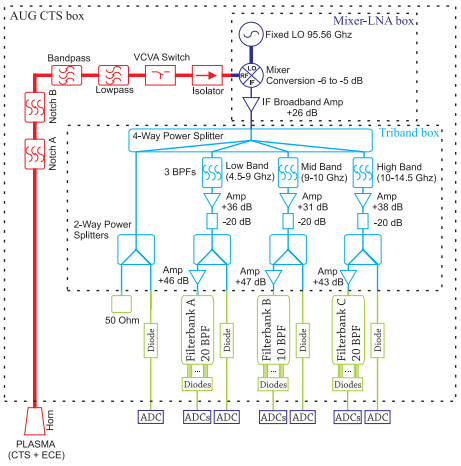

Figure 3.5: Schematic of the CTS receiver installed on ASDEX Upgrade. Different colours depict different functional parts of the receiver. Figure is taken from reference 69.

depth of the stopband exceeds 100 dB and reliably protects the components of the CTS receiver further down the transmission line (as long as the gyrotron frequency stays inside the notch). The characteristics of the notch filters are shown in Fig. 3.6.

In a heterodyne radiometer, a mixing stage with an external local oscillator

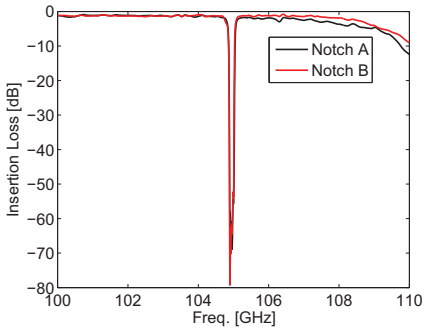

Figure 3.6: Insertion losses of two notch filters measured separately in the frequency range 100 - 110 GHz. Figure is taken from reference 69.

(LO, a source of radiation for the mixer) is used. In the ASDEX Upgrade CTS receiver, the signal is mixed with a frequency in the range of 95 GHz. In order prevent any signal with frequencies from outside the range of 100 - 110 GHz, a bandpass filter is installed after the notch filters. Unfortunately, because of peculiarities in the designs of cavities of the bandpass filter, it has relatively high transmittance for frequencies in the range of 140 GHz. Gyrotrons at ASDEX Upgrade work routinely at this frequency dur-

ing standard ASDEX Upgrade operations. Thus a very strong signal can be expected at this frequency. In order to minimize risks for the receiver, an additional low-pass filter with the limiting frequency of approximately 140 GHz is installed.
During switching-on time, the gyrotron frequency chirps down typically by approximately 100 - 200 MHz. The results of the stray radiation measurements are presented in Fig. 3.7 [26], and the methodology of the measurements is described in reference 70. The space between the two black dashed horizontal lines denotes the frequency range which is protected by the notch filter. As will be descibed in Section 4.5, the CTS measurements require modulation of the probing beam. One can see in Fig. 3.7 that the first 500 μs and the last 200 μs of the gyrotron-on phase where the power is ramped, the CTS receiver is not protected by the notch filters. Thus, for safety reasons, a voltage control variable attenuator (VCVA) is present. When activated, it applies 40 dB attenuation to the full frequency band, i.e. typically every 2 ms because the gyrotron power is modulated for background subtraction, for details see Section 4.5.
The final element in the RF line is an isolator which is used to avoid stand-

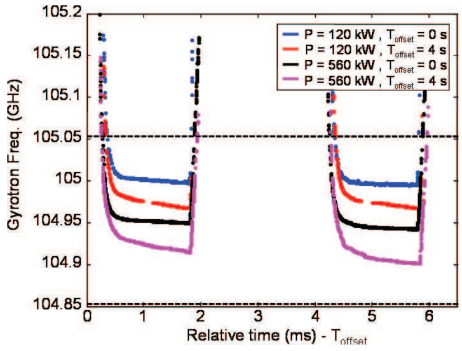

Figure 3.7: Measurements of the frequency chirp of the Odyssey-2 gyrotron firing into the load at different power levels (120 kW and 560 kW) at different times of operations: right after the switching on ($T_{offset} = 0$) and four seconds later ($T_{offset} = 4$). Two horizontal black dashed lines depict boundaries of notch filters. The figure is taken from reference 26.

ing waves due to reflections between the RF components.
In the ASDEX Upgrade CTS receiver, a mixer with an IMPATT diode technology is employed. This mixer is fed by the LO working at a frequency of $f_{LO} = 95.56$ GHz. It converts the RF signal in the range of 100 - 110 GHz into the signal in the intermediate frequency (IF) range of 4.5 - 14.5 GHz. The conversion loss in the mixer is frequency-dependent and varies from 5 to 6 dB, as shown in Fig. 3.8. In general, the scattering signal from the plasma is weak, additionally insertion losses of each element of the receiver is around 1-2 dB, and therefore amplifiers are needed. After the mixer a

broadband amplifier with gain of 26 dB is installed.

The down-converted signal is fed to a 4-way power splitter. The fourth

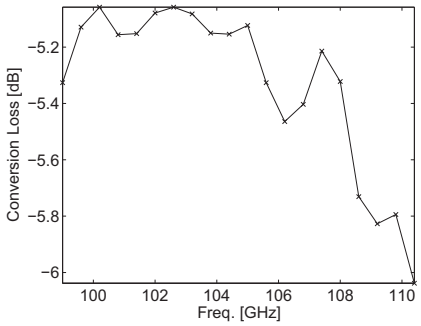

Figure 3.8: Conversion losses of the mixer measured as a ratio between input RF power and output IF power. Figure is taken from reference 69.

output is used solely for monitoring purposes. Signal from each of three remaining bands is transmitted to the band-pass filters. The central bank has a bandwidth of 1 GHz and is centred around the down-converted frequency of the probing radiation. Two other bands cover the up- and the down-shifted parts of the spectrum. The splitter is needed for several reasons. Firstly, very large spectral power density (SPD) is measured in the proximity of the probing frequency and the SPD far away from the probing frequency is low. In order to get a maximum dynamic range, signal with frequency farther away from the gyrotron frequency should be amplified more then signal with frequency closer to the gyrotron frequency. Another reason is to protect the receiver. If for any reason the receiver is exposed to stray radiation from a gyrotron and it is not blocked by either the notch filters or by the VCVA, only one band out of three would be affected. An amplifier in conjunction with an attenuator are present after each output of the triband box. This is due to the fact that the amplification coefficients of the amplifiers are fixed and the total gain can be varied by attenuators installed after the amplifiers in series. Putting attenuators before amplifiers typically reduces signal-to-noise ratio significantly. As it is shown in Fig. 3.5, after the attenuators signal is conveyed to 3 dB couplers, so half of the power enters into a broadband monitoring channels and another half is being amplified once again and than being transferred into the filter bank. The total gain of the triband box (a part of the receiver from the 4-way power splitter until the 3 dB couplers, shown in blue in Fig. 3.5) is depicted in Fig. 3.9. Signal from the triband box outputs is fed to square-law diodes, whose characteristics were measured and is presented in Fig. 3.10, through band-pass filters with the bandwidth from 100 MHz (in the central part of the spectrum) up to 1 GHz (filters for the outermost frequencies compared with the probing frequency). It is very important for calibration that diodes respond to

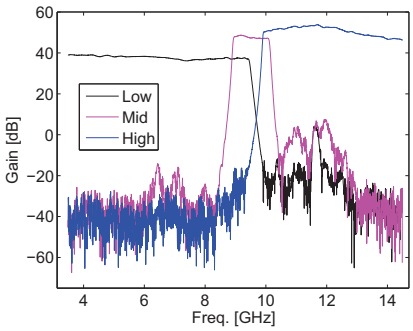

Figure 3.9: Total gain of the triband box (blue in Fig. 3.5). Figure is taken from reference [69].

incident power linearly, therefore sensitivity $-dU_{out}/dP_{in}$ for each diode is calculated, see Fig. 3.10(b). Obviously, when the input power exceeds -23 dBm (0 dBm = 1 mW), the sensitivity drops and the diode response to the input power is not linear any more. The voltage measured on the diodes has negative polarity and is directly proportional to the incident power at intermediate frequencies. The signal from the diodes is acquired by 24 bit 10^5 samples per second ADC cards from National Instruments. However, 24 bits of dynamic range measure signal from +10 V to -10 V, meaning 20 V in total, at the same time diodes, succeeded by the video amplifiers, produce voltage in the range of 0 to -10 V. Thus effective bit depth of our acquisition is 23 bits, which is sufficient.

The CTS diagnostic at ASDEX Upgrade currently undergoes a major upgrade. The receiver is being relocated into the NBI control room where access to all four transmission lines is possible. Installing RF switches allows to assign any transmission line for transmitting either probe or receiver signal. Secondly, a new receiver is about to be installed there. Two receivers make simultaneous measurements at different radii possible. The upgraded diagnostic will be commissioned during the 2012 experimental campaign.

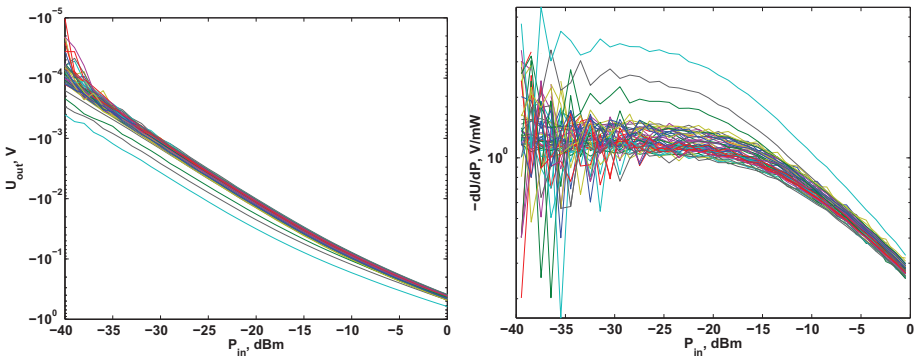

(a) (b)

Figure 3.10: Characteristics of the square-law diodes which are used in the receiver detection scheme. (a) Shows the diode characteristics. Channels with higher sensitivity in high-frequency band are no 42, 44, 46; (b) shows diodes sensitivity to the input power (in V/mW), diodes are driven in non-linear regime if the input power exceeds -23 dBm

.

3.3 TEXTOR

TEXTOR is an acronym for **T**okamak **EX**periment for **T**echnically **O**riented **R**esearch. TEXTOR is a medium-size tokamak in Forschungszentrum Jülich, Germany. It has similar major radius to ASDEX Upgrade but much smaller plasma volume. This is due to the circular plasma cross-section of the TEXTOR tokamak. The basic parameters of the TEXTOR machine are listed in Table 3.2. The tokamak is equipped with two NBIs which are used in CTS experiments as sources of fast ions. The top view of TEXTOR with the injectors is shown in Fig. 3.11. The NBIs can accelerate hydrogen or deuterium up to 50 keV per particle and operate at the power level of up to 1.3 MW each. These injectors have very parallel injection geometry with the same tangency radius R $\approx$ 1.65 m, see Fig. 3.11. One of NBIs injects in co-I_P direction another in counter-I_P (*co-* and *ctr-NBI*, respectively). In the CTS experiments NBI primarily works with hydrogen in order to avoid an enhanced radiation level due to D - D reactions between the beam ions and the background plasma. Another reason is that having the same energy, hydrogen atoms move with $\sqrt{2}$ larger speed than deuterium, therefore they cause a larger frequency shift in the spectrum of the scattering signal. Calculations of the ionization profile provided by the ASCOT and VENUS codes show, that during typical CTS scenario discharges the deposition profile of the NBI-originated fast ions peaks in the plasma centre.

Plasma limitation	Limiter / **D**ynamic **E**rgodic **D**ivertor
Major radius	1.75 m
Minor radius	0.47 m
B_t	up to 3 T
I_p	up to 800 kA
Plasma cross section	Circular
Plasma volume	7 m^3
Pulse duration	up to 10 s
Total installed aux. heating power	up to 9 MW*
Heating methods	NBI, ICRH, ECRH**

Table 3.2: Main parameters of the TEXTOR tokamak. * - include ECRH; ** - ECRH is currently decommissioned. The data are taken from www2.fz-juelich.de

TEXTOR is equipped with two gyrotrons working at frequency of 140 GHz and 110 GHz, respectively. The CTS diagnostic utilizes the 110 GHz gyrotron as a source of probing radiation at $B_t = 2.6$ T. At this scenario the gyrotron frequency does not coincide with any harmonic of the electron cyclotron resonance in the plasma. Thus the probing beam is not absorbed and the electron cyclotron emission is minimized.

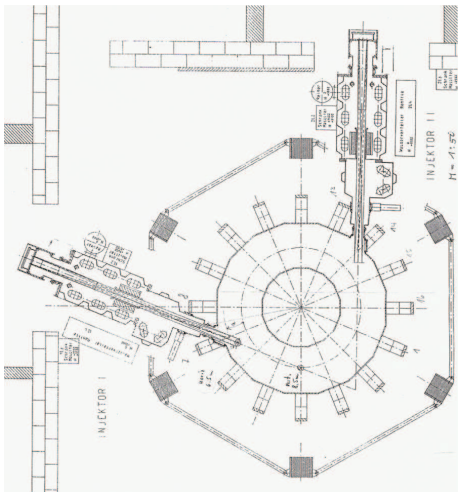

Figure 3.11: Schematic of the installation of TEXTOR NBI. Top view. The figure is a courtesy of R. Uhlemann.

3.4 CTS on TEXTOR

The CTS diagnostic on the TEXTOR tokamak is very similar to the one on ASDEX Upgrade and historically was built earlier. Here mainly the differences between the two are described.
The 110 GHz gyrotron is primarily used for the CTS experiments. The front-end part of TEXTOR CTS, like at ASDEX Upgrade, is equipped with steerable mirrors, see Fig. 3.13, but unlike the current ASDEX Upgrade CTS (Fig. 3.5), the probing and receiving mirrors are located on top of each other. This difference has implications on alignment check for both ASDEX and TEXTOR CTS systems. This will be discussed in Section 4.3. It is also important to mention that the CTS system on TEXTOR can make toroidal sweeps during discharges, in contrast to the one on ASDEX Upgrade.
Unlike the ASDEX Upgrade CTS diagnostic, the CTS system at TEXTOR does not utilize an ECRH transmission line for conveying scattering signal to the receiver. After leaving the plasma, received radiation is transferred to the receiver in free-space propagation mode, see Fig. 3.12.

Different probing frequency requires higher local oscillator frequency in

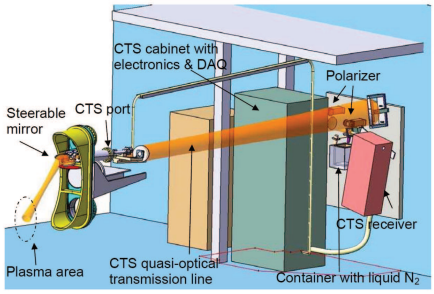

Figure 3.12: Schematic of the CTS quasioptical transmission line for the CTS receiver. Figure is taken from reference 71.

the mixing unit (100.6 GHz) in order to mix the signal to the convenient intermediate frequency (IF) band.
In the IF part of the CTS receiver, the system at TEXTOR uses a triplexer. The triplexer splits the signal in the frequency range of 0.5 - 40 GHz into three frequency bands. One of the outputs (bandwidth 18 - 40 GHz) is terminated, another output (bandwidth 8 - 18 GHz) is fed to a diplexer which divides the signal into two bands with frequencies 8 - 10.68 GHz and 10.68 GHz - 18 GHz. The signal after the triplexer and the diplexer and further amplification is conveyed further to the filters and the detection diodes.
The receiver has 42 channels. 32 of them have a bandwidth of 80 MHz each and are probing the central part of the spectrum, where the spectral power is the highest. The rest of the channels have bandwidths from 140 MHz to 750 MHz depending on how far the frequency which they are probing is

from the probing frequency. The ADCs are similar to those installed in the ASDEX Upgrade CTS receiver.

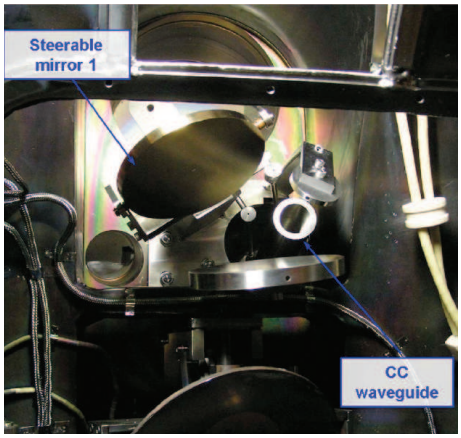

Figure 3.13: Steerable in-vessel receiver mirror on TEXTOR CTS. Figure is taken from reference 72.

3.5 Receiver Upgrade for High Frequency Resolution Measurements

For performing fuel ion ratio measurements [73–75] (see Section 5.4) and measurements related to NBI-induced instabilities [76] described in Chapter 8, frequency resolution requirements for a receiver are much higher than existing set-ups could provide. In these experiments, harmonics of ion cyclotron frequency in the plasma have to be resolved. For investigations of the ion cyclotron structure in the scattering spectrum, the frequency resolution should be in the order of a few MHz. In order to fulfil such high demands, a Tektronix Digital Phosphor Oscilloscope (model DPO 7104) was connected to the receiver, see Fig. 3.14. An upgraded part of the receiver is shown in light blue. The oscilloscope can acquire data with up to $5{\cdot}10^9$ samples per second and 8 bit per sample. It is equipped with 256 MB of fast memory which allows acquisition of nearly 50 ms of data. The fast oscilloscope is connected to the center band of the triplexer through an additional amplifier and a power splitter. The split signal is transmitted to the second mixing stage via the band-pass filter with bandwidth of 1 GHz. The band-pass filter is essential because it helps to avoid aliasing. After the band-pass filter the signal in the frequency range from 9 GHz to 10 GHz is mixed down to frequencies of 0.2 GHz to 1.2 GHz and, after additional amplification, is ready for detection. Recently the ASDEX Upgrade CTS receiver was upgraded with a fast acquisition system for the same purposes

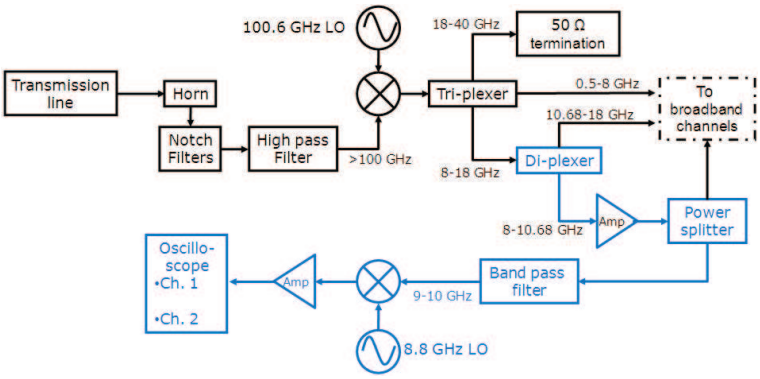

Figure 3.14: A schematic of the upgraded CTS receiver on TEXTOR. Light blue shows a new, upgraded part of the receiver. The oscilloscope is Tektronix DPO 7104.

but due to its similarity it will not be discussed here.

Chapter 4

Methodology of the Experiments

In this chapter preparatory steps for the CTS experiments on ASDEX Upgrade and TEXTOR, and methodology of the experiments are described. CTS diagnostics work at frequencies in the range of electron cyclotron frequency in fusion plasmas. Typical values of the SPD from scattering due to fast ion motion is in the order of a few electron-volts. However, the electron temperature in the plasma is somewhere from several tens of eV to several keV. It is important to note that even though the plasma is not optically thick at the locations where the background originates from, the values of the SPD from the electron cyclotron emission are in the order of the local electron temperature and thus much higher than the SPD of the scattering signal. That reduces the signal-to-noise ratio drastically. In order to avoid low signal-to-noise ratios, the magnetic field should be chosen in a way so that all frequencies which the CTS receiver can detect should not coincide with any harmonic of electron-cyclotron emission (ECE) from the plasma. This is briefly illustrated in Fig. 4.1. The probing and receiver beams are not allowed to be absorbed, either. In the case of ASDEX Upgrade and TEXTOR, CTS experiments are performed at on-axis magnetic field values $B_t = 2.5 - 2.6$ T. At such values of the magnetic field, the plasma is located in between the fundamental and the second harmonics of electron-cyclotron resonances for all the frequencies which the CTS receivers are sensitive to. Just as a remark, the CTS in ITER will work at 60 GHz. Such a low frequency is used partly because of the large cross-sections of plasmas in ITER which makes it impossible to find a frequency when it located in between the harmonics of resonances.

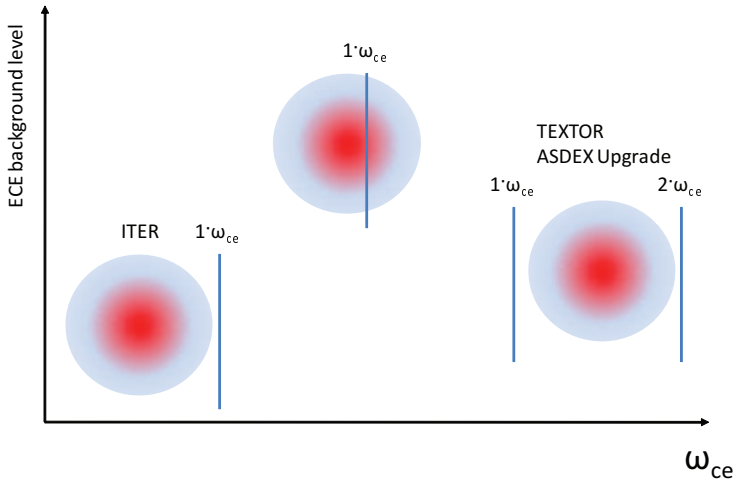

Figure 4.1: A sketch illustrating a dependence of ECE background detected by the CTS receiver from position of EC resonances in the plasma.

4.1 Alignment of the Transmission Line

Alignment is of crucial importance for the CTS diagnostic. This is because the beam travels a fairly long distance between the launcher/receiver and the plasma. Alignment of the transmission line for the probing radiation is typically a responsibility of the ECRH groups, because the same gyrotron and transmission line is used for plasma heating. Alignment of the receiving part of the diagnostic is made by the CTS group. The procedure for the ASDEX Upgrade CTS system is described in details in reference 26, the results are briefly summarized in this section. Travelling in the overmoded waveguide with a large amount of mitre-bends, even a small misalignment at a certain location in the waveguide can cause significant astigmatism and creation of side-lobes. Correct alignment is of crucial importance for the right localization of measurements. An example of poor alignment of the transmission line is shown in Fig. 4.2. This section is devoted to alignment of the CTS diagnostic in ASDEX Upgrade. For proper microwave alignment a device named micro-rig is used. This is a two-dimensional scanning rig with a sniffer probe coupled with a 110 GHz detection diode, developed and constructed at Risø DTU. A Gunn diode or a backward wave oscillator working at 110 GHz is used as a source of radiation. The power of the source should be low enough so that the detection diode works in the linear regime. In order to align the transmission line, a piece-wise method is used. For this, the source of radiation is placed into the transmission line using an HE11 coupler which transforms the Gaussian beam into the HE11 mode. The piece-wise alignment is carried out between two components from the HE11 section towards the receiver. A specially constructed two-way laser

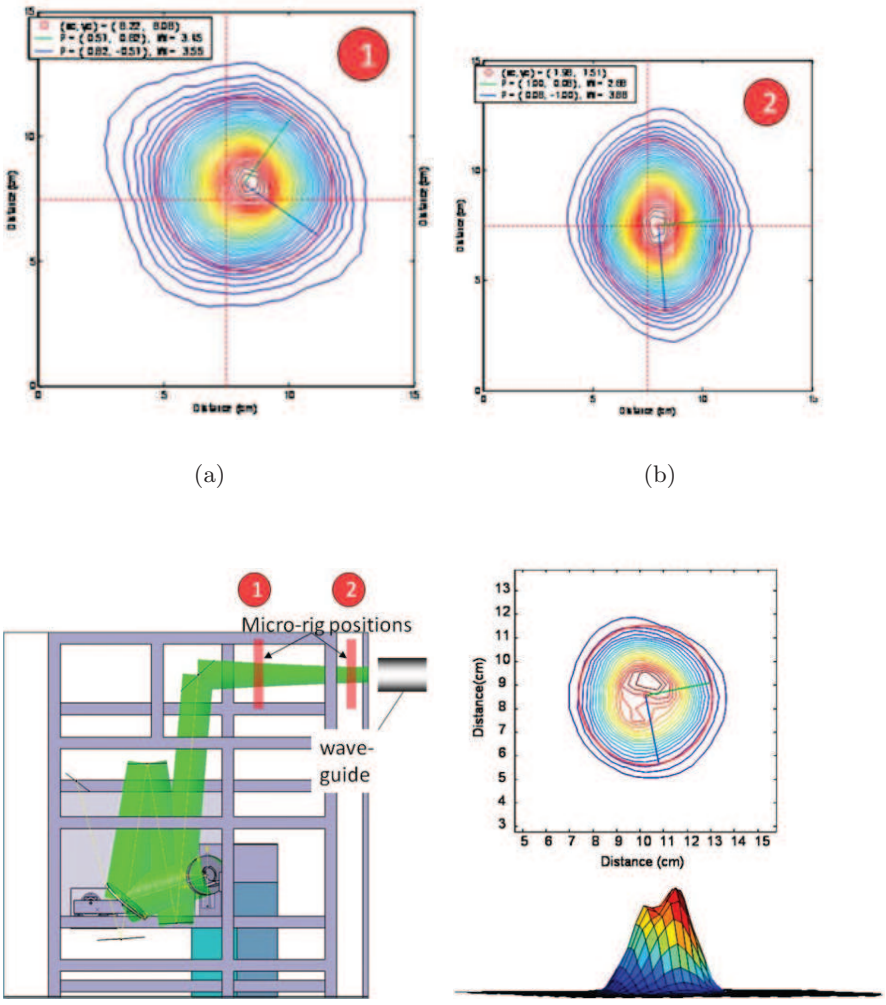

(a) (b)

(c) (d)

Figure 4.2: Examples of good and bad alignment in the MOU box measured with the micro-rig are shown in (a) (ellipticity 0.97) and (b) (ellipticity 0.75). The intersection of the two red dashed lines corresponds to the center of the beam in case of ideal alignment. (c) shows where the measurements presented in (a) and (b) were made. (d) shows the case of a side lobe in the beam measured at the end of the waveguide next to the tokamak when laser alignment was perfect. Figure is taken from reference 26.

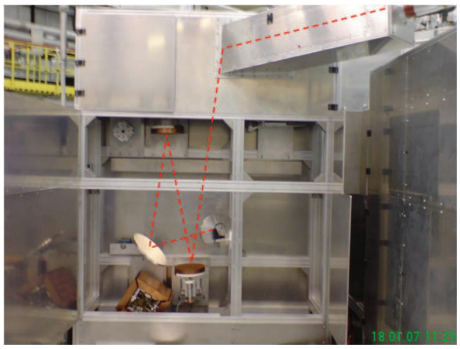

Figure 4.3: Schematic of laser alignment in the MOU box. Red dashed lines denotes a laser beam.

is used to connect geometrical centres of the components. The laser is also used to reference the micro-rig measurements. The micro-rig scan is conducted after laser alignment. The astigmatism and misalignment detected during the measurements are corrected by adjusting mirror angles. The final stage of ex-vessel alignment is carried out by attaching the source to the receiver horn and carrying out a piece-wise alignment inside the MOU box (see Fig. 4.3). The position of the receiver horn and the position of the coupling mirror were found to influence ex-vessel alignment the most. In-vessel measurements are made in order to check that neither probing nor receiver beam would have any side lobes at any settings of the antenna mirrors. Micro-rig scans confirmed this for different angles of the antennas, also at extreme values. The ASDEX Upgrade ECRH group performed laser calibration, so they mapped the settings of the antennas to elevation and rotation angles. Another purpose of the in-vessel measurements is to find discrepancies between laser and microwave alignment. For this the micro-rig scans at fixed antenna values were performed. For acquiring positions of the centre of the beam measured by the micro-rig, the FARO arm, supplied and operated by the ASDEX Upgrade staff, is used. This instrument has many degrees of freedom; once positioned at the known location it tracks the location of its tip in Cartesian coordinates. Performing measurements at different distances from the antenna and obtaining the 3D positions of the beam centres, a vector representing wave propagation can be calculated and compared with the results of the laser calibration. Spacing between the propagation direction vector of the microwaves and the laser beam as a function of distance from the antenna is shown in Fig. 4.4 for various antenna settings. It shows that for typical CTS experiments the deviation is less than 2 cm, or 1°. A similar method was used on TEXTOR, but the functions of the micro-rig and the FARO arm were delegated to a single robot device which makes microwave measurements and obtaining a coordinate in 3D of each measurement point.

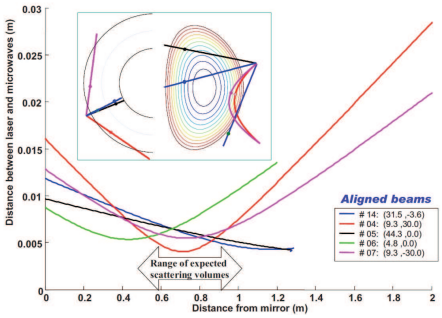

Figure 4.4: Spacing between the wave propagation vector of the microwaves and the laser beam as a function of distance from the steerable mirror. Poloidal and top views of used antenna settings are depicted in the top left corner. The figure is taken from reference 26.

4.2 Ray-tracing and Beam-tracing

The CTS diagnostics installed on TEXTOR and ASDEX Upgrade are capable of performing measurements at different spatial locations with various projection angles with respect to the mangetic field. Such a flexibility is achieved by using movable mirrors for the front-end parts of the ECRH launching system and the CTS receiver. However, flexibility requires very careful alignment (see Section 4.1). Moreover, even in the case of a well-aligned system in non-transversal launching and receiving geometries, refraction has a significant impact on beam trajectories in plasmas. In order to deal with these challenges and find the mirror positions for which probing and receiving beams intersect, an overlap sweep is used.

4.2.1 Overlap Sweep

The essence of this method is sweeping one of the beams (receiver or probing) across another in order to find the mirror settings at which the maximum overlap is achieved. Typically the gyrotron launching mirror is kept still while the receiver mirror is swept. A sketch of the process is depicted in Fig. 4.5. The time trace of the received signal in one of the bulk channels (no. 27) in the TEXTOR receiver during the overlap sweep is shown in Fig. 4.5(c). The background (blue in the figure) does not change significantly during the sweep because the majority of the background radiation is located at the edge of the plasma. The signal during gyrotron-on periods shown in red (which consists of both ECE background and scattering) has a bell-like shape. Sudden drops in level between signal level at two neighbour gyrotron-on periods is due to sawtooth oscillations which change plasma temperature and density inside the sawtooth inversion radius (where the overlap volume is located). When the mirror position at the moment of maximum overlap is

identified, the location of the measurement volume can be determined using ray-tracing (see next subsection). An example of two scattering geometries for ASDEX Upgrade is shown in Fig. 4.6.

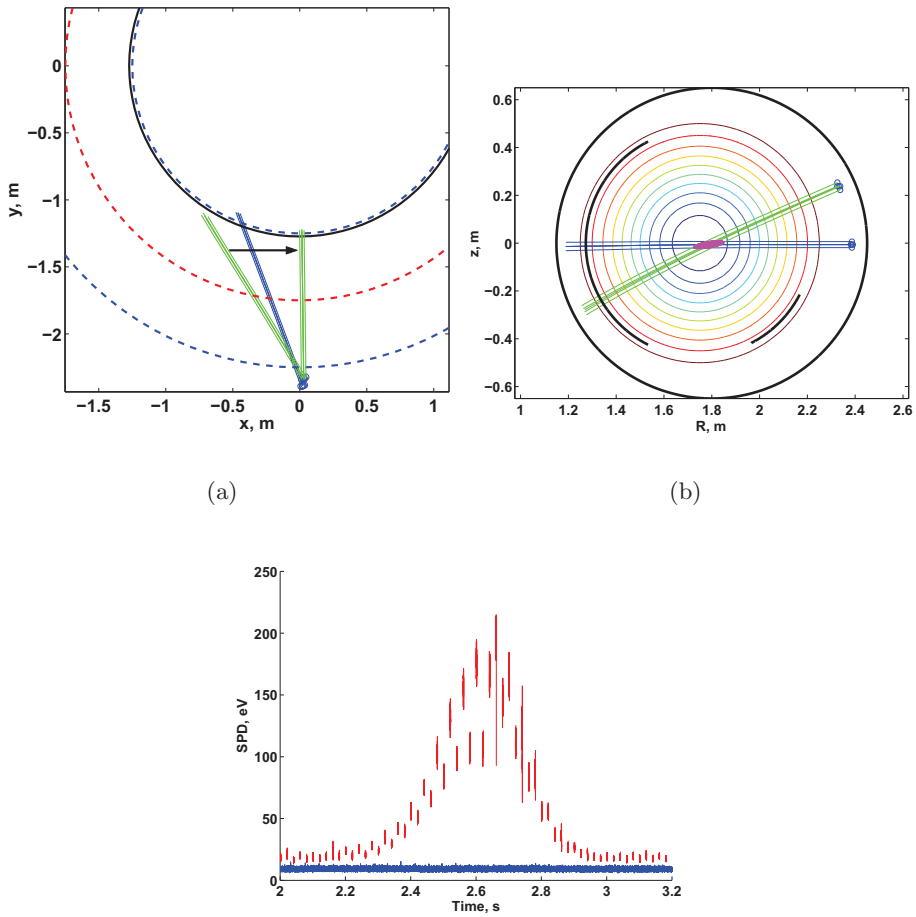

(a) (b)

(c)

Figure 4.5: Schematic illustration of the overlap sweep. Solid blue lines denote probing beam and solid green lines denote receiver beam. (a) Top view of the TEXTOR tokamak. Two sets of solid green lines denote initial and final position of the receiver beam, the black arrow denotes the direction of the scan; (b) Poloidal cross-section of the TEXTOR tokamak, the probing and receiver are at the position of maximum overlap, the pink ellipsoid estimates the size of the scattering volume; (c) An example of the received signal in channel 27 of the TEXTOR CTS receiver during the overlap sweep, discharge 111506. Red and blue lines correspond to gyrotron-on and -off periods, respectively.

4.2.2 Ray-tracing

Equations for ray-tracing are well-known and described in reference 77:

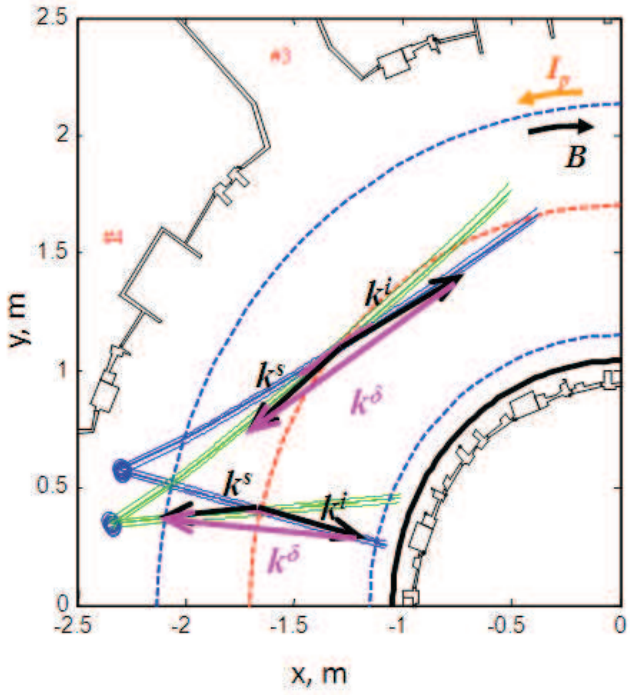

Figure 4.6: Scattering geometries in ASDEX Upgrade simulated with a relativistic ray-tracing code. Green and blue lines represent the receiver and probe beams, respectively. Arrows denote wave vectors. The direction of plasma current and magnetic field are marked.

$$\frac{\partial \mathbf{r}}{\partial t} = \frac{\partial \omega}{\partial \mathbf{k}} \tag{4.1}$$

$$\frac{\partial \mathbf{k}}{\partial t} = -\frac{\partial \omega}{\partial \mathbf{r}} \tag{4.2}$$

However, these equations are not easy to handle numerically. Instead, they were re-written in terms of weakly relativistic dispersion function, Λ, described in reference 63:

$$\frac{\partial \mathbf{r}}{\partial t} = -\frac{\partial \Lambda / \partial \mathbf{k}}{\partial \Lambda / \partial \omega} \tag{4.3}$$

$$\frac{\partial \mathbf{k}}{\partial t} = \frac{\partial \Lambda / \partial \mathbf{r}}{\partial \Lambda / \partial \omega} \tag{4.4}$$

Ray-tracing technique requires that anti-Hermitian part of the dielectric tensor, ϵ^a, is small. In other words it means that there should be very little absorption or emission. This limitation is not severe for the CTS

experiments since they anyway require that harmonics of electron cyclotron resonance which have frequencies in the sensitivity range of the CTS receiver, are located outside plasma volume.
In the CTS group, a weakly relativistic ray-tracing code is used [63]. Using this code, the position of the scattering volume, as well as the projection angle, are estimated after the experiments. In order to evaluate the size of the overlap volume, an iterative technique is used. Typically, the probing and the receiver beams are approximated by five rays: one central one and four which denote the width of the beam at $1/e^2$ of the maximum power level. Because ray-tracing does not reflect the evolution of the Gaussian beam along its trajectory, at the first iteration, where the position of maximum overlap is identified the distance to the launching and receiver mirrors is calculated, then the beam width is recalculated taking into account that

$$w = w_0 \sqrt{1 + \frac{z^2}{z_R^2}}, \tag{4.5}$$

where z is the distance along the beam from the focal point, w is beam waist and $z_R = \pi\omega_0/\lambda$ is the Rayleigh range. A new value of the beam width is substituted into the ray-tracing program and a better estimate of the size of the overlap volume and overlap integral, O_b, is obtained.

4.2.3 Beam-tracing

Ray-tracing is a very powerful and fast tool for the CTS experiments. However, ray-tracing does not take beam diffraction into account. In the CTS experiments waves in O-mode do not experience much diffraction, but it is of particular importance for the work on sawtooth destabilization by electron cyclotron current drive (ECCD), see Chapter 9. In order to be able to simulate correctly the current deposition profile, the beam-tracing code TORBEAM is used [78]. In this code, the diffraction and refraction mechanisms are combined with the simplicity of the ray-tracing. In the code the ray-tracing is used to calculate the position of the wave front. At each time step the transversal structure of the beam is calculated with greater accuracy, which allows to calculate the beam absorption profile, from which ECCD can be calculated.

4.3 Alignment Check of Quasi Optical Receiver Mirrors of the CTS Diagnostic by Measurements of Sawteeth

As it is discussed in Section 4.1, alignment is very important for successful CTS experiments. There the methods of the alignment check and correction are discussed. However, information on the alignment is essential during

the experiments. One of such checks is described in Section 4.2. Depending on the relative placement of the receiver and probe mirrors, the overlap sweep [25] is very sensitive to either rotation angle misalignment (TEXTOR) or elevation angle misalignment (ASDEX Upgrade). At the same time there was no reliable method how to control elevation (TEXTOR) or rotation (ASDEX Upgrade) angle misalignment.
A new elevation angle alignment check is developed for the TEXTOR tokamak. The magnetic field for this check should have such a value that ECE from the plasma which is detected by the receiver should originate from the resonance layer which intersects the $q = 1$ surface. The bisection point exactly halfway between our calculated values should lie at $z = 0$, because plasma equilibrium in TEXTOR is vertically symmetric with respect to the equatorial plane if no vertical shift is applied. This makes the CTS experiments during the alignment check of the discharge practically impossible due to a very slow rate of changing the toroidal magnetic field in tokamaks (for TEXTOR and ASDEX Upgrade a typical value is ± 0.1 T/s). It means that ramping the magnetic field in the CTS discharge from 2.6 T (at this value of the magnetic field the fast ion CTS diagnostic normally works) down to 1.9 T (at this value of the magnetic field the alignment check was performed) would take approximately seven seconds, which is longer than the duration of a typical TEXTOR discharge. The CTS receiver in the ECE

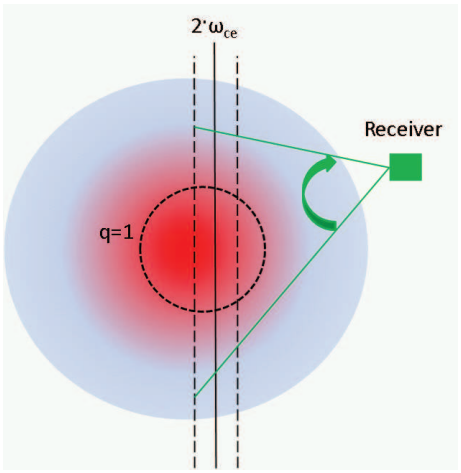

Figure 4.7: A sketch illustrating the principle of post factum elevation alignment check using the CTS receiver as an ECE radiometer. The $q = 1$ magnetic surface is shown as a black dashed circle; black vertical and dashed lines show the lower- and the upper-most positions of electron-cyclotron resonance which the receiver is sensitive to; the green box denotes the steerable mirror of the receiver, solid green lines represent the beam of EC waves propagating into the receiver; the green arrow indicates the direction of the receiver mirror sweep.

radiometer regime is sensitive to the changes in electron temperature. The electron temperature changes rapidly during a sawtooth event ($\sim 10\mu s$). In order to find the location of the intersection of the resonance layer with the $q = 1$ surface, the receiver beam is swept across the plasma, as it is shown in Fig. 4.7. This is made by scanning the elevation angle of the receiver mirror. When the receiver beam is swept across the $q = 1$, inverse sawtooth oscillations are followed by direct sawtooth oscillations when the received radiation originates from inside the sawtooth inversion radius.
A time series of the ECE signal (channel no. 19 of the CTS receiver) from TEXTOR discharge 112963 is presented in Fig. 4.8. In this discharge, the toroidal magnetic field on axis was $B_t = 1.9$ T. One can clearly see that the signal in the beginning of the scan originates from outside of $q = 1$ surface because the signal variation has a clear inverse-sawtooth shape. At around $t = 2.9$ s an inverted sawtooth signature in the signal vanishes (Fig. 4.8(b)) and then appears again as a normal sawtooth. This is a clear sign of crossing of the $q = 1$ surface and the signal originates from inside the inversion radius. Continuing the sweep, the $q = 1$ surface is crossed again which is indicated by the change in the sawtooth signature in the receiver signal from sawtooth-like to inverted sawtooth(Fig. 4.8(c)).
There are a number of reasons why the transition between normal and inverted sawtooth is so not abrupt. The first reason is geometrical. On the magnetic surface where $q = 1$ exactly, electron temperature and density should not change at all. In the very proximity of the surface, changes are small. Secondly, the received beam is Gaussian and has a finite width. It means that a weighted average over a beam width takes place, so it is difficult to spot a precise location of the transition. An effect of a finite bandwidth of channels in the CTS receiver is negligible.
Location in the plasma where the detected radiation originates from, is calculated using the ray-tracing code. If the elevation alignment is correct, the z - coordinate of both locations where the resonance layer intersects the $q = 1$ magnetic surface should by symmetric with respect to the equatorial plane. For the discharge which is discussed here, the z - coordinate of the intersection points are $z = -14.1$ cm and $z = 12.7$ cm. An error-bar of the measurements is $\sigma_z = 1.6$ cm, so the elevation beam alignment is correct within the uncertainty of 1.5°.

4.4 Calibration

A CTS receiver needs a very careful calibration. As one can see from the equation of transfer (Eq. (2.15)), the received spectrum is proportional to the scattering function Σ and to the multiplicand which contains constants, electron density and the overlap integral. The multiplicand does not depend on the fast ion distribution function and therefore acts as a scaling factor.

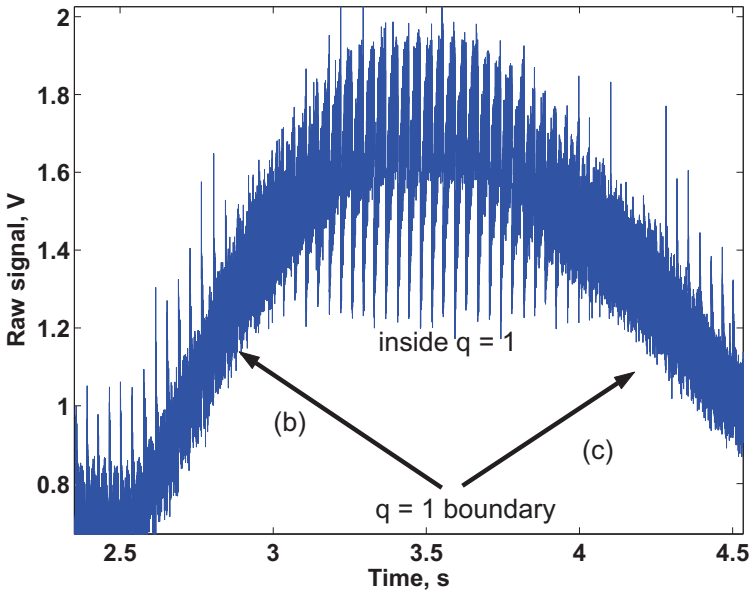

(a)

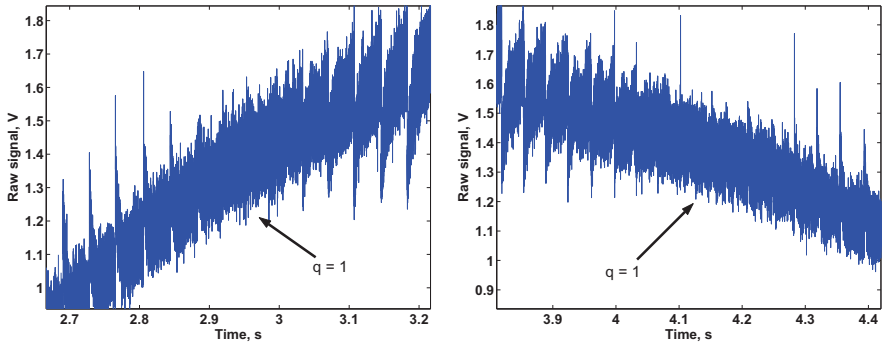

(b) (c)

Figure 4.8: (a) Time trace of raw signal in channel 19 of the TEXTOR CTS receiver during the elevation angle scan (rotation angle 0°) in TEXTOR discharge 112963 in X-mode. The scan is performed from bottom to top with crossing $z = 0$ plane. The time span when the radiation originates from inside the $q = 1$ magnetic surface is marked, arrows show the moments when the receiver beam crossed the $q = 1$ surface. The signal at these moments, (b) and (c) are indicated by arrows, zoomed in and showed in (b) and (c).

The scaling factor can be determined during fitting. Taking into account that each detection channel is equipped with its own band-pass filter, detection diode with an individual characteristic (see Fig. 3.10 for example) and that groups of the detection channels are treated by different amplifiers and attenuators after leaving the splitting stage, the absolute values for the calibration coefficients can be arbitrary but the ratio between the calibration coefficients of various channels should be found correctly.
It is unavoidable to use the scaling factor anyway during the data analysis because the ray-tracing code (see Section 4.2) determines the position of an overlap volume accurately but the size of the overlap and its comparison with experimental results is a large source of errors due to uncertainties in plasma parameters and the diagnostic alignment.
The receiver can be cross-calibrated with another plasma diagnostic, i.e. ECE or incoherent Thomson scattering or calibrated directly with the black-body sources of radiation. Each method has its own advantages and disadvantages.

4.4.1 Liquid Nitrogen Calibration

This method of calibration is actively used to calibrate the ASDEX Upgrade CTS receiver. The CTS receiver is sensitive to the radiation power at the level of a fraction of a μW. Thus it is sensitive to the difference in radiation intensities of black bodies at room temperature and liquid nitrogen temperature. Assuming that the receiver works in a linear regime, the calibration is inferred. The signal in each channel can be calibrated using the following relation:

$$S(V) = k \cdot (T_{BB} + T_{noise}), \tag{4.6}$$

where S is a measured signal (in V), k is a calibration coefficient, T_{BB} is black body temperature and T_{noise} is noise temperature. The noise temperature shows an effective temperature of the receiver resulting in non-zero signal from measurements with zero temperature. Typically, for ASDEX Upgrade receiver $T_{noise} \approx 5 - 10\ eV$. Fig. 4.9 shows a photo of the receiver at ASDEX Upgrade with calibration hardware. The chopper mirror which is mentioned above, is a mirror which can be put into the transmission line by an electrical motor that switches views between a room temperature black body and a special bucket with liquid nitrogen. For better statistics, many repeat measurements are conducted. In order for the thermal radiation spectrum in the mm-range originating from the liquid nitrogen bucket to be similar to the spectrum of a black body, the inner walls of the bucket are covered with a special absorbing material called *ecosorb*.
Liquid nitrogen calibration does not include the instrument function of the RF transmission line (which includes mirrors, polarisers, a diamond window and over 70 meters of overmoded waveguide with miter bends) into account.

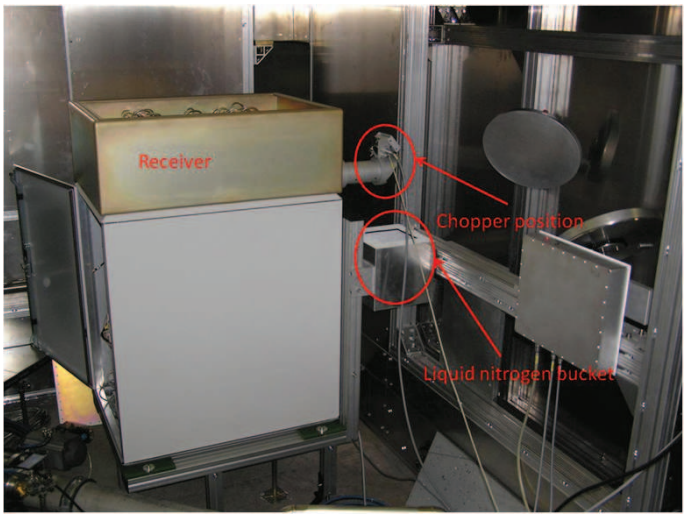

Figure 4.9: Photo of ASDEX Upgrade CTS receiver. Red ellipses denote the bucket for liquid nitrogen and the chopper mirror.

The instrument function of the transmission line has to be included in the calibration at a later stage, since it might be a source of uncertainties. However, this method of calibration may be used absolutely independently from any other activities which take place at the experimental site.
The feasibility analysis for improvement of liquid nitrogen calibration by adding a hot source into the calibration scheme was carried out. SiC was chosen as material for the viewing surface (of the same size as a cold source at liquid nitrogen temperature) with operating temperature of 800 °C because it mimics the black body emission for our range of frequencies. Such a value was chosen as minimum possible temperature which allows using the third point on the calibration curve significantly different from the point corresponding to room temperature. However, technical difficulties made this project problematic: the radiation power of a hot source at 800 °C with minimum possible size would radiate more than 5 kW. The receiver at ASDEX Upgrade will be moved to a new location in the NBI control room. Approximately 10 m^2 are dedicated for the CTS diagnostics, this space is limited with walls and has no technical capabilities of maintaining room temperature when such powerful heat sources are used.

4.4.2 Cross-calibration with Another Diagnostic

Using this method, the receiver is calibrated assuming radiation which is leaving the plasma is black-body radiation. During the calibration, the receiver is working as an ECE-radiometer. In order to be able to relate the received signal with the black-body radiation, we should assume that

the radiation originates from an optically thick region. Thus the receiver's polarizers are set to X-mode and the magnetic field is chosen such that the frequencies to which the receiver is susceptible to correspond to the second harmonic of electron-cyclotron resonance in the centre of the plasma. When the black-body condition is fulfilled, the intensity of ECE obeys the Rayleigh-Jeans law:

$$I_{ECE} = \frac{\omega^2 T_e}{8\pi^2 c^2} \tag{4.7}$$

A very big advantage of this method is that the calibration curve includes an instrumental function of the transmission line, which is very important due to possible frequency selectivity of windows, waveguides, etc. However, the disadvantage is that this method relies on calibration of another diagnostic and that is a source of possible error. Another aspect which one has to be careful about is a possibility to run the receiver in the non-linear regime. It is implied during the CTS measurements that the output of the receiver (V) scales linearly with the SPD of received radiation (eV). However, the linear scaling breaks if the amplifiers and/or diodes reach certain output power because the amount of radiation seen by the receiver during cross-calibration shots is significantly higher than in CTS discharges. Thus one has to always monitor that the amplifiers never reach their 1 dB compression point. 1 dB compression point sets an operational limit for a linear amplifier. It is defined as an input power at which the output power of the amplifiers is 1 dB less than expected by a linear approximation $P_{out} = Gain \cdot P_{in}$.
Another possible source of error is mapping of the locations of origin of received radiation by the different diagnostics on normalized plasma radius, ρ.

A big advantage of the cross-calibration method in comparison with liquid nitrogen calibration is a large amount of data points at different temperatures for proper statistics. Referring to the liquid nitrogen calibration technique one has to keep in mind that the slope reconstructions having just two points on the diagram is correct, assuming that everything works linearly. However, having so few data at different temperatures makes it impossible to recognize non-linear regime of the receiver or a hardware failure. An example is shown in Fig. 4.10, which depicts cross-calibration graph of the ASDEX Upgrade receiver with an ECE diagnostic during discharge 26550. Red stars denote measurements made by the CTS receiver and the ECE diagnostic, blue line shows the slope obtained by least square fitting of the cross-calibration data and additionally data obtained at zero temperature (with no plasma in the vessel). The magenta line shows the results of fitting excluding zero-temperature data. Ideally, in case of no hardware failures and good statistics these two lines should be indistinguishable. However, one can clearly see that for channel 1 (Fig. 4.10(a)) the slopes of blue and magenta lines differ a lot. The results of the same calibration for channel 32 (Fig. 4.10(b)) look correct.

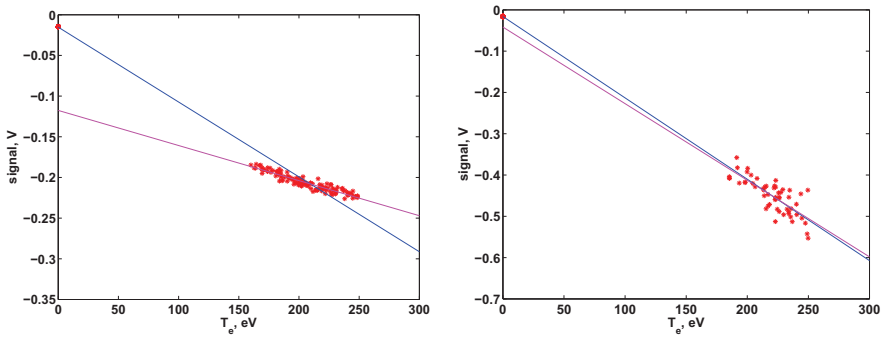

(a) (b)

Figure 4.10: ECE data plotted against raw CTS data in ASDEX Upgrade discharge 26550 for channel 1 (a) and channel 32 (b). The blue and magenta lines show calibration slopes for data included measurements without plasma (zero temperature) and excluded, respectively.

Very similar to the ECE cross-calibration technique, cross-calibration with incoherent Thomson scattering was implemented on TEXTOR. There the collective Thomson scattering diagnostic was calibrated by the incoherent Thomson scattering diagnostic. The resulting calibration curve is shown in Fig. 4.11. Fig. 4.12 shows a raw signal from the receiver in TEXTOR discharge 111509 averaged over 1 ms and the same data after calibration was applied. Cross-calibration on TEXTOR uses temperature data from incoherent Thomson scattering diagnostic.

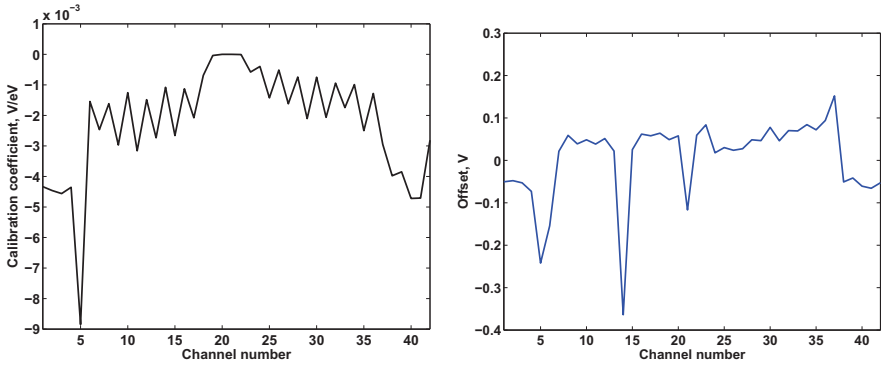

(a) (b)

Figure 4.11: Cross-calibration of the CTS receiver at TEXTOR with the incoherent Thomson scattering diagnostic. The calibration curve is shown in (a); DC offset of the ADCs is depicted in (b)

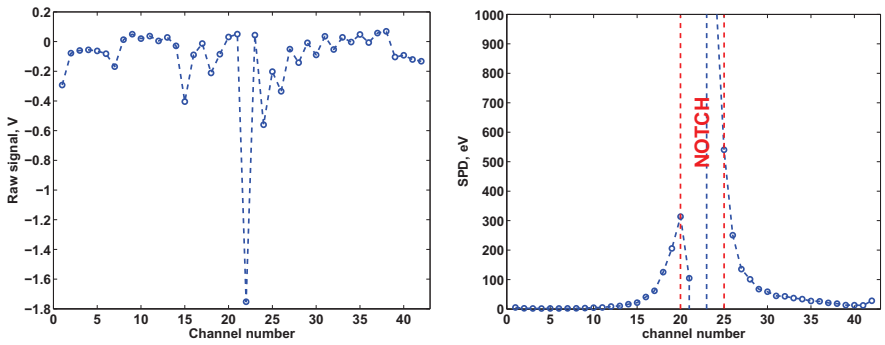

(a) (b)

Figure 4.12: Shot No.111509, averaged over 1 ms between 2.811 s and 2.812 s (102 samples) (a) Averaged raw signal from the receiver; (b) The same signal after calibration was applied

4.5 Background Subtraction and Secondary Emission in the CTS Data

The CTS receivers both on TEXTOR and ASDEX Upgrade are sensitive to the frequencies ±5 GHz around the probing frequency (110 GHz and 105 GHz, respectively). The received radiation consists of scattering signal and

ECE background. In order to distinguish between the two, the gyrotron power is modulated. For CTS experiments, the gyrotron usually works with 50% duty cycle, 2 ms on/2 ms off. Due to the fact that the gyrotron power is not absorbed in the plasma and may occasionally damage the first wall tiles and/or other diagnostics, a total gyrotron energy limit per discharge is applied. Thus, when CTS measurements require long acquisition (for example during the overlap sweep), the gyrotron duty cycle is altered. For frequencies far enough from the probing frequency, i.e. corresponding to the first and the last channels in the receiver, no scattering is expected. The signal in these channels should only be due to the background ECE radiation. Thus, these channels are called the background channels. The background subtraction technique assumes that the background signal in any channel is a linear combination of signals in the background channels. The decomposition coefficients are calculated during the gyrotron off periods, when all the channels receive only ECE radiation. During the gyrotron on period, the background level is calculated using information about the background level from the ECE background channels (channels 1 and 50 in the ASDEX Upgrade CTS receiver and 1 and 42 in the TEXTOR CTS receiver).
In order to check how well the background fitting works and the validity of the assumption that the ECE background during gyrotron-on periods can be represented as a function of signals in the background channels, so-called fake pin-switch discharges were conducted. In these discharges the gyrotron is not operated but during the data analysis at certain times the signal is considered to be scattering together with the background subtraction. Thus a test for the background fitting can be performed because in the absence of probing radiation there is no scattering, so an estimate of the ECE background should coincide with the measurements. The results of such a test are shown in Fig. 4.13 for TEXTOR discharge 111605, channel 32 prove that the background fitting method is reliable.

A time trace of the ECE background channel during an overlap sweep is shown in Fig. 4.14. This fact is used for sanity checks of the experimental result. Sometimes there is a non-background signal in the ECE background channels, so called *secondary emission signal*, see Fig. 4.15 for example. Secondary emission decreases the accuracy with which the fast ion distribution function can be estimated. Sometimes the fast ion CTS signal is on the same order of magnitude as the secondary emission signal, whose origin is yet not completely understood.

Firstly, the check was performed to clarify whether the gyrotron might be the source of it. Stray radiation measurements of the gyrotron radiation by the receiver with blocked transmission line disproved this hypothesis. Secondly, it was believed that the secondary emission signal is associated with absorption and following re-emission of the probing radiation either at

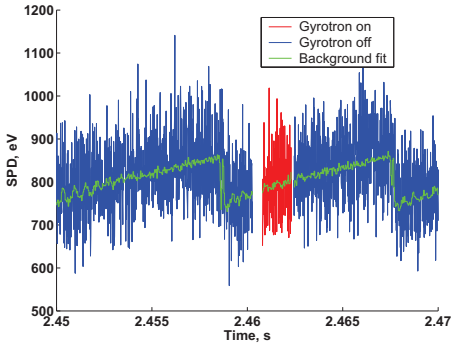

Figure 4.13: Time trace of the CTS signal in ch.32 for TEXTOR discharge 111605 (fake pin-switch shot). Blue shows gyrotron off periods, red denotes gyrotron on periods, gyrotron power in the experiment is zero. Green is a fit of the ECE background.

the fundamental or at the second harmonic of electron cyclotron resonance. Parameter scans of the edge plasmas in TEXTOR and ASDEX Upgrade do not reveal any consistency in the secondary emission signal behaviour. However, recent experiments at ASDEX Upgrade, performed at higher magnetic field showed a simultaneous drop of the secondary emission signal and decrease of signal to noise ratio. In an ideal CTS experiment the probing beam is not absorbed in the plasma, immediately after leaving the plasma it should disappear. The reality is that at least some part of the gyrotron radiation is reflected from tiles on the high field side with arbitrary polarization and bounces between the walls and weakly interacts with plasma. If such a bouncing takes place next to the receiver antenna, it might cause an unpredictable signal in the receiver. Moving a resonance at the high field side into the plasma creates a weak dump which might reduce the amount of the secondary emission signal significantly or get rid of it completely. This hypothesis needs more experimental proofs which are to be obtained during the next campaign at ASDEX Upgrade in 2012.

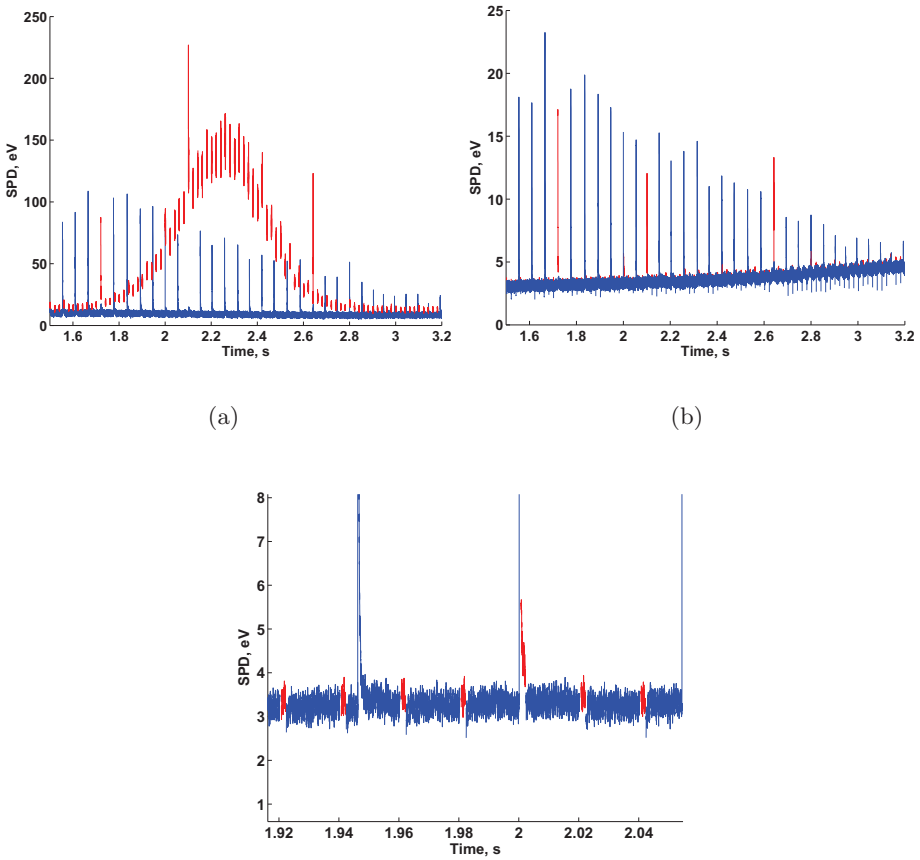

Figure 4.14: Absence of the secondary emission signal in the TEXTOR overlap sweep discharge no. 111742. Blue line denotes gyrotron-off periods, red line denotes gyrotron-on periods. (a) Time trace of the bulk channel no. 27, overlap is clearly visible; (b) Time trace of the background channel no. 3 and its zoomed image (c)

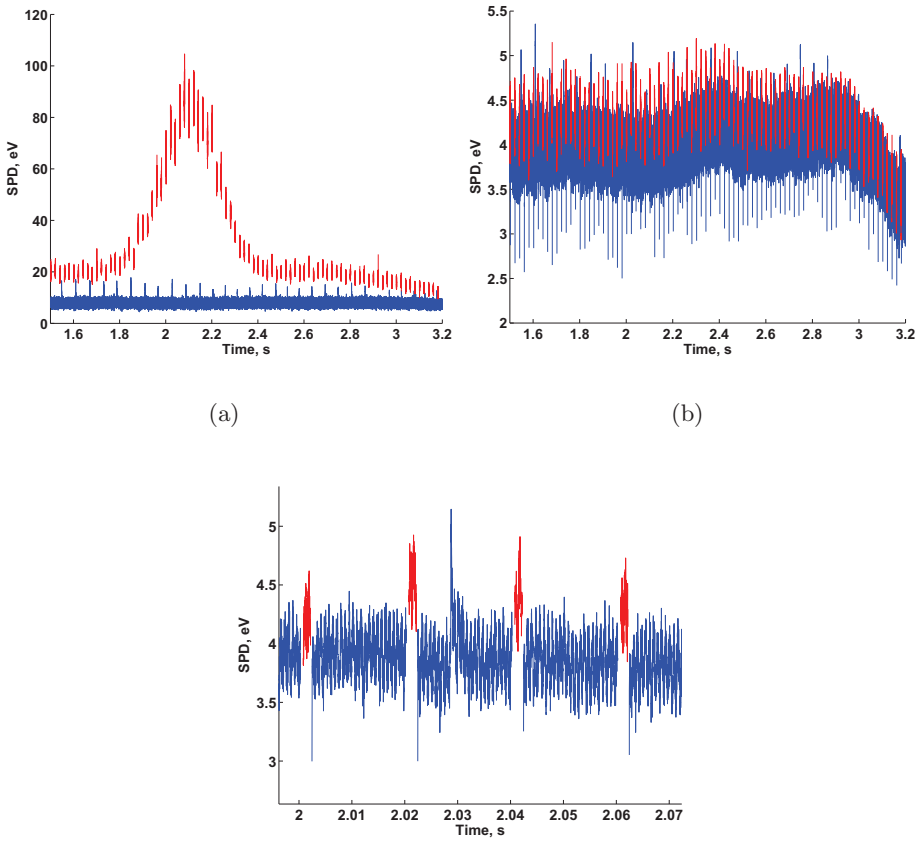

Figure 4.15: Secondary emission signal in the TEXTOR overlap sweep discharge no. 111513. Blue line denotes gyrotron-off periods, red line denotes gyrotron-on periods. (a) Time trace of the bulk channel no. 27, overlap is clearly visible; (b) Time trace of the background channel no. 3 and its zoomed image (c)

Chapter 5

Recent CTS Results

The idea of using CTS for diagnosing the fusion plasmas came up in the 1970's [79]. It was proposed to use far infra-red laser as a source of probing radiation. Ion temperature measurements with laser-based CTS were performed on the TCA tokamak [80]. However, only one measurement during a discharge was possible because of the operating regime of the laser. The signal-to-noise ratio was also limited by a very short length of a laser pulse. The laser-based CTS was also installed on the UNITOR tokamak [81]. A fast ion CTS system using a CO_2 laser was designed for ALCATOR-C Mod [82], but it was never built. In the 1980s high-power gyrotrons (free electron masers) were developed and proposed as sources of probing radiation for CTS. Using mm-waves in the diagnostic allows a wide choice of scattering geometries. Another advantage of using gyrotrons is a possibility of conducting temporally resolved measurements. Microwave-based CTS diagnostics were installed in TFTR (at 60 GHz) [83], JET [84], Wendelstein 7-AS [85], TEXTOR [1,23,25,72,86–88], FTU [89], ASDEX Upgrade [24,26,71,72,90], and LHD [91, 92]. This diagnostic is also included in the ITER baseline design. Here recent results of the CTS group at Risø DTU are highlighted.

5.1 Strong Signals in the CTS Receiver from Plasmas with Tearing Modes and a Gyrotron Probe Beam

A magnetic island is a structure in a plasma which is created by magnetic field lines reconnection events. The physics of magnetic reconnection is not entirely clear yet. There is a number of models which try to reveal its nature [47], but only resistive reconnection in collisional plasmas is comprehensively described by Kadomtsev [43]. Kadomtsev's model is not applicable for high temperature plasmas. Magnetic islands in the plasma core are called tearing modes if they are caused by lack of inductive current (classical tearing mode)

or bootstrap current (neoclassical tearing mode, NTM). The topology of a magnetic island is shown in Fig. 5.1. In the future, NTMs can be suppressed by driving current (which can be created by electron cyclotron current drive, or inductively by reducing the plasma resistance due to heating) in the O-point of the island but for this a reliable detection and feedback system should be designed. In order to detect the O-point of the island a line-of-sight ECE diagnostic was installed on TEXTOR [93]. During the tearing mode experiments on TEXTOR, anomalously large structured signal was found. The mode had $(m, n) = (2, 1)$ structure generated by the DED coils installed at TEXTOR and was located on the q = 2 surface. The spectral shape of the strong signal and its onset with respect to the phase of the island vary with the density in the plasma [93]. One can clearly see from Fig. 5.2 that strong structures appear in the spectrum with the same frequency as the island passage frequency. The strong signal at 137.5 GHz is present every time the island (or a part of it) is inside the overlap volume in this discharge. Three bright lines are chirping down during the onset of the signal at 137.5 GHz. At the time when the signal at 137.5 GHz disappears, the three lines are chirping back up. Fig. 5.2 should be taken as example of a variety of spectral shapes. The strong signal can appear at other densities, magnetic fields, probing frequencies, or heating power. 140 GHz gyrotron launching in the X-mode was used for ECRH heating, as well as a source of probing radiation for the CTS diagnostic. Low-threshold backscattering parametric decay instability was suggested as a possible explanation for the observed phenomena [94].

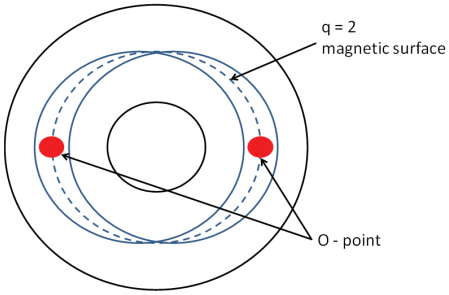

Figure 5.1: A sketch of a $(m, n) = (2, 1)$ magnetic island, O-points are marked by red circles.

5.2 Fast Ion Redistribution Due to Sawteeth

Sawtooth oscillations is an internal $(m, n) = (1, 1)$ kink mode. It was reported that fast ions can stabilize sawteeth [96–102]. It was also reported that sawtooth oscillations redistribute fast ions from inside the inversion radius [17]. More details on the sawtooth instability can be found in Sec-

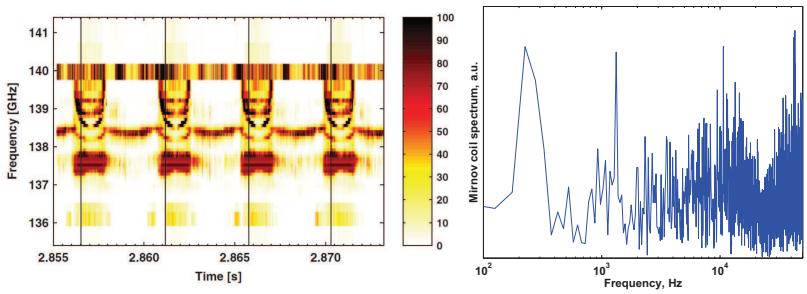

(a) (b)

Figure 5.2: (a)Spectrum of measured radiation of the TEXTOR discharge no. 107128 in presence of $(m, n) = (2, 1)$ rotating island. Vertical lines show when the O-point of the island passes through the ECRH beam. Figure is taken from reference 95; (b) Fluctuation spectrum of one of the Mirnov coils in discharge 107128 during the CTS measurements.

tion 2.2.4 and references therein. The CTS experiments at TEXTOR were performed in order to investigate fast ion redistribution due to sawtooth oscillations. Fast ions in this experiment originated from 50 keV, 1.2 MW co-I_p highly tangential deuterium NBI launched into deuterium plasmas. The experiments showed that the MHD activity associated with sawteeth mainly interacts with fast ions with nearly parallel velocity to the magnetic field [87]. Fig. 5.3 shows CTS measurements at the same radial location but at two different projection angles: 39° and 83°. At the projection angle of 39° the CTS diagnostic is mostly probing fast ions with a large value of pitch, while at projection angle of 83° the diagnostic is more sensitive to the fast ions with low pitch [68]. It is clearly visible that in the latter case there is no clear correlation between the sawtooth activity and changes in total fast ion density, see Fig. 5.3(b). However, fast ions density in the overlap volume in the experiments with projection direction more parallel to the magnetic field experience strong reduction at the moment of the sawtooth crash (Fig. 5.3(a)). There was no evidence of fast ion redistribution due to sawtooth in the experiments where overlap volume was located outside the sawtooth inversion radius [88]. It was also shown in reference 88 that fast ions with energy close to the maximum energy of the injected beam also oscillate with the same frequency as the sawteeth but the oscillation is out of phase with that of the bulk ions. The fast ions density decreases before the crash. The results displayed in Fig. 5.4 show that fast ions at different energies respond differently to the sawtooth crash and that there is a phase shift between oscillations in electron temperature and response

in fast ion channels. The CTS geometry of the experiments was the following: R = 1.79 m, $\phi = 110°$. The time shift in the response of $g(u)$ at high velocities is explained by changes in collisional slowing down of fast ions at high velocities (their slowing down is mainly due to collisions with electrons). The electron density and temperature in the overlap volume rapidly decrease at the moment of the sawtooth crash and then they recover until the next crash. These oscillations affect slowing down time. The effect described above was also obtained with the basic Fokker-Planck code for homogeneous plasma [25].

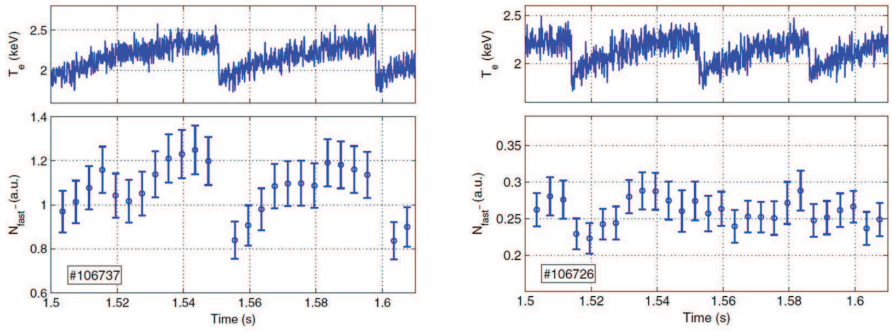

(a) (b)

Figure 5.3: Electron temperature in the core measured by the ECE spectrometer over partial 1D density of fast ions, $N^{-}_{fast} = \int_{-2\cdot10^6}^{-1.2\cdot10^6} g(u)du$; (a) $\phi = 39°$; (b) $\phi = 83°$. Figure is taken from reference 87.

5.3 Comparison of Fast Ion CTS Measurements on ASDEX Upgrade with Numerical Simulations

Comparison of the CTS results on ASDEX Upgrade with numerical simulations was performed in order to benchmark numerical codes with the experiment [90]. The experiments were performed in deuterium plasmas with deuterium NBI. Two different NBI sources were used in the experiments: S3 and S8. Each of them has similar on-axis injection geometry and a power of 2.5 MW. The acceleration voltage of NBI S3 is 60 kV and that of S8 is 93 keV. Fig. 5.5 shows a comparison of the measurements with the simulations. The simulations were done with two Monte Carlo codes, TRANSP/NUBEAM and ASCOT. The steady-state plasma deposition profile was assumed in the simulations. The measurements and the simulations

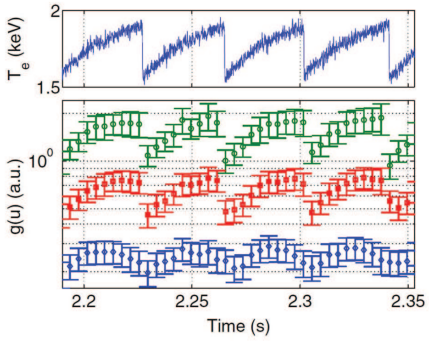

Figure 5.4: Time trace of electron temperature measured with the ECE spectrometer (above) shows moments of sawtooth crashes. The bottom graph shows time traces of $g(u)$ values at certain values of u: $1.3 \cdot 10^6$ m/s (green), $1.6 \cdot 10^6$ m/s (red), $1.9 \cdot 10^6$ m/s (blue). Scattering geometry: R = 1.79 m, $\phi = 110°$. Figure is taken from reference 88.

agree qualitatively: they both demonstrate skewness of the 1D velocity distribution function. The fast ion phase space density is higher when both neutral beam injectors are switched on. However, there are quantitative discrepancies between the measured and simulated distribution functions. There is a tendency to measure larger signals than would be expected from the present theory.

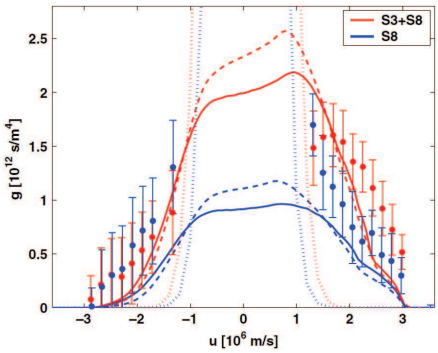

Figure 5.5: Comparison of the CTS measurements at plasmas with two different scenarios (circles) with the Monte Carlo simulations performed with TRANSP/NUBEAM (solid line) and ASCOT (dashed line). Red color denotes heating scenario with two neutral beams, S3 and S8, blue shows heating scenario with only one NBI, S8. Thin dashed lines show distribution of bulk ions. Figure is taken from reference 90.

5.4 Fuel Ion Ratio Measurements with CTS

In ITER or future fusion reactors, the D-T reaction takes place in the core of the plasma, where it is fully ionized and no spectroscopy is available which is capable to measure the ratio between the isotopes. Thus, developing a diagnostic which can measure the fuel ion ratio in the core is of great importance for successful ITER operation.
It was noticed that in the CTS experiments, when the angle ϕ is close to 90°, the scattering spectrum is sensitive to the waves in the frequency range of harmonics of ion cyclotron waves. These signatures are related to the ion cyclotron motion and ion Bernstein waves. For detection of the spectral signatures, the CTS diagnostic was upgraded in order to improve its frequency resolution. The details of the upgrade can be found in Section 3.5 and in reference 75.
Experiments in TEXTOR plasmas [103] showed that the diagnostic is indeed sensitive to the ion cyclotron and ion Bernstein waves. Fig. 5.6 shows a ϕ angle scan performed during discharge 111796 in TEXTOR. During this discharge, both probe and receiver beams were swept in such a way that the beams sustained good overlap at the same radial position, only the ϕ angle was changing. The scan was 20° wide and was centred around $\phi = 90°$ to the magnetic field. For ϕ angles close to perpendicular, the ion cyclotron structure remained very clear but when the angle was more than 3° off the perpendicular direction, the ion cyclotron structure vanished.

A scan of different fuelling schemes was performed during the same experimental campaign. The ratio between hydrogen and deuterium ($R_H = n_H/(n_H + n_D)$) was steadily changing. In addition, experiments with fuelling by ^{3}He were performed. The results of these measurements one can see in Fig. 5.7. The frequency separation between the peaks corresponds to cyclotron frequencies of hydrogen, deuterium and ^{3}He in the overlap volume.

In reference 104 it was shown that contributions of ion cyclotron and ion Bernstein waves cannot be decoupled from the CTS spectra. However, they can be treated together and the density ratio between different species in the plasma can be inferred. Reference 105 provides with the results of the first measurements of the isotope composition in the core of TEXTOR plasmas. The results were compared with the results of spectroscopy measurements at the edge. The results agree qualitatively, but discrepancy in absolute values is observed. This could be either due to difference in plasma composition at the edge and in the core, or due to an error in one of the methods.

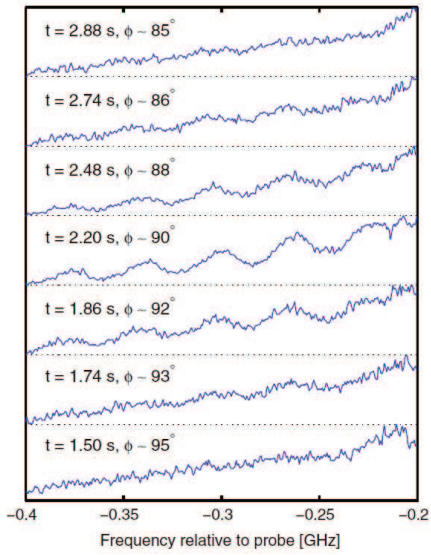

Figure 5.6: Measured CTS spectra in TEXTOR discharge 111796. The presented scan shows how the spectra change with changing in ϕ angle. The peak separation in the structure of spectra which are close to 90° is 40 MHz, which corresponds to the proton cyclotron frequency in the measurement volume. Figure is taken from reference 103.

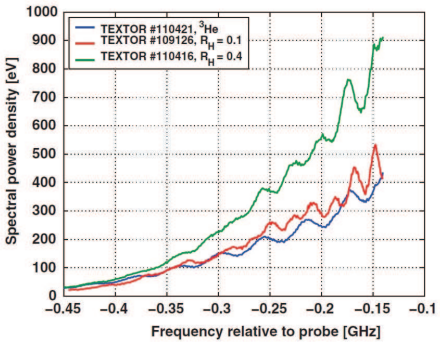

Figure 5.7: Measured CTS spectra at the ϕ angle close to perpendicular to the magnetic field with different fuelling schemes. Blue: ^{3}He plasma, TEXTOR discharge 110421; red: $R_H = 0.1$, TEXTOR discharge 109126; green: $R_H = 0.4$, TEXTOR discharge 110416. Figure is taken from reference 103.

Chapter 6

Comparison of Measured and Simulated Fast Ion Velocity Distributions in the TEXTOR Tokamak

This chapter is based on the article 1 of which I am the first author. Simulations were performed by Tuomas Koskela (Aalto University), Otto Asunta (Aalto University) and Mattia Albergante (EPFL).

Here we demonstrate a comprehensive comparison of CTS measurements with steady-state Monte Carlo simulations performed with the ASCOT and VENUS codes. The measurements were taken at a location on the magnetic axis as well as at an off-axis location, using two projection directions at each location. The simulations agree with the measurements on-axis, but for the off-axis geometries discrepancies are observed for both projection directions. For the near perpendicular projection direction with respect to the magnetic field, the discrepancies between measurement and simulations can be explained by uncertainty in plasma parameters. However, the discrepancy between measurement and simulations for the more parallel projection direction cannot be explained solely by uncertainties in plasma parameters. Here anomalous fast ion transport is a possible explanation for the discrepancy.

6.1 Introduction

Simulations of fast ions in tokamaks and stellarators are done using a wide variety of codes. Codes can be benchmarked against experimental data to increase the confidence in them if reasonable agreement is found. For this purpose fast ion distribution functions and synthetic CTS spectra can be

computed using the computer codes [90, 106, 107]. Fast ion distributions from CTS results at ASDEX Upgrade at a single location and angle but with different NBI scenarios have been compared with simulations where they agreed qualitatively [90], see Section 5.3. In this chapter the experimentally obtained results from TEXTOR at two radial position and projection directions are compared with simulated distributions of fast ions using the Monte Carlo codes ASCOT [108, 109] and VENUS [110]. The comparison shows good agreement between experimental results and simulations for the plasma center. Discrepancies are observed for off-axis measurements. The discrepancy between the off-axis measurement and the simulation for the nearly perpendicular projection direction with respect to the magnetic field can be explained by uncertainties in T_e and n_e profiles as we find by a sensitivity analysis with ASCOT. However, the disagreement for the more parallel projection direction cannot be explained by the uncertainties in T_e and n_e profiles alone. The discrepancies could be explained by anomalous fast ion transport. The simulations are steady-state; no anomalous fast ion transport is assumed.

6.2 The CTS Experiments on TEXTOR

The measurements were made in four discharges in plasmas with deuterium gas puff and co-current hydrogen NBI. Each discharge had a different scattering geometry (Fig. 6.2). The measurements were performed at the plasma center at R $\approx$ 1.8 m and off the magnetic axis at R $\approx$ 2.0 m at different projection angles to the magnetic field $\phi = 127°$, 138°, 106° and 107°. No significant MHD activity was detected by the Mirnov coils and the soft X-ray diagnostic (SXR) (maximum sampling rate 10^5 samples per second) except sawtooth oscillations. From previous CTS measurements in TEXTOR it is known that fast ions redistribute because of sawtooth crashes [87, 88], see also Section 5.2. As the simulation codes do not take the redistribution into account, we chose measurement periods right before the sawtooth crashes (1-3 ms) for the comparisons. The fast ion slowing down time for the given experimental conditions does not exceed 20 ms, while the sawtooth periods in the discharges discussed here were 40 - 50 ms.
Some key experimental parameters are listed in Table 6.1. Electron density and temperature profiles were obtained from incoherent Thomson scattering (TS) [111] for discharge 111508. From this discharge we obtained shapes of the temperature and density profiles at the end of the sawtooth crash. The TS could not be used for obtaining the profiles for the discharges used in this paper because the TS measurement time window was not located at the end of the sawtooth period. In the discharges considered in this chapter and in discharge 111508, the shape of the density profile was similar before the sawtooth crashes according to the interferometry. The density profile was

scaled for each discharge according to the interferometer measurements. The electron temperature profile was also scaled for all the discharges considered in this chapter according to the ECE spectrometer. The ion temperature was measured by charge-exchange recombination spectroscopy diagnostic.

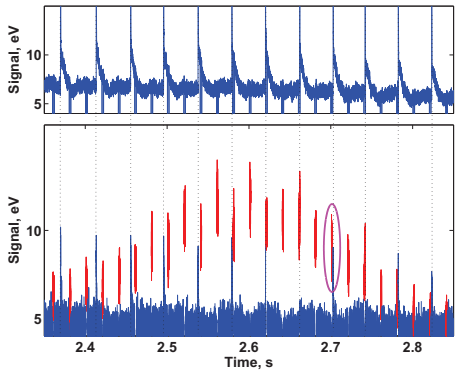

Figure 6.1: Overlap sweep in discharge 111506 with gyrotron modulation. The upper graph shows signal from the ECE background channel (no. 42) and illustrates the times of sawteeth crashes; the lower graph shows the signal in a fast ion channel (no. 37) Red: signal during gyrotron-on time, blue: gyrotron-off time; the magenta ellipse marks the gyropulse which was used for further analysis.

Plasma parameters	111506	111822	111509	111512	σ
Radial position of the scattering volume, m	1.79	1.84	2.0	1.97	$\lesssim 5$ cm
projection angle, $\phi = \angle(\mathbf{k}^{\delta}, \mathbf{B})$	107°	138°	127°	106°	1°
B_t @ magnetic axis, T	2.6				
I_p, kA	437				
n_e @ $\rho = 0$, 10^{19} m^{-3}	3.7	2.9	3.1	3.3	25%
T_e @ $\rho = 0$, keV	2.0	1.5	1.7	2.1	17%
T_i @ $\rho = 0$, keV	3.2	n.a.	3.4	3.4	33%
Co-I_P NBI power, MW	1.2	0.65	1.2	1.2	
Beam ions	Hydrogen				
NBI injection energy, keV	50				

Table 6.1: Plasma and CTS system parameters during CTS experiments. TEXTOR discharges 111506, 111822, 111509 and 111512. σ corresponds to the uncertainty of the measurement.

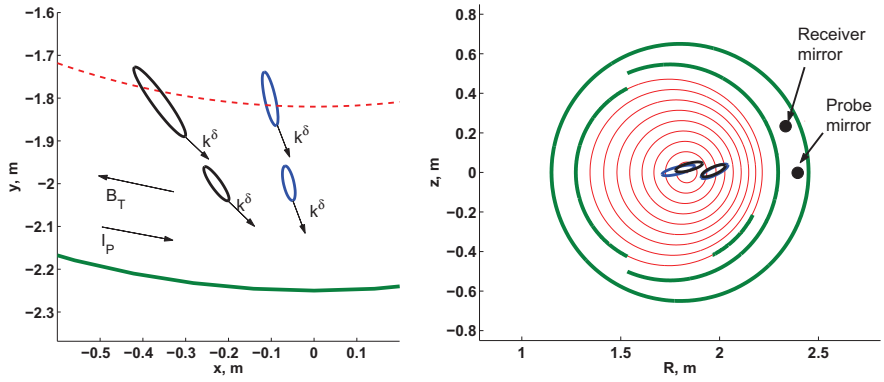

(a) (b)

Figure 6.2: Scattering geometry of the experiments. (a) Top view showing the magnetic axis (red) and the LFS limiter (green); (b) Poloidal view showing estimated flux surfaces (red), limiters and the vacuum vessel (both in green). The blue and black ellipsoids in both figures denote the scattering volumes where black corresponds to $\phi \approx 138°$ and $\phi \approx 127°$; blue to $\phi \approx 108°$ and $\phi \approx 107°$. Black circles represent schematically the position of the receiver and the probe mirrors. Both have similar toroidal location.

6.3 The Monte Carlo simulations

The steady-state 4D distribution of fast ions born from co-current NBI in TEXTOR shots 111506, 111509, 111512 and 111822 are simulated with the ASCOT [108, 109] and VENUS [110] codes. The temporal evolution of the fast ion distribution function was neglected because the sawtooth period was 2-3 times larger than the slowing down time. Changes in T_e and n_e during one slowing-down time prior to the measurements are listed in Table 6.2. ASCOT follows an ensemble of test particles by advancing the guiding center equations of motion [112] using a 5th order error monitoring Runge-Kutta method and by applying Monte Carlo collisions [113] with the background plasma. The initial test particle ensemble is created by injecting neutrals into the plasma and calculating their ionization locations using parametrized ionization cross sections from reference 114.
The drift-kinetic code VENUS is designed for simulating a wide variety of physical phenomena related to fast ion motion. In this work, a recently developed module is used to simulate the NBI in TEXTOR discharges [115]. The code employs a 4th order Runge-Kutta method to solve the single particle equations of motion described in reference 116. The interaction with the background plasma is simulated with the same Monte-Carlo collision

operator used in the ASCOT code. Particle slowing down and pitch angle scattering are described by this numerical technique.
In the ASCOT and VENUS simulations, static magnetic and plasma backgrounds were assumed. The plasma profiles were taken from the experiments (see Section 6.2). Examples of the plasma profiles for discharge 111506 are shown in Fig. 6.3(a). A 2D equilibrium code, DIVA [117], was adapted by both codes to obtain the magnetic field topology. For the simulations presented in this section, ASCOT used $2{\cdot}10^5$ and VENUS used $2.4{\cdot}10^6$ test particles. Test particles were followed until they are slowed down to the double thermal energy (local value for ASCOT and at $\rho = 0$ for VENUS) or until they are lost. An example of the steady-state fast ion density in the poloidal cross-section of TEXTOR in discharge 111506 is shown in Fig. 6.3(b).
Figure 6.4 shows slices of the simulated 4D fast ion velocity distribution functions at (R, z) = (1.8 m, 0 m) and (R, z) = (2.0 m, 0 m) for discharge 111822. There is almost no discrepancy in total fast ion density between the ASCOT and VENUS results calculated for the plasma center, i.e. (R, z) = (1.8 m, 0 m) (Fig. 6.4(a), Fig. 6.4(c)) and slightly off-axis (Fig. 6.4(b), Fig. 6.4(d)). Simulations by ASCOT assumed $Z_{eff} = 1.7$ obtained from the estimate of conductivity, VENUS used $Z_{eff} = 1$. For benchmarking purposes, ASCOT simulations with $Z_{eff} = 1$ were conducted and they showed only small differences with the results obtained by VENUS. None of the codes accounted for re-ionization reactions.

Discharge no.	ΔT_e	Δn_e
111822	7%	5%
111506	12%	8%
111509	10%	5%
111512	11%	4%

Table 6.2: Variations in electron temperature and density within the 20 ms preceding each measurement. The temporal evolution of electron temperature during discharges 111509 and 111512 is monitored only by the ECE spectrometer. On-axis changes in electron temperature were considered as an upper estimate of the changes in the off-axis electron temperature.

6.4 Experimental Data Analysis and Results

We infer 1D projections of the fast ion velocity distribution functions, $g(u)$ (Eq. (2.18)), from the scattering spectra. $g(u)$ is inferred from the SPD using a Bayesian least squares fitting procedure using the forward model shown in Eq. (2.15) which takes prior information about relevant parameters into account, including those from other diagnostics. More details of the procedure can be found in reference 67. One can see an example of the fitted spectrum

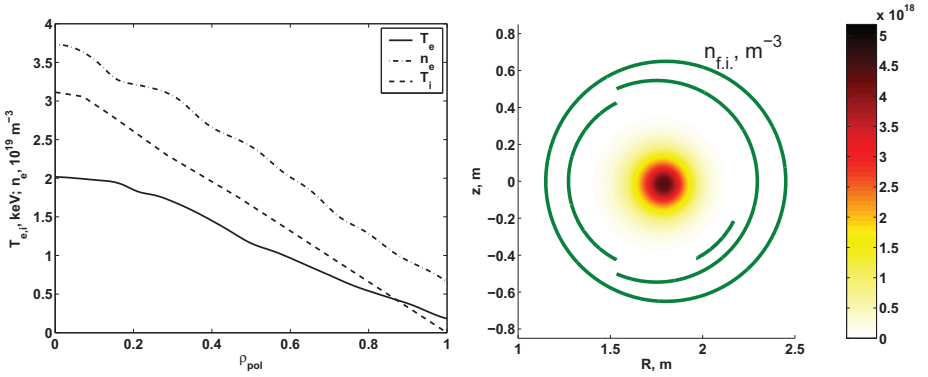

(a) (b)

Figure 6.3: (a) Plasma profiles for ion and electron temperatures and electron density for discharge 111506; (b) Fast ion density in TEXTOR discharge 111506 obtained by ASCOT.

in Fig. 6.5. Here we note that the fit to the experimentally measured SPDs is good compared with the uncertainty of the measurement. The uncertainty on the scattering spectra is estimated as $\sqrt{\sigma_{on}^2 + \sigma_{off}^2}$, where σ_{on} and σ_{off} denote the standard deviations of the spectral power density during gyrotron-on and gyrotron-off periods, respectively.

6.4.1 Results

Positive velocities in $g(u)$ correspond to the direction along $\mathbf{k}^{\delta}$. As illustrated in Fig. 6.2(a), the toroidal component of $\mathbf{k}^{\delta}$ is in the same direction as I_P and the co-current NBI which we use in the four discharges discussed here.

In Fig. 6.6(a), we compare experimental results of $g(u)$ from discharges 111509 ($R \approx 1.97$ m, $\phi \approx 127°$) and 111512 ($R \approx 2.0$ m, $\phi \approx 106°$) which had very similar temperature and density profiles and measurement locations but different projection angles, 127° and 106° (Table 6.1). Even though the difference in the projection angles is only about 20°, the $g(u)$ from shot 111509 ($R \approx 1.97$ m, $\phi \approx 127°$) demonstrates much stronger asymmetry than that from TEXTOR discharge 111512 ($R \approx 2.0$ m, $\phi \approx 106°$), where the projection was taken in more perpendicular direction to the magnetic field. This is consistent with our expectations due to the very parallel injection of the fast ions: the tangency radius of the NBI is approximately 1.65 m. The error bars on $g(u)$ represent the 1σ confidence interval on the phase-space

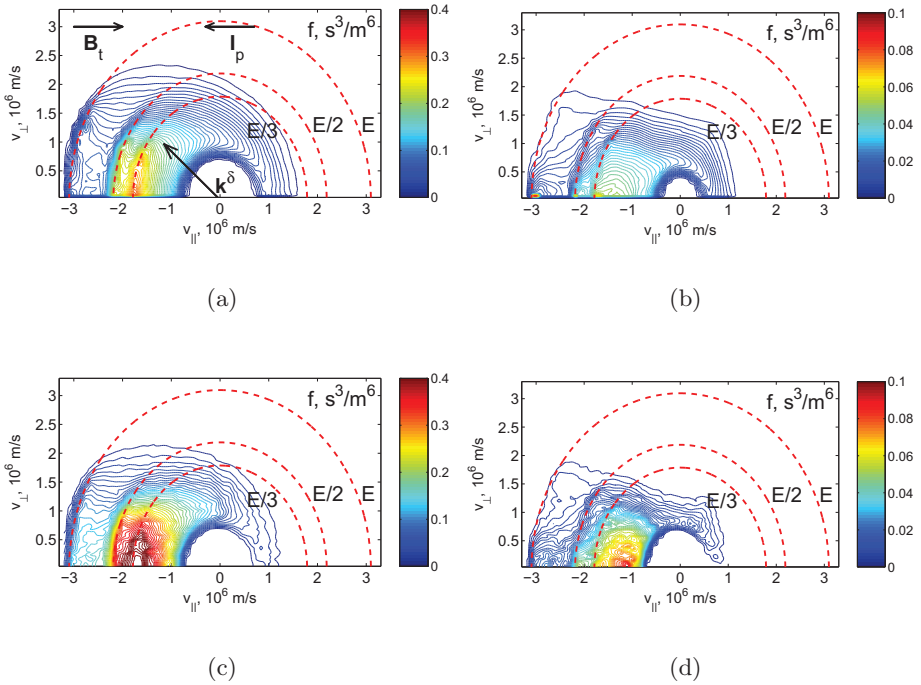

Figure 6.4: Simulated steady-state slowing down velocity distributions of the fast ions at two different radial positions for the TEXTOR discharge 111822; dashed red lines denote beam energy fractions E, E/2 and E/3; (a) R = 1.8 m, ASCOT; arrows show the direction of I_P, B_T and the direction of k^δ along which the projection is taken; (b) R = 2.0 m, ASCOT; (c) R = 1.8 m, VENUS; (d) R = 2.0 m, VENUS.

density. The error bars include prior uncertainties on plasma and CTS system parameters (see Table 6.1), the overlap integral and the spectral power density. The error bars on $g(u)$ are correlated and to some extent can be represented as an uncertainty of a scaling factor of the fast ion velocity distribution function.

For the measurements with projection angles close to perpendicular (Fig. 6.6(b)), $g(u)$ at on-axis and off-axis locations are indistinguishable within the error bars for $u > 1.8 \cdot 10^6$ m/s. These experiments had, however, slightly different temperature and density profiles.

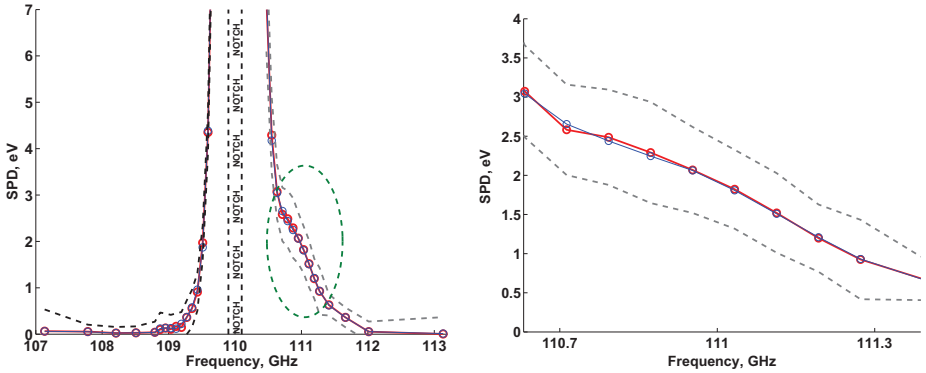

(a) (b)

Figure 6.5: An example of the fitted spectrum for discharge 111822, R = 1.84 m, $\phi = 138°$ shown in (a). Experiment: red line; Fit: blue line. The grey dashed lines are the error bars on the SPD. The green ellipse denotes the zoomed part of the spectrum shown in (b).

6.5 Comparison and Discussion

The absolute comparison between the experimental and simulated results is presented in Fig. 6.7. The general trends of the experiments follow those from the simulations. Fig. 6.6(a) demonstrated the asymmetry of $g(u)$ and that the asymmetry is stronger for larger projection angles, i.e. when $\mathbf{k}^{\delta}$ is more parallel to the magnetic field. The simulations follow these trends shown in the measurements for on-axis and off-axis locations. Another feature common to simulations and experiments is that there is a larger population of fast ions in the plasma center compared with the off-axis case. This can be seen since the absolute values of $g(u)$ are larger on-axis compared with off-axis for similar angles, i.e. comparing Fig. 6.7(b) with Fig. 6.7(d).

In discharges 111822 (R $\approx$ 1.84 m, $\phi \approx 138°$, Fig. 6.7(a)) and 111506 (R $\approx$ 1.79 m, $\phi \approx 107°$, Fig. 6.7(b)), we have on-axis measurements for near parallel and near perpendicular directions, respectively. We find an excellent quantitative agreement between the measurements and the simulations for the scattering volumes located approximately at the plasma center (Fig. 6.2). These discharges have different heating scenarios, different plasma parameters and different projection angles. This fact allows us to posit that in these two discharges where the measurements were performed at the plasma center of TEXTOR, the fast ion distribution function can be described solely by collisions.

On the other hand, for the off-axis scenarios (Fig. 6.7(c), Fig. 6.7(d)) we find

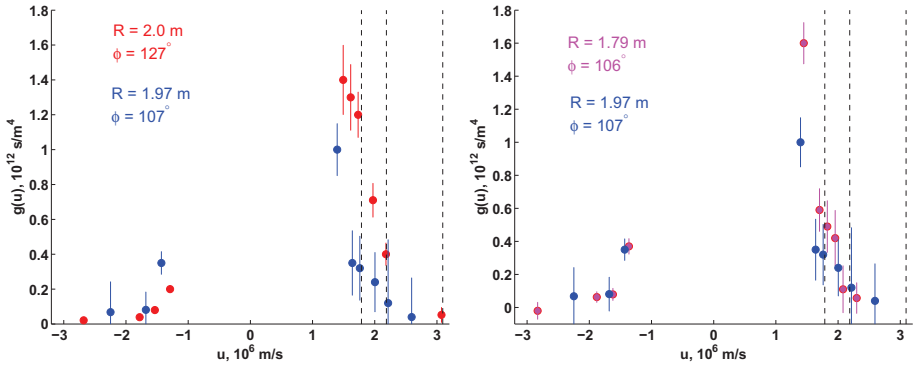

(a) (b)

Figure 6.6: (a) Comparison between the two measurements with off-axis locations but different projection angles: shots 111509, red (R ≈ 1.97 m, ϕ ≈ 127°) and 111512, blue (R ≈ 2.0 m, ϕ ≈ 106°); black dashed lines denote the beam energy fractions E, E/2 and E/3. In shot 111509 the error bars for negative velocities are hidden by markers; (b) Comparison between the two measurements with different locations but similar projection angles: shots 111506, magenta (R ≈ 1.79 m, ϕ ≈ 107°) and 111512, blue (R ≈ 2.0 m, ϕ ≈ 106°); black dashed lines denote the beam energy fractions E, E/2 and E/3.

a discrepancy between the measured and the simulated projections of the fast ion velocity distribution function. The measurement shows a larger population of fast ions at the off-axis location compared with the simulations, an effect which appears for $\phi \approx 106°$ as well as for $\phi \approx 130°$. Part of this discrepancy could be explained by the uncertainty of the radial position of the scattering volume which could arise from a potential probe mirror misalignment. This mirror has two degrees of freedom: it can turn both around the vertical (described by rotation angle) and the horizontal (described by elevation angle) axis, see chapter 3 for details. Due to the fact that the receiver mirror is situated above the probe mirror, an overlap scan can mainly verify the rotation angle alignment. The elevation angle is primarily responsible for the radial position of the scattering volume. Therefore, uncertainty in the probe mirror elevation angle will translate into uncertainty in the radial location of the scattering volume. Consistency checks of other discharges showed that the discrepancy cannot, however, be entirely explained by the probe misalignment. Additionally, an uncertainty in simulations associated with the uncertain shape of the electron temperature and density profiles which were assumed to be identical is possible (see Section 6.2). In order to

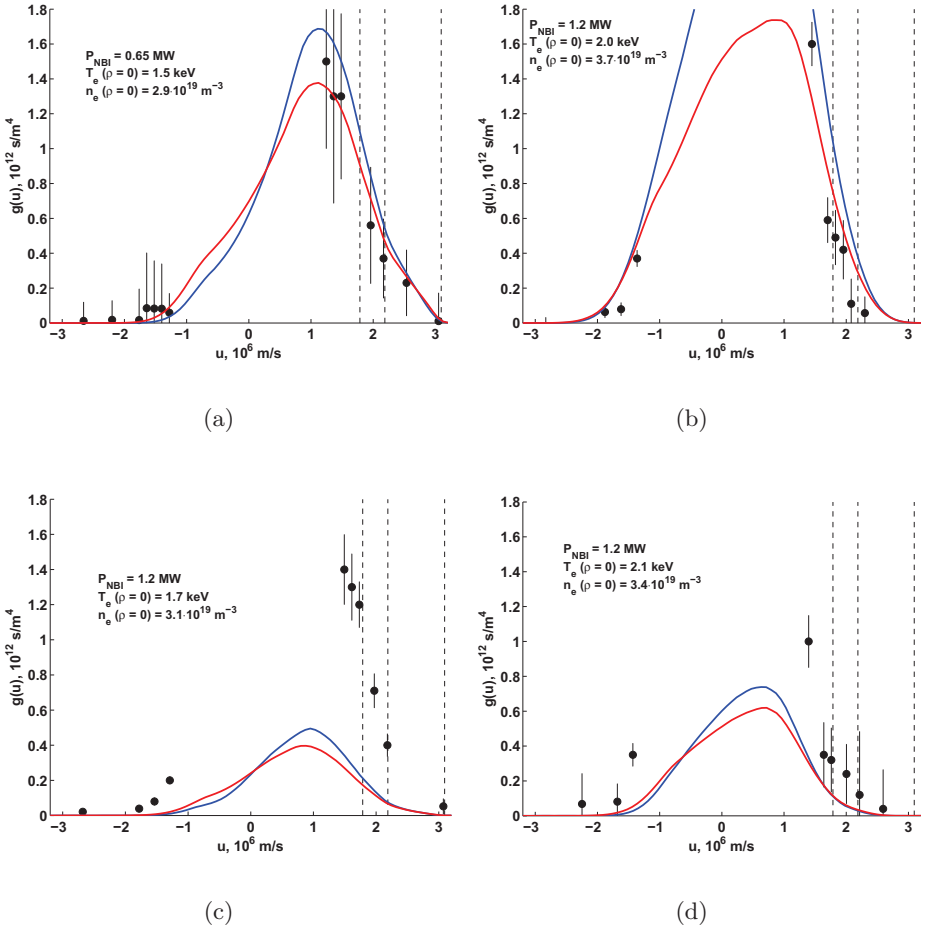

Figure 6.7: 1D projections of the experimental and simulated fast ions velocity distribution functions onto the $\mathbf{k}^{\delta}$ direction at different radial positions. The black dots with error bars (one standard deviation) correspond to the experimental distribution function; the solid red and blue lines correspond to corresponding simulations with ASCOT and VENUS, respectively; black dashed lines show the velocities corresponding to E, E/2 and E/3 beam energy fractions. (a) Discharge 111822, $\phi \approx 138°$, R $\approx$ 1.84 m; (b) Discharge 111506, $\phi \approx 107°$, R $\approx$ 1.79 m; (c) Discharge 111509, $\phi \approx 127°$, R $\approx$ 2.0 m. The error bars for negative velocities are hidden by markers; (d) Discharge 111512, $\phi \approx 106°$, R $\approx$ 1.97 m.

check this hypothesis, a sensitivity study was performed with ASCOT. The electron temperature and density were varied within the prior uncertainties in order to obtain a possible minimum and a possible maximum collisionality. Then the sensitivity of the computed results to the collisionality can be as-

sessed. For discharge 111512 ($\phi \approx 106°$, R $\approx$ 1.97 m) the experimental error bars lie inside the confidence region of the simulations (Fig. 6.8(b)). Hence the uncertain electron temperature and density profiles might explain the discrepancy in this discharge. However, it does not exclude other explanations. For the more parallel geometry in discharge 111509, the experimental error bars are outside the confidence region of the simulations. Here the uncertain density and temperature profiles cannot explain the disagreement (Fig. 6.8(a)). The fact that the fast ion profile seems to be more peaked in the simulations compared with the measurements may also in part be due to additional transport of fast ions in these discharges not accounted for in the modelling. As it was mentioned in Section 6.2, we did not detect any low frequency MHD activity except for sawteeth, neither by Mirnov coils nor by SXR. However, for example core-localized Alfvén eigenmodes (AE), which appear at high frequency and generally do not leave traces on Mirnov coils, could have been triggered. In order for them to be excited, the condition $v_{||} \gtrsim v_A/3$ should be fulfilled, where v_A is Alfvén velocity. For the experimental conditions described in this chapter, the Alfvén velocity is about 10^7 m/s, so the AE can be excited. For discharges 111506 and 111512 (on- and off-axis, perpendicular), the CTS diagnostic is less sensitive to the fast ions moving parallel to the magnetic field which are resonant with the AE. In order to illustrate which fast ions of which regions of the phase space elicit a response onto the same u for experiments with different projection angles $\phi = 106°$ and $\phi = 138°$, weight functions (see Section 2.4) are calculated and their product with the distribution function (discharge 111509) is presented in energy-pitch coordinates in Fig. 6.9. The figure proves that the closer the projection angle is to 90°, the more sensitive the projection of the fast ions distribution function is to trapped particles and the less sensitive to passing ions. For discharge 111822 (on-axis, more parallel), the NBI power might have been too low to excite the Alfvén activity whereas the excitation threshold might have been exceeded in discharge 111509 (off-axis, $\phi = 138°$) with full power NBI. No diagnostics were available to confirm or disprove this hypothesis. Sawtooth activity cannot explain the discrepancy. If sawteeth would have influenced the measurements, it would have primarily affected fast ions located inside the sawtooth inversion radius (discharges 111822 and 111506) which agree well with the simulations.

6.6 Conclusions

In order to compare fast ion velocity distribution functions measured by the CTS diagnostic with the simulations, we performed four discharges where the scattering volumes were twice located in the plasma center and twice off-axis on the low field side with two different values of the projection angle to the magnetic field. The discharges with off-axis scattering volumes had

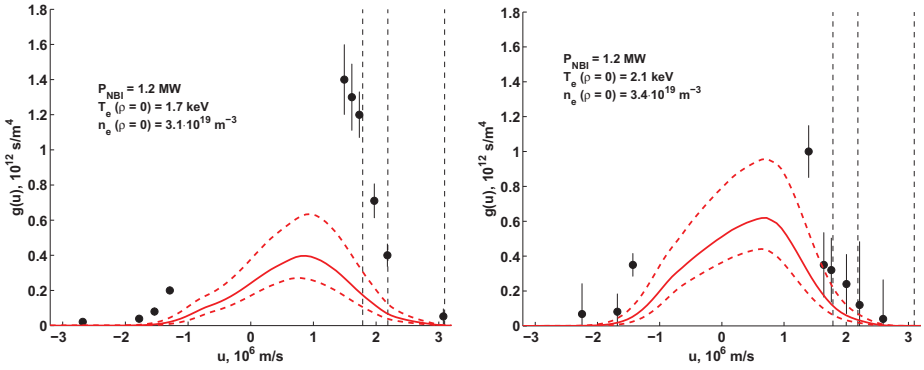

(a) (b)

Figure 6.8: Sensitivity study performed with ASCOT for discharges 111509 ($\phi \approx 127°$, R $\approx$ 2 m) (a) and 111512 ($\phi \approx 106°$, R $\approx$ 1.97 m) (b) for the minimum and maximum possible collisionality obtained from prior uncertainties in electron temperature and density. The black dots with error bars (one standard deviation) correspond to the CTS measurements, solid red lines denote simulation results, dashed red lines show simulation at minimum and maximum possible collisionality.

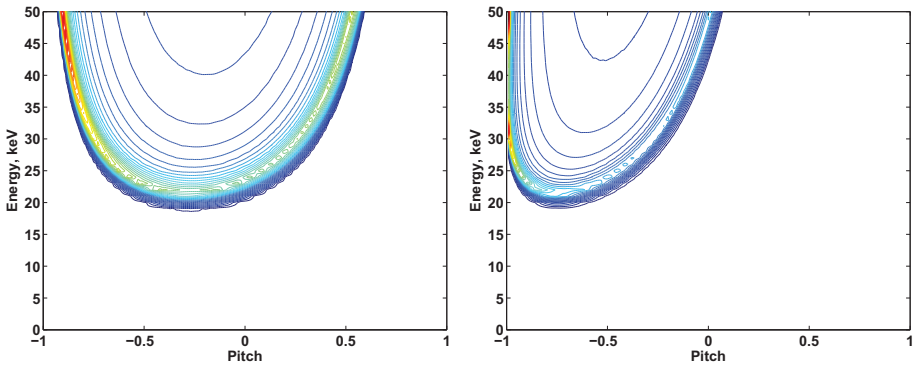

(a) (b)

Figure 6.9: A product of the simulated distribution function (discharge 111509) with the weight functions in energy-pitch coordinates for u = $2{\cdot}10^6$ m/s and (a) $\phi = 106°$; (b) $\phi = 138°$. See Section 2.4 for details.

similar plasma parameters, so the experimentally measured projections of the fast ion velocity distribution function could be compared directly. The projection of the velocity distribution function taken in the direction more parallel to the magnetic field demonstrated larger asymmetry. This result is in a good agreement with our expectations due to the highly tangential geometry of the NBI.

For projection angles close to perpendicular with respect to the magnetic field, the one-dimensional fast ion velocity distribution $g(u)$ for the off-axis location is indistinguishable, within the error bars, from that for the on-axis location for velocities larger than $1.8{\cdot}10^6$ m/s.

The fast ion velocity distribution functions for the discharges were simulated by the guiding center Monte Carlo codes ASCOT and VENUS. The comparison of the measured projections of the fast ion velocity distribution functions with the simulations shows similar trends for both radial locations and each projection angle to the magnetic field. In the plasma center good quantitative agreement between the measurements and the simulations is observed. For the scattering volumes located off-axis, the measured fast ion distribution functions are much larger than the simulated ones throughout all velocities. The discrepancy may in part be due to the uncertainty in the position of the overlap volume, but it cannot be the only reason. A possible source of the discrepancy can be an assumption of the identical shape of the electron temperature and density profiles to those measured instantaneously by incoherent Thomson scattering. Another cause of the discrepancy can be an additional fast ion transport which could take place in these discharges and transport fast ions from the center to the periphery. One of the probable mechanisms of fast ion transport is through interaction with AE. However, presence or absence of Alfvén activity in any of the discharges discussed in this chapter cannot be confirmed by other diagnostics. This mechanism is not taken into account in the simulations.
The comparison between measurements and simulations will benefit if the measurements are taken simultaneously at different locations in the discharge, then the gradients in fast ion phase space density can be studied. Simultaneous CTS measurements at the same spatial location with different projection angles will allow a reconstruction of 2D fast ion velocity distribution functions [68]. This can be obtained in future when the second CTS receiver is installed on ASDEX Upgrade.

Chapter 7

Influence of Resonant Magnetic Perturbations on Fast Ion Confinement

Edge localized modes (ELMs) are a big challenge for the coming ITER machine. Several methods have been developed for mitigating ELMs like pellet pace making or resonant magnetic perturbations (RMP). In this chapter we discuss influence of the RMP applied to the plasma edge on fast ion confinement in the core. It was shown in [118] that individual ELMs can decrease plasma energy by 5 - 10% and are also responsible for extreme heat loads on divertor tiles and the first wall. ELMs occur when the steepness of the pressure profile at the edge exceeds a certain critical value. Present methods of ELM control are either triggering them frequently by pellet injection making each individual event acceptably weak, or keeping the edge pressure gradient below the threshold. In the low-confinement regime (L-mode) gradients are shallow and ELMs have never been observed. However, the transport in L-mode is high and it will be difficult to meet the Lawson criteria. In the high-confinement regime (H-mode) a special method has to be applied in order to stay below the critical value of the pressure gradient. Experiments [119–121] showed that by applying weak radial perturbations of the magnetic field (in order of 1% of the equilibrium value) to the magnetic surfaces with $q = 3$ or $q = 4$, the plasma pressure gradient decreases at the edge sufficiently to achieve a complete ELM mitigation. However, the particle and heat transport are low compare to the L-mode regime. It was shown in [119] that RMP mainly affects the density while the pedestal electron temperature remains the same and even shows a tendency to grow. At the same time, questions about fast ion transport at various energies and pitch angles remain open. In order to shed light on this, experiments were performed on the TEXTOR tokamak which is equipped with a dynamic ergodic divertor (DED), a set of external coils located at the high

field side of the machine which create RMP by specially set currents [122]. Simulations demonstrate that RMP influence fast ion confinement due to symmetry breaking of the magnetic field [123]. Prompt losses of fast ions due to an ergodic structure of the magnetic field at the plasma edge may be triggered. This can be a significant issue for example with ICRF heating where fast ions are accelerated to MeV energies primarily in the direction perpendicular to the magnetic field and have a large banana width. RMP may also influence passing fast ions due to various harmonics of the perturbation field which can penetrate deep inside plasma and modify magnetic field structure in the plasma center. For example, it is known that on TEXTOR DED can trigger $(m, n) = (2, 1)$ magnetic islands. By means of CTS we sought to investigate the confinement of fast ions at the plasma center in the TEXTOR tokamak in the presence of RMP.
RMP influence the shape of the plasma density and temperature profiles, thus changing the NBI ionization profile. The profile effects need to be decoupled from the influence of the changed magnetic structure on the fast ion confinement. In order to comply with this, the slowing down of fast ions is studied by means of the CTS diagnostic. Notches are placed in the NBI power and the fast ion content in the overlap volume is studied after NBI has been switched off. Unfortunately, due to lack of time and computational complications, the evolution of the 1D fast ion distribution function has not been studied, here only SPD results are presented. The results on inferred fast ion velocity distribution will be presented in later publications.

7.1 Experimental Results

DED in the TEXTOR tokamak works at two main configurations: $(m, n) = (3, 1)$ and $(m, n) = (6, 2)$. The CTS measurements were conducted for both configurations of DED in the DC mode. Key experimental parameters for the $(m, n) = (3, 1)$ campaign are listed in Table 7.1, the experimental parameters from the experiments with the $(m, n) = (6, 2)$ DED configuration are presented in Table 7.2.

For the $(m, n) = (3, 1)$ configuration experiments a low value of current in the error field coils was chosen in order to stay below the tearing mode threshold. That is due to a strong $(m, n) = (2, 1)$ side band of the DED [124]. The tearing mode threshold strongly depends on toroidal plasma rotation [124], therefore using counter-I_p NBI reduces a risk of the tearing mode generation. As it is shown in Fig. 3.11 and explained in Section 3.3, the TEXTOR tokamak has two identical NBIs, launching in the opposite toroidal directions. The charge exchange diagnostic on TEXTOR works only with NBI 1 which launches the beam in a co-I_p direction in standard shots. In order to have the charge exchange diagnostic available in presence

Parameters	Value
Radial position of the scattering volume, m	≈ 1.8
Resolved angle, $\phi = \angle(\mathbf{B}, \mathbf{k}^{\delta})$	$\approx 135^{\circ}$
B_T @ magnetic axis [T]	2.6
I_P [kA]	340
n_e @ $\rho = 0$ [10^{19} m^{-3}]	3.3 - 4
T_e @ $\rho = 0$ [keV]	2.0 - 2.6
T_i @ $\rho = 0$ [keV]	2.9 - 3.3
DED current [kA]	1.1 - 3.1
DED configuration, (m, n)	(3, 1)
DED operation mode	DC
Co-I_P NBI power (NBI 2) [MW]	1.2
Ctr-I_P NBI power (NBI 1) [MW]	0.5 - 0.7
Beam ions	Hydrogen
NBI energy [keV]	50

Table 7.1: Key experimental parameters during the first RMP campaign

Plasma parameters	111823	111824	111826
Radial position of the scattering volume, m	1.78		
Resolved angle, $\phi = \angle(\mathbf{k}^{\delta}, \mathbf{B})$	141°		
B_T @ magnetic axis, T	2.61		
I_P, kA	430		
n_e @ $\rho = 0.1$, 10^{19} m^{-3}	3.2 - 2.9	3.5 - 2.7	4.5 - 4.2
T_e @ $\rho = 0.1$, keV	1.5 - 1.2	1.6 - 1.1	1.7 - 1.2
Co-I_P NBI power, MW	1.2		
Beam ions	Hydrogen		
NBI injection energy, keV	50		
DED current, kA	0	0	4.3

Table 7.2: Plasma and CTS system parameters during the RMP experiments. TEXTOR discharges 111823, 111824 and 111826.

of counter-I_p NBI, we chose an inverse configuration of I_p and B_t. However, counter-I_p NBI causes a spiky signal in some of the channels of the CTS receiver which complicates the analysis of the fast ion results, see chapter 8. For this reason, the experiments are conducted in the $(m, n) = (3, 1)$ DED configuration with the counter-I_p NBI power of 30 - 50% of its maximum. In the measurements, the projection angle to the magnetic field was $\phi \approx 135^{\circ}$. Measurements are done at the plasma center, see Fig. 7.1(a). As it is mentioned above, the influence of RMP on fast ion confinement is investigated by studying the slowing down of fast ions when the source has been switched off. Fig. 7.1(b) illustrates the shot plan for the experiments with

DED in the $(m, n) = (3, 1)$ configuration. The counter-I_p NBI is launched during an entire discharge with 30 - 50% of its maximum power. In order to make steady-state conditions, the co-I_p NBI is switched on 100 ms prior to the CTS measurements. Half way through the CTS measurement phase, the co-I_p injection is switched off. The CTS measurements last for 200 ms. Unfortunately, the goals of these experiments could not be fulfilled. Firstly, we could not prevent the formation of magnetic islands during the DED operation: practically in all discharges an $(m, n) = (2, 1)$ locked mode was present. Secondly, the CTS data were contaminated with the secondary emission signal (see Section 4.5). As it was mentioned above, presence of the secondary emission signal makes proper CTS data analysis practically impossible.

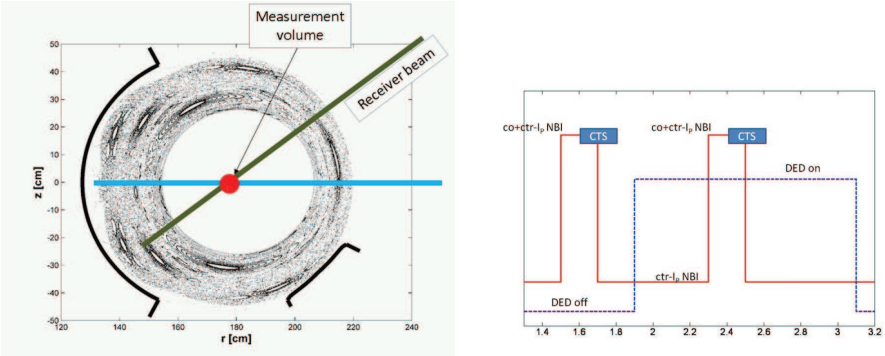

(a) (b)

Figure 7.1: (a) Scattering geometry of the CTS experiments with the $(m, n) = (3, 1)$ DED configuration. Measurements were taken at the center at R $\approx$ 1.8 m; The ergodic field structure in vacuum for the $(m, n) = (3, 1)$ DED configuration is shown, the Poincaré plot is provided by O. Schmitz; (b) Experimental plan for the measurements with DED working in the $(m, n) = (3, 1)$ configuration.

The experiments which are discussed in this chapter were conducted at different experimental campaigns at TEXTOR. Another configuration of the DED, $(m, n) = (6, 2)$ was explored. In between the campaigns the DED coil arrangement was changed. The discharges are made with the standard direction of I_p and B_t. It is known that the DED discharges in TEXTOR requires a counter-I_p NBI to avoid the tearing mode triggering. However, due to the problems which the counter-I_p beam causes for the CTS data interpretation (see Chapter 8), the counter-I_p NBI is not used any longer.

Instead the DED current is significantly reduced.
The measurements are made in the plasma centre with $\phi \approx 141°$. The CTS measurements are conducted in three phases: without DED, at DED flat top operation and after the DED current has been modified. Unfortunately, the CTS experiments faced the problems similar to those in the experiments with the $(m, n) = (3, 1)$ DED configuration. The secondary emission signal remained an issue for the CTS experiments with the $(m, n) = (6, 2)$ DED configuration, and magnetic islands due to the DED operation also appeared in the discharges. However, there were sufficient amount of uncorrupted data for the analysis. In Fig. 7.2 one can see that in discharge 111824, the locked $(m, n) = (2, 1)$ mode appears after the second NBI notch, and it is clearly visible on the rotation velocity graph. These two discharges also illustrate an enhanced particle confinement due to the DED operation. It results in increase of the plasma density during the RMP phase. The enhanced confinement phase is observed at small DED currents and is changed by increased particle and heat transport when the RMP amplitude is increased. The experimental observations of the phenomena are reported in [125] where the enhanced confinement was detected with DED current of around 4.5 kA. The result presented in this chapter is expected [126], even though it has not been observed for the DED currents as low as 1 kA. According to the reference 126, the density gradient change (either positive or negative) is determined by the error field amplitude and the velocity of toroidal rotation at the resonance magnetic surface.
Despite of all the difficulties, the data obtained during the campaign are interesting. Three CTS measurement periods are compared; classical (no DED), DED without an island, without DED with a decaying rotating island. There was no secondary emission in all three measurement periods. Each of these periods is taken from three discharges with similar parameters. One period from discharge 111823 is taken in the absence of RMP and is used as a reference. The second measurement period is taken from discharge 111826 without an island in the 'pump-in' regime, i.e. where the DED operation makes the density gradient steeper. The third measurement period is taken in the absence of RMP and with the decaying rotating magnetic island, discharge 111824. In the Fig. 7.2 the magnetic spectrogram of the discharge 111824 (the spectrogram of the discharge 111826 is clean), co-I_p NBI power (MW) and the DED current (kA), toroidal rotation velocity and electron density in the plasma center are shown as functions of time.

The time traces of the CTS spectra at frequency $f = 110.873$ MHz was analysed. That is approximately 870 MHz away from the gyrotron line and on the 1D projection of the fast ion velocity distribution function corresponds to the velocity node of $u = 2.3 \cdot 10^6$ m/s. The weight function for this velocity and projection angle of 141° peaks for passing particles. Fig. 7.3 shows that there is almost no difference between the scenarios with

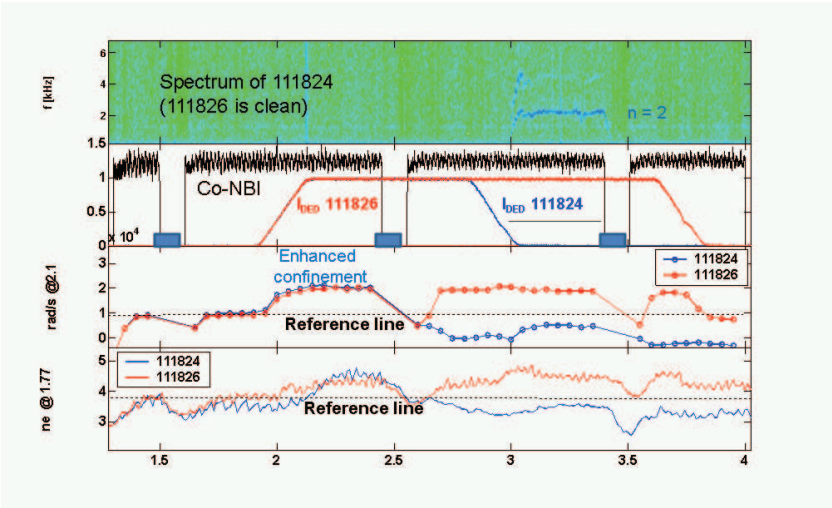

Figure 7.2: Time traces and the spectrogram of TEXTOR discharges 111824 and 111826. From top to bottom: spectrogram of discharge 111824 from the magnetics pickup coils(the spectrogram from 111826 had no modes); co-I_P NBI power, MW, and the DED current, kA; rotation angular velocity; electron density from the interferomter channel at R = 1.77 m.

and without magnetic islands. The DED scenario shows around 30% smaller decay time than in the discharges without DED. The similarity in the the

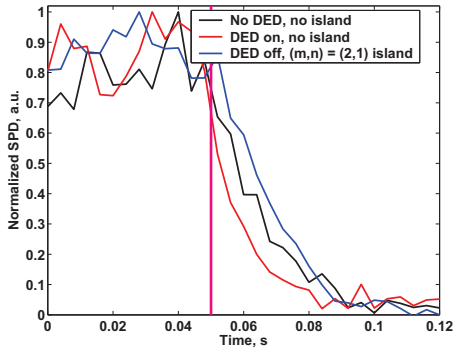

Figure 7.3: The comparison of the normalized time traces for three different scenarios: without RMP and magnetic island (black line, discharge 111823), with RMP and without magnetic island (red line, discharge 111826), without RMP in presence of decaying magnetic island (blue line, discharge 111824). The vertical line denotes a moment when NBI is switched off.

.

time traces can be explained assuming that the orbits of fast ions which are probed by the CTS diagnostic do not cross the island. However, it seems

to contradict the observation of the enhanced noise level which decreases with the decaying tearing mode, see Fig. 7.5(a). It is worth mentioning that strong fluctuations of the signal level in the CTS channels are observed only during gyrotron on periods, the level of ECE background fluctuations in some central channels is six time smaller than the fluctuation level at gyrotron on periods.
The slowing down curves of the CTS time traces for the reference scenario, scenario with DED, and the scenario without DED with the decaying island are fitted with exponential function: $S \propto exp(-\nu \cdot t)$, where S is the signal in the CTS fast ion channel, ν is the fitting coefficient. The results are the following:

- $\nu_{reference} = 59.3 \pm 4.4\ \frac{1}{s}$, discharge 111823
- $\nu_{island} = 59.6 \pm 3.9\ \frac{1}{s}$, discharge 111824
- $\nu_{DED} = 79.6 \pm 3.7\ \frac{1}{s}$, discharge 111826

Here the results are given with 68% confidence interval. Assuming that the decay of fast ion signal is due to collisions ($\nu \propto n$), the ratio between fitting coefficients in different scenarios should be equal to the ratio of central densities in the corresponding measurement periods:

- $\nu_{reference}/\nu_{DED} = 0.745$, $n_{reference}/n_{DED} = 0.7 \pm 0.02(1\sigma)$
- $\nu_{island}/\nu_{DED} = 0.749$, $n_{island}/n_{DED} = 0.75 \pm 0.05(1\sigma)$

The electron density data in the overlap volume are obtained from interferometry. Electron temperature in all three shots is approximately equal according to the ECE diagnostic, therefore it is not considered to cause any effect. One can clearly see that the observed discrepancy in the slowing down time traces is explained by different densities. No additional transport due to the DED operation is evident.

The direct comparison between the CTS measurements in the reference shot and in the discharge with the decaying tearing mode is shown in Fig. 7.4. One can clearly see that these two normalized spectra taken during the NBI-on time are clearly asymmetric and are indistinguishable within the error bars in most of the points. However, one can clearly see that the signal from the discharge with the decaying island (111824) is significantly noisier than the reference discharge. The noise is asymmetric and is greater in the channels which correspond to the co-I_p fast ions with significant perpendicular velocity. No structures in the CTS signal similar to those described in reference 95 and in Section 5.1 are found. The noise level in the CTS signal in discharge 111824 decays after the NBI has been switched off, see Fig. 7.5.

The noise level stabilizes after approximately 30 ms of the NBI switch off time. The same time is also needed for the magnetic island to decay.

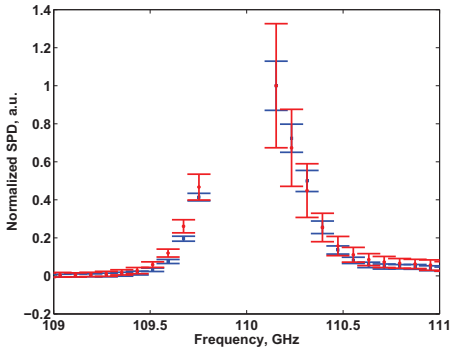

Figure 7.4: The comparison of the normalized SPD during the NBI on time for discharges 111823 (no RMP, no island) - blue squares and 111824 (no RMP, (m, n) = (2, 1) island) - red. Error bars stand for one standard deviation of the scattered light during one gyrotron-on period

.

In discharge 111824 (no DED, decaying rotating island) the CTS channels at frequencies in the vicinity of 110 GHz show a strong increase, see Fig. 7.6(a). The signal in these channels is strongly affected by bulk plasma parameters, primarily ion temperature, and show a significant increase, in some channels up to 40%. Typically, SPD of scattering signal decreases in all the channels after NBI has been turned off, see SPD of the reference measurement period in Fig. 7.6(b). The observation could be caused by reduction of heat transport from the plasma centre. However, when the NBI 1 is switched off, no ion temperature measurements are conducted. Electron temperature measurements decrease monotonically. The observation cannot be explained by the density effect either because the density in the plasma centre monotonically decreases after the NBI has been switched off.

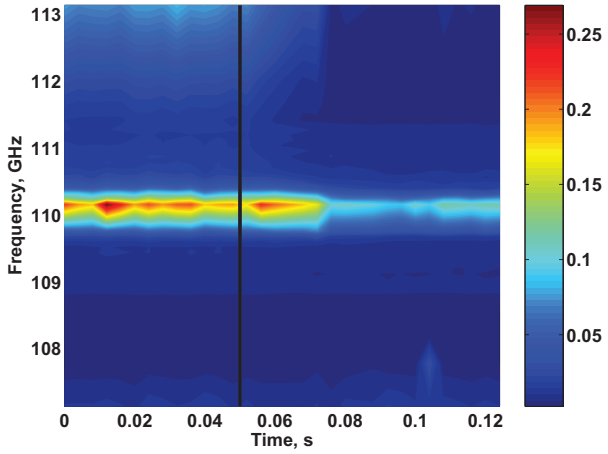

(a)

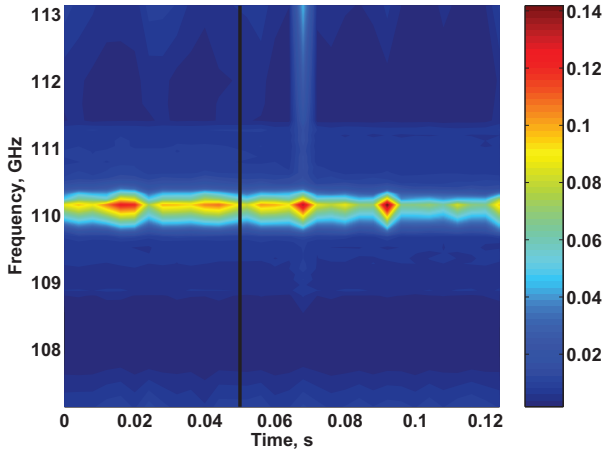

(b)

Figure 7.5: Contour plot showing evolution in time of normalized uncertainties in the CTS spectra (one standard deviation) in TEXTOR discharge 111824, with the decaying island and without DED (a); in TEXTOR discharge 111823, reference shot (b). Black vertical line marks the moment of NBI switch off. The uncertainties are normalized to the maximum value of SPD in the measurements.

7.2 Conclusions

The experiments on investigation of influence of resonant magnetic perturbations on fast ion confinement were designed and conducted. In the exper-

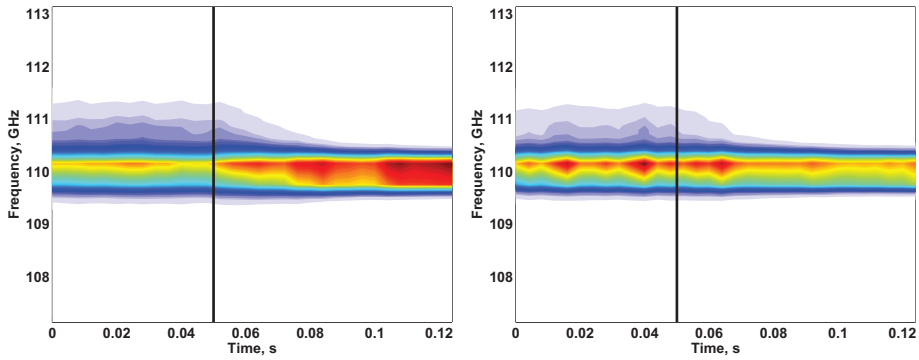

(a) (b)

Figure 7.6: Contour plot of SPD of discharge 111824 with rotating island and no RMP (a) and in the reference discharge 111823 (b). The vertical line denotes a moment when NBI is switched off.

iments with the $(m, n) = (3, 1)$ DED configuration, secondary emission in the CTS data hampered the analysis.
In the CTS experiments with the $(m, n) = (6, 2)$ configuration the shot plan was redesigned. No counter-I_p NBI was used, DED current was around 1 kA in order to avoid tearing mode generation. The regime with an enhanced confinement [125] was re-discovered at smaller RMP amplitude.
The discrepancy in the decay time between discharges with and without RMP could be explained by the density effect in collisional process.
The reference discharge 111823 and the discharge with the decaying magnetic island show similar fast ion slowing down time at the same plasma parameters in the overlap volume. It suggests that the tearing mode either did not cause any additional fast ion transport or that orbits of fast ions which were studied by the CTS in this discharge did not intersect the islands. However, noise level in the discharge 111824 was found significantly higher than that in the reference discharge. The noise in the CTS spectra from discharge 111824 is skewed, it is larger at frequencies above the probing frequency and decays after the NBI has been turned off. It stabilized only when the tearing mode was not present in the plasma any longer.
Growth of the signal level in the central channels of the CTS diagnostic in discharge 111824 was detected after the NBI had been turned off. The growth lasted for 30 ms and afterwards the level saturates. The exact reason for this observation remains unknown. It can only be stated that the observation is associated with decay of the magnetic island.

Chapter 8

Fast Ion Driven Instabilities in the Ion Cyclotron Frequency Range Measured by CTS

In a number of CTS experiments on TEXTOR where counter-I_P NBI or the low-power transverse diagnostic beam are used, an instability is detected. It resulted in a significant increase of the radiation detected by the receiver in two-four channels which form a series of peaks in the spectrum; the peaks are symmetrical with respect to the gyrotron frequency. Detailed investigation of this phenomenon is conducted using the CTS receiver upgraded with a high bandwidth oscilloscope which provided the spectral resolution of the acquired data better than 1 MHz and reveals a fine structure of the signal detected previously by the fast ion CTS receiver. Multiple peaks at the observed frequencies could be interpreted as instability at harmonics of hydrogen cyclotron frequency.

8.1 Literature Overview of Previous Results and Theoretical Models

Instability signals at frequencies corresponding to the harmonics of the ion cyclotron frequency were detected in different machines, i.e. TFTR [127–129], JET [130–132], JT-60U [133] and Wendelstein 7-AS [134, 135]. In TFTR the emission was triggered by fusion products in the supershots (shots during the D - T campaign), as well as by NBI. The frequencies of the signal corresponded to the location at outer midplane of the tokamak. In JET plasmas the ion-cyclotron emission (ICE) was driven by fusion-born α-particles. The ICE in JT-60U was triggered by high-energy deuterium ions

originating from the NBI, fusion-born tritium, and ^{3}He ions. In the Wendelstein 7-AS stellarator the emission was triggered by a low-power radial diagnostic hydrogen beam. In references 136–139 the theoretical explanations of the observed phenomena in the tokamaks are given. For both cases of super-Alfvénic fusion products and sub-Alfvénic NBI-born fast ions, the emission was caused by a magnetoacoustic cyclotron instability. However, the instability acts differently in the presence of super- or sub-Alfvénic fast ions. As it is shown in references 128, 140, 141, the ICE observed in TFTR which was triggered by super-Alfvénic fusion-born α-particles had an analytical explanation which agreed qualitatively with the experiments. For the analytical model, the fast ion distribution function was assumed to have the following form:

$$f_\alpha \propto e^{-\frac{(v_{||}-v_d)^2}{v_r^2}} \delta(v_\perp - u) \tag{8.1}$$

In electrostatic limit and in case of small concentration of fast ions ($n_\alpha \ll n_i$) and neglecting Landau damping, in zero-order approximation the dispersion relation is the following:

$$\omega^2 = \frac{1}{2} c_A^2 \left[k^2 + k_{||}^2 + k^2 k_{||}^2 \frac{c_A^2}{\Omega_i^2} + \sqrt{\left(k^2 + k_{||}^2 + k^2 k_{||}^2 \frac{c_A^2}{\Omega_i^2} \right)^2 - 4 k^2 k_{||}^2} \right] \tag{8.2}$$

The first-order correction to this equation gives a growth rate:

$$\begin{aligned} \gamma^2 &= \frac{\omega_{p\alpha}^2}{\omega_{pi}^2} \left[M_n \frac{n\Omega_\alpha}{k_{||} v_r} - \frac{2u^2}{v_r^2} \eta_n N_n \right] \cdot \\ &\quad \cdot \frac{\Omega_i^4}{(\Omega_i + (\omega - \Omega_i) N_{||}^2)(\Omega_i - (\omega + \Omega_i) N_{||}^2)} \frac{\sqrt{\pi}}{2\omega} e^{-\eta_n^2} \end{aligned} \tag{8.3}$$

$$\begin{aligned} M_n &= 2n \frac{\omega}{\Omega_i} \left[J_n'(z_\alpha) - \frac{(n^2 - z_\alpha^2) J_n^2(z_\alpha)}{z_\alpha^2} \right] - \\ &\quad -2 \frac{\omega^2 - \Omega_i^2}{\Omega_i^2} \frac{J_n(z_\alpha) J_n'(z_\alpha)}{z_\alpha} \left[n^2 N_\perp^2 - (z_\alpha - 2n^2) N_{||}^2 \right] + \\ &\quad +2 \frac{J_n(z_\alpha) J_n'(z_\alpha)}{z_\alpha} (z_\alpha^2 - 2n^2) \end{aligned} \tag{8.4}$$

$$\begin{aligned} N_n &= -2n \frac{\omega}{\Omega_i} \frac{J_n(z_\alpha) J_n'(z_\alpha)}{z_\alpha} + \\ &\quad + \frac{\omega^2 - \Omega_i^2}{\Omega_i^2} \left[N_{||}^2 \left(\frac{n^2 J_n^2(z_\alpha)}{z_\alpha^2} + J_n'^2(z_\alpha) \right) + N_\perp \frac{n^2 J_n^2(z_\alpha)}{z_\alpha^2} \right] + \\ &\quad + \frac{n^2 J_n^2(z_\alpha)}{z_\alpha^2} + J_n'^2(z_\alpha) \end{aligned} \tag{8.5}$$

Here $N_{||} = k_{||} c_A/\omega$, $N_\perp = k_\perp c_A/\omega$, $\eta_n = (\omega - k_{||} v_d - n\Omega_d)/k_{||} v_r$, J_n is the Bessel function of n-th order, $z_\alpha = k_\perp u \Omega_\alpha$, $n = round(\omega/\Omega_\alpha)$. It was

shown in reference 141 that the growth rate depends on a number of dimensionless parameters, i.e. ratio of α-particles to the background ion density ($\xi = n_\alpha/n_i$), the wave propagation angle ($\tan(\Theta_k) = k_{||}/k_\perp$), narrowness of the fast ion distribution function ($\sigma = v_r/u$) and the ratio of the α-particle velocity to the Alfvén velocity ($\zeta = v_{\alpha 0}/c_A$). It was shown that the distribution function of super-Alfvénic fast ions does not need to be very narrow. For sub-Alfvénic alphas the distribution function has to be several times narrower in order to destabilize the same harmonic as for super-Alfvénic alphas. Surprisingly, the increased concentration of fast ions does not increase the growth rate since it leads to a wider distribution function which stabilizes the instability. This fact is in a good qualitative agreement with the supershot experiments in TFTR where the ICE associated with fusion products vanished in less than 200 ms [128].

In references 134,135 the instabilities driven by the transversal low-power diagnostic hydrogen beam and heating radial NBI in the Wendelstein 7-AS stellarator are described. The unlocalized measurements were made by the CTS diagnostic [85] and a broadband loop antenna. The instability induced by the low-power diagnostic beam due to its density dependence was identified as of lower-hybrid (LH) type under double-resonance condition (when the LH frequency coincides with one of the harmonics of the ion cyclotron frequency) [135]. In reference 134 it was shown that the radial NBI in Wendelstein 7-AS also triggers LH instability. The diagnostic beam launches fast particles with a pitch angle of 90° to the magnetic field so that almost all ions after the ionization become trapped in the magnetic ripple of the stellarator. These ions are not confined due to ∇B drift in the inhomogeneous magnetic field. The instability happens most likely in the plasma center since the change of direction of the magnetic field makes the signal level much smaller. This is due to the fact that in reverse configuration most of fast ions originating from the diagnostic injector do not drift through the center of the plasma before they are lost. The radial heating NBI launches particles with a pitch angle of about 60° and most of the fast ions originating from this injector are passing particles, so a substantially greater amount of fast ions is needed in order to destabilize the LH waves. Moreover, it was shown that passing fast ions have a stabilizing effect. The stability analysis presented in reference 134 specified operating regimes when the radial NBI causes constant LH activity or transient LH activity (only shortly after the beam has been switched on) or does not cause any LH instability at all. The multiple-harmonics structure resolved with the broadband loop antenna in Wendelstein 7-AS shows no sensitivity to the low-power diagnostic beam [134]. This is explained by the excitation of the ion Bernstein instability for steady-state distributions of fast ions.
The dispersion relation for the LH waves under the double resonance con-

dition was obtained:

$$D_0(w) = H_n \frac{\omega_{ci}}{\omega - n\omega_{ci}} \tag{8.6}$$

$$H_n = -\frac{2n\omega_{pi}^2}{k^2} \int J_n^2\left(\frac{k_\perp v_\perp}{\omega_{ci}}\right) \frac{\partial f_i}{\partial v_\perp^2} d^3v \tag{8.7}$$

In the first order approximation, assuming $D_0(\omega) = D_0'(\omega_{LH}) \cdot (\omega - \omega_{LH})$, the frequency and the growth rate of the LH instability were calculated in reference 134:

$$\omega = \omega_{LH} - \frac{\omega_{LH} - n\omega_{ci}}{2} \pm \sqrt{\left[\frac{\omega_{LH} - n\omega_{ci}}{2}\right]^2 - \gamma_n^2} \tag{8.8}$$

$$\gamma_n = \omega_{ce}\omega_{LH} \sqrt{-\frac{H_n}{2n(\omega_{ce}^2 + \omega_{pe}^2)}} \tag{8.9}$$

8.2 Experimental findings in TEXTOR

The previous results on NBI driven instabilities in the ion cyclotron range were described in Section 8.1. In this section experimental results obtained by the CTS diagnostic in TEXTOR are described.
TEXTOR NBI was introduced in Section 3.3. As well as heating NBI, the tokamak is equipped with the low-power radial hydrogen diagnostic injector RUDI [142]. Instabilities driven by energetic ions have been observed both in the regime of counter-I_p heating with high power and with low-power RUDI operation.
Fast ion driven instabilities have frequencies corresponding to various harmonics of ion cyclotron emission from the plasma. In standard configuration of the CTS receiver the narrowest channel width is 80 MHz which makes a detailed study of the instabilities in the ion cyclotron range impossible. However, the first signs of these instabilities were obtained in the standard configuration of the receiver. It resulted in the unusually high signal in one to two channels on each side of the probing frequency. An example of traces of these instabilities in the CTS signal is shown in Fig. 8.1

8.2.1 Experimental Setup

In order to perform measurements with substantially higher frequency resolution which would allow studying the instability evolution in time the CTS receiver was upgraded. The upgrade is described in Section 3.5.

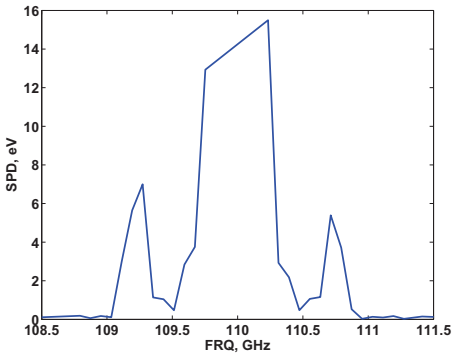

Figure 8.1: Traces of NBI driven instability in the CTS receiver. The instability is triggered by the RUDI beam in the discharge 111802, the graph represents a scattering spectrum at 2.95 s. An enhanced signal at 109.3 and 110.7 GHz is not typical for the normal CTS operation and was caused by the RUDI beam injection.

In all the experiments the gyrotron is modulated with 50% duty cycle, 2 ms on/2 ms off. The discharges are conducted in deuterium-fueled plasma with hydrogen NBI. The injection energy of fast particles is 50 keV, power varies between 600 kW and 1.2 MW for heating NBI and is constant at 50 kW for RUDI. In discharges where heating NBI is used the injection is always balanced, i.e. $P_{co-NBI} = P_{ctr-NBI}$. Density varies from $3{\cdot}10^{19}$ to $5.5{\cdot}10^{19}$ m^{-3}.

8.2.2 Transient Activity

The activity in the range of frequencies corresponding to harmonics of ion cyclotron frequency is observed during the counter-I_p NBI switching-on time. This frequency range is later called the ICE range of frequencies in the sense that the frequency separation between the pikes is similar to the hydrogen or deuterium cyclotron emission frequency originating from the tokamak at present operating conditions. The activity is transient because most of its signatures disappear shortly after the NBI switching-on time. In Fig. 8.2 the spectrogram of discharge 111528 obtained by the upgraded CTS receiver is shown. The first gyrotron-on period in the graph is the first period after the NBI switching-on time. In Fig. 8.3(a) an averaged spectrum over the first gyrotron-on period is shown for shot 111528. Zero frequency corresponds to the frequency of the probing radiation. The frequency range between 0 and 200 MHz is covered by the notch filter. Different spectral lines in this discharge during the transient ICE activity most likely originate from different kinds of instabilities; the spacing between the lines varies from 5 to 42 MHz. However, if several different kinds of instabilities in the same frequency range contribute to the spectral shape, the spacing between the

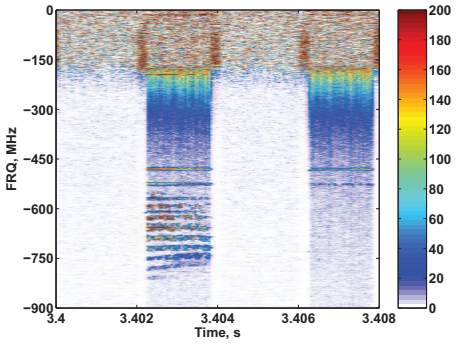

Figure 8.2: Spectrogram of the CTS signal for discharge 111528. counter-I_p NBI switches on at 3.4 s. Signal at frequency range [-150 0] MHz contains no information because it is masked by the notch filter.

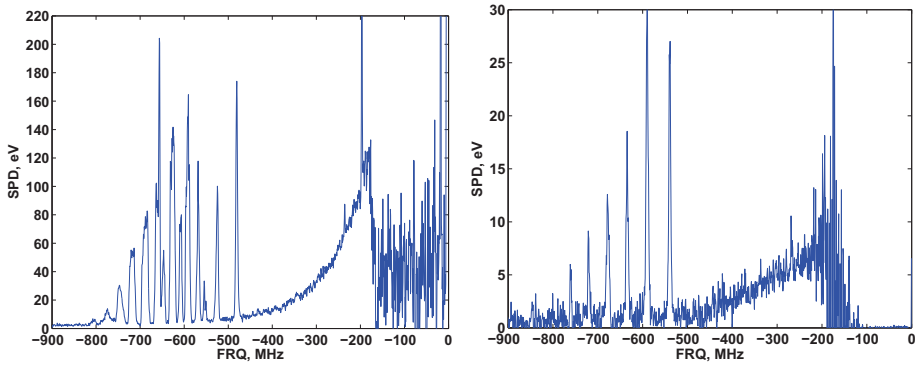

(a) (b)

Figure 8.3: (a) Mean CTS spectrum of the gyrotron pulse closest to the counter-I_p NBI switching-on time in discharge 111528, P_{NBI} = 1.2 MW; (b) Mean CTS spectrum of the gyrotron pulse closest to the counter-I_p NBI switching on time in discharge 111802, P_{NBI} = 0.6 MW. Frequency range [-200 0] MHz is masked by the notch filter.

peaks may provide only very limited information. In this discharge both co- and counter-I_p NBI are working simultaneously at almost maximum possible power, 1.2 MW. At the same time in discharge 111802 (Fig. 8.3(b)) both co-I_p and counter-I_p NBI are working at 600 kW, also discharge 111802 has a density in the plasma centre of $5.5{\cdot}10^{19}$ m^{-3}, which is around 30% higher than in discharge 111528. The central density in discharge 111528, according to interferometer, is around $4.2{\cdot}10^{19}$ m^{-3}. At lower power and higher density discharges the peaks of the ICE are arranged more regularly,

with the distance between peaks increasing from lower frequency to higher monotonically from 39 to 50 MHz. These frequencies correspond to the hydrogen cyclotron frequency at magnetic field in the range 2.6 T - 3.3 T. In these discharges such magnetic field corresponds to the plasma centre and high field side.

8.2.3 Steady-state Emission Triggered by Counter-I_p Heating NBI

Steady-state emission from heating counter-I_p NBI is observed in many discharges. It has a different spectral structure than the transient activity described in the previous section, even though it is also driven by the counter-I_p NBI. An example is shown in Fig. 8.4. In discharge 109172 both co- and counter-I_p NBI are switched on. Co-I_p NBI works at 0.8 MW and counter-I_p NBI at 1.2 MW at low density, less than $3{\cdot}10^{19}$ m^{-3}, according to interferometer. In contrast to the Fig. 8.3(b), the distance between the peaks during the steady-state NBI operation decreases monotonically from lower to higher frequencies (in absolute values) from 52 MHz to 47 MHz (Fig. 8.4). In terms of hydrogen cyclotron frequencies it corresponds to the magnetic field of 3.5 T, i.e. the source would be located at the high field side. In other discharges similar trends are observed.

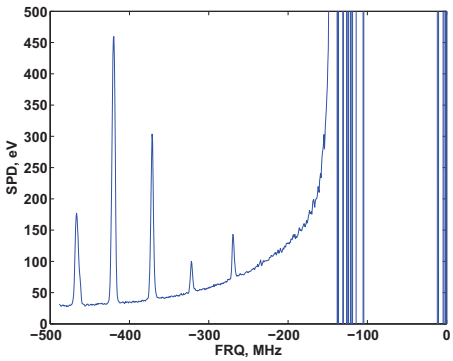

Figure 8.4: Mean CTS spectrum of the steady-state ICE in discharge 109172 at around t = 1.7 s during counter-I_p NBI. Signal in the frequency range [-150 0] MHz is masked by the notch filter and contains no information.

8.2.4 ICE Triggered by Low Power Diagnostic Beam

Low power (50 kW) radial hydrogen diagnostic beam (RUDI) is used to study ICE on TEXTOR. In discharge 111802 RUDI is on during 600 kW co-I_p NBI operation. At this period no ICE-associated activity is detected by CTS. At the moment when co-I_p NBI is switched off, the ICE peaks start to emerge (Fig. 8.5(a)). There is no significant transient activity, i.e. the

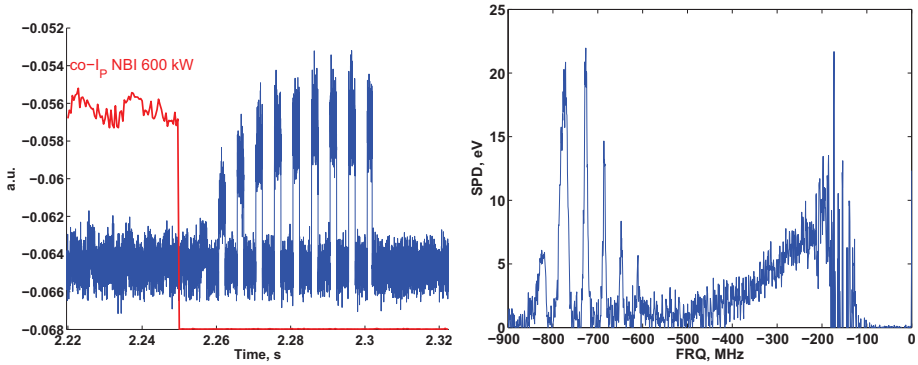

(a) (b)

Figure 8.5: (a) Relative plot of the raw CTS signal in one of the receiver channel no 31 sensitive to the signal in the corresponding frequency range in discharge 111802 is shown in blue, and the power of co-I_p NBI is shown in red; (b) Mean CTS spectrum of the same discharge at about t = 2.29 s. Signal in the frequency range [-200 0] MHz is masked by the notch filter.

activity at switching-on time which disappears in the course of injection. During the steady-state RUDI operation, the distance between the peaks in Fig. 8.5(b) increases monotonically with increasing frequency (in absolute values). It is worth mentioning the stabilizing effect of co-I_p NBI on RUDI - triggered an instability. When the RUDI beam is switched on during the co-I_p injection, neither transient nor steady-state ICE activity is detected. At the moment when the heating NBI is switched off and the RUDI beam remains operating, an ICE signal emerges. At the moment when RUDI is switched off, the instability signal disappears immediately, which indicates that the instability is caused by fast ions which are not confined in the plasma volume where the instability originates from.

8.2.5 Comparison to Previous Observations on Other Machines

The ICE activity observed on TEXTOR by CTS has some features which makes it different from observations on TFTR, JET and Wendelstein 7-AS. In TEXTOR, the CTS does not see the signal at frequencies 150 - 200 MHz away from the gyrotron frequency (0 MHz in the graphs in this chapter) due to the notch filters, so it is technically unable to detect the very first harmonics of ICE. However, CTS detects signal starting from minimum 250 MHz away from the gyrotron line and it is clear that there

is no other peak missing. In contrast to that, ICE on JET and TFTR had signal at rather low frequencies and corresponded to maximum first five harmonics of the ion cyclotron frequency. Secondly, in contrast to previous observations, the peaks are not equidistant in frequency, hence most likely RUDI and counter-I_p NBI cause different kinds of instabilities. This topic requires future investigation and modelling because the instability is highly dependent on the shape of the ion distribution function.

8.3 Stability Analysis of Lower Hybrid Instability

The lower hybrid instability [134,135] was suspected to be driven by counter-I_p and diagnostic transverse NBI. The fast ion distribution function is calculated with the ASCOT code, see Fig. 8.6. The ASCOT code is used because good agreement between the fast ion CTS measurements and the simulated velocity distribution function produced by ASCOT was found, see Chaptersec:spatresolved and reference 1. Fig. 8.6 shows slices of the 5D velocity distribution functions $(v_{||}, v_{\perp 1}, v_{\perp 2}, R, z)$ for counter-I_p NBI (plots (a), (c), (e), (g)) and co-I_p NBI (plots (b), (d), (f), (h)) at R = 1.4, 1.6, 1.8, 2.0, 2.2 m, and $z = 0$. The stability analysis is performed only for the co- and counter-I_p NBI, the distribution function for the RUDI beam is unavailable. In order for the lower hybrid instability to be excited, the double resonance condition should be fulfilled (see Eq. (8.7)). Basically it means that the instability could appear at frequencies where the lower hybrid frequency coincides with the harmonics of ion cyclotron frequency. Fig. 8.7 shows lower hybrid frequency ($\omega_{LH}^2 = (\Omega_{ci}^{-1}\Omega_{ce}^{-1} + \omega_p^{-2})^{-1}$) in TEXTOR discharge 111802, which is typical for TEXTOR plasmas during the CTS experiments. One can see that the lowest lower hybrid frequency is in the plasma at low field side and it is much higher than the frequency at which the instability is observed. However, the stability of the fast ion distribution function during the counter-I_p injection is investigated. For this the H_n function from Eq. (8.7) is calculated. The sign of the function determines the stability of the lower hybrid wave when the double resonance condition is satisfied. Fig. 8.8 shows the sign of H_n as a function of major radius and a harmonic number of ion (hydrogen) cyclotron resonance. The function is calculated using the distribution functions simulated with ASCOT. One can see that for harmonic numbers which could correspond to the observations (i.e. ≈ 15) the lower hybrid instability cannot be excited by the counter-I_p NBI (Fig. 8.8(a)). In contrast, the fast ion distribution for co-I_p NBI looks more unstable and at lower values of magnetic field may result in lower hybrid instability, which is not observed experimentally. For the CTS experiments the lower hybrid frequency is very high, and no activity at relevant frequency range is observed. Moreover, it is known that lower hybrid waves have very narrow angular spectrum and propagate strictly perpendicular to the magnetic

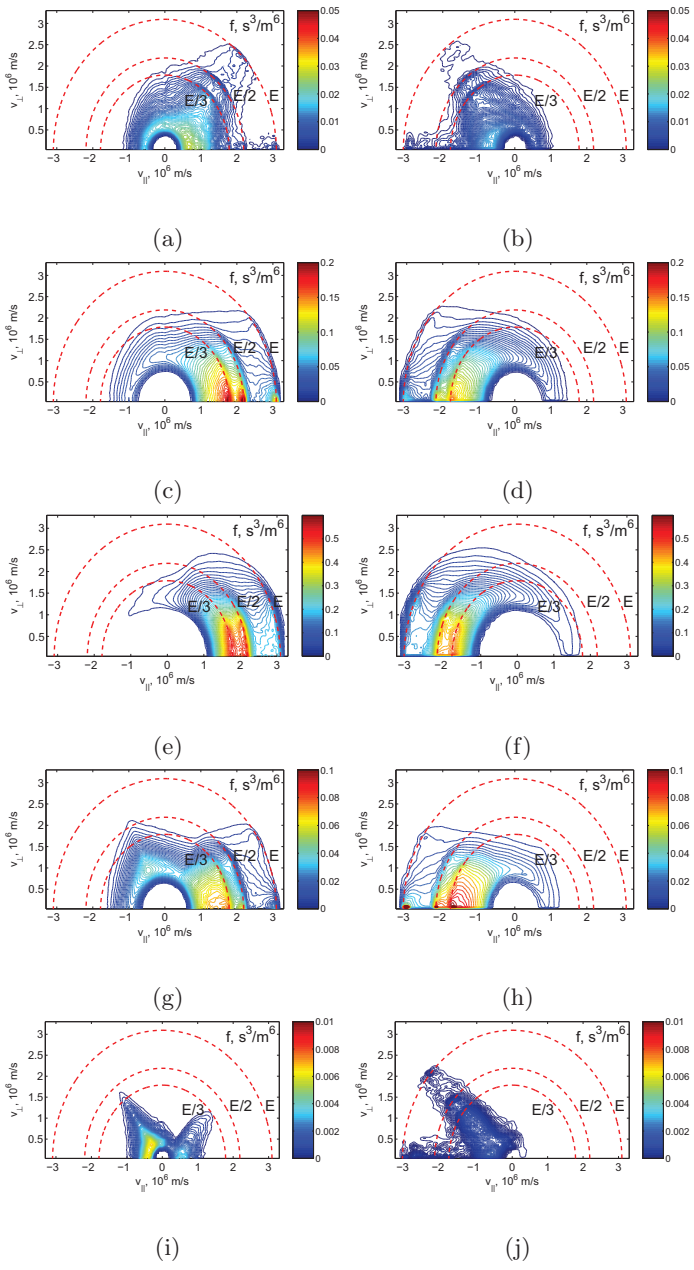

Figure 8.6: Full fast ion distribution function for counter- ((a), (c), (e), (g), (i)) and co-I_p ((b), (d), (f), (h), (j)) NBI at R = 1.4 m ((a), (b)), R = 1.6 m ((c), (d)), R = 1.8 m ((e), (f)), R = 2.0 m ((g),(h)), and R = 2.2 m ((i),(j)), $z = 0$. The simulations were conducted by T. Koskela and O. Asunta

field lines. In the CTS observation, the projection angle ϕ may deviate from perpendicular significantly, nevertheless the ICE activity is observed.

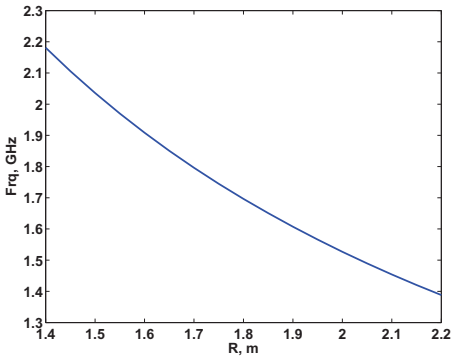

Figure 8.7: Lower hybrid frequency as a function of major radius in the TEXTOR CTS experiments.

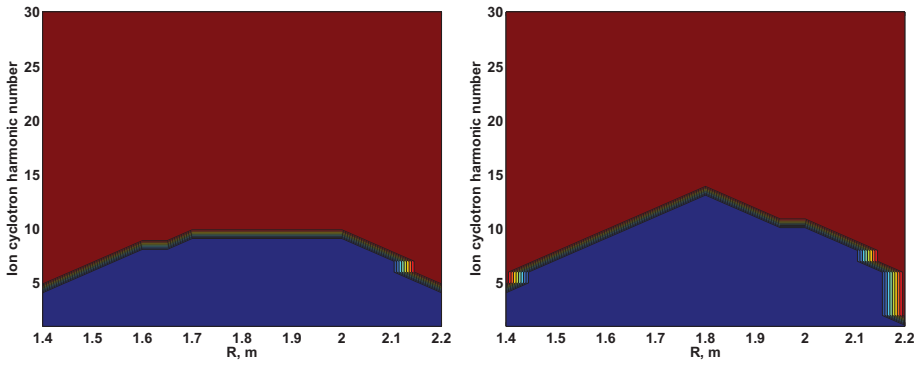

(a) (b)

Figure 8.8: Sign of the H_n as a function of major radius and harmonic number of ion cyclotron frequency for counter- (a) or co-I_p (b) NBI for TEXTOR discharge 111802. Red corresponds to stable and blue to unstable region, H_n is calculated using the distribution functions simulated with ASCOT.

8.3.1 Future Experiments

Due to the notch filters, the CTS diagnostic is not capable to monitor the activity at frequencies closer than 150 MHz to the probing frequency. In order to monitor the instabilities (if any) at lower frequencies, i.e. first harmonics of ion cyclotron emission, a new set of experiments is prepared. They will be conducted in TEXTOR in January 2012 using the ICRH antennae for receiving the radiation and using the fast oscilloscope for data acquisition. The waveforms of proposed experiments are shown in Fig. 8.9. Experiments will be conducted for two different NBI scenarios, with and without counter-I_p

NBI and RUDI. The acquisition is planned at the certain parts of discharge in order to detect instability at different regimes:

- Transient activity due to counter-I_p NBI or RUDI switch-on.
- Developed instability without co-I_p NBI (counter-I_p NBI or RUDI is switched on).
- Transient activity due to co-I_p NBI switch-on (counter-I_p NBI or RUDI is switched on).
- Transient activity due to counter-I_p NBI or RUDI switch-off (co-I_p NBI is switched on).
- Transient activity due to counter-I_p NBI or RUDI switch-on (co-I_p NBI is switched on).
- Transient activity due to co-I_p NBI switch-off (counter-I_p NBI or RUDI is switched on).
- Transient activity due to counter-I_p NBI switch-off (co-I_p NBI is switched off).

Unfortunately, the CTS diagnostic is no longer available at TEXTOR. However, plasma parameters in the future experiments will be the same as they were during the CTS experiments, so that the experimental results can be compared. The experimental parameters are listed in Table 8.1. For the smallest and largest target densities we intend to make a power scan of co-I_p NBI in order to see at which particular power a stabilizing effect disappears (if there is a threshold).

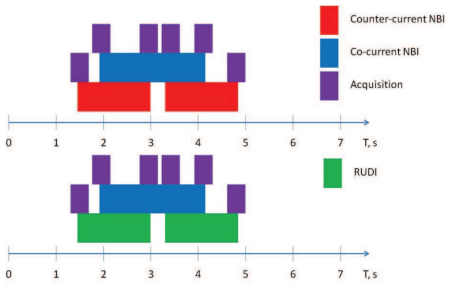

Figure 8.9: Waveforms of proposed experiments for detection of instabilities in ion cyclotron range.

8.4 Conclusions

In the CTS experiments instability was observed during counter-I_p NBI, as well as during RUDI operation. The instability appears in the standard

Target density, 10^19 m$^-3$	3 - 5
Counter-I_p NBI power, MW	1.2
Co-I_p NBI power, MW	up to 1.2
RUDI current, A	1
Beam ions	Hydrogen
Acquisition duration, ms	Depends on fast memory available

Table 8.1: Experimental parameters for proposed measurements of fast ion - induced instabilities in ion cyclotron range.

CTS receiver as significant peaks in two - four frequency channels symmetrically located with respect to the gyrotron frequency. The structure of the instability, revealed by the CTS diagnostic with high frequency resolution, shows multiple peaks separated by frequency which can be interpreted as ion cyclotron frequency of hydrogen or deuterium originated from inside the plasma. Spacing between the peaks is not constant and monotonically increases (RUDI operation, transient activity because counter-I_p NBI switch on) or decreases (steady-state scenario with counter-I_p NBI). In all cases except for discharge 111518 there is no hint of activity at low frequency at the very first harmonics of ion cyclotron frequency. Stabilizing effect of co-I_p NBI is found in RUDI experiments. The instability signature from RUDI injectors disappears immediately after the RUDI is switched off, which indicates that the instability originates from unconfined fast ions (i.e. with no slowing down distribution function).
The stability analysis for steady-state counter-I_p NBI does not confirm that the emission originates from the lower hybrid instability at double resonance condition. This instability was under suspicion because of the frequency range where it was observed.
The instability contaminates the CTS spectrum and requires further investigations. In case it appears only as sharp lines in the spectrum which are discussed above, they can be filtered from the CTS spectrum numerically and cause no more complications for the fast ion analysis. However, if this fast ion induced instability has continuum part of the spectrum, filtering it out from the CTS spectrum is not trivial. Thus further experimental and theoretical investigations are necessary.
Future experiments at TEXTOR with the ICE antenna are foreseen in order to detect any possible signatures of the instability in the frequency range which is blocked by the notch filters in the CTS diagnostic.

Chapter 9

Destabiliziation of Sawteeth Oscillations Stabilized by Fast Ions in ASDEX Upgrade tokamak

This chapter is based on the project which results are described in reference 143. Sawtooth instability is is triggered by an unstable $(m, n) = (1, 1)$ kink mode. A brief introduction into the theory of sawtooth oscillations is given in Section 2.2.4. Sawtooth oscillations do not cause many problems for tokamak operation themselves. But, if the sawtooth activity is stabilized for any reason, and there is a lot of energy accumulated in between the crashes, they might trigger an NTM which potentially might lead to a disruption [144]. As it is known, fast ions may stabilize sawtooth instability [145], see Fig. 9.1. Stabilized sawtooth oscillation release a lot of energy at the time of crash and are very likely to cause NTM and lead to a disruption. More detailed description of the sawtooth instability can be found in Section 2.2.4 and references therein. ITER will be able to tolerate a few disruptions only, however it will have a large population of particles in the core with energies of the MeV range, both from fusion and ICRF heating. Thus a scenario for sawtooth destabilization for ITER-like conditions has to be developed. A technique which can influence a period of sawtooth oscillations is controlled deposition of gyrotron power and a drive of current [146]. The relevant experiments conducted in ASDEX Upgrade are described in this chapter.

9.1 Experiments on Sawteeth Destabilization

The key parameters of the experiments on sawtooth destabilization experiments are listed in Table 9.1. Destabilization is performed in the H-mode

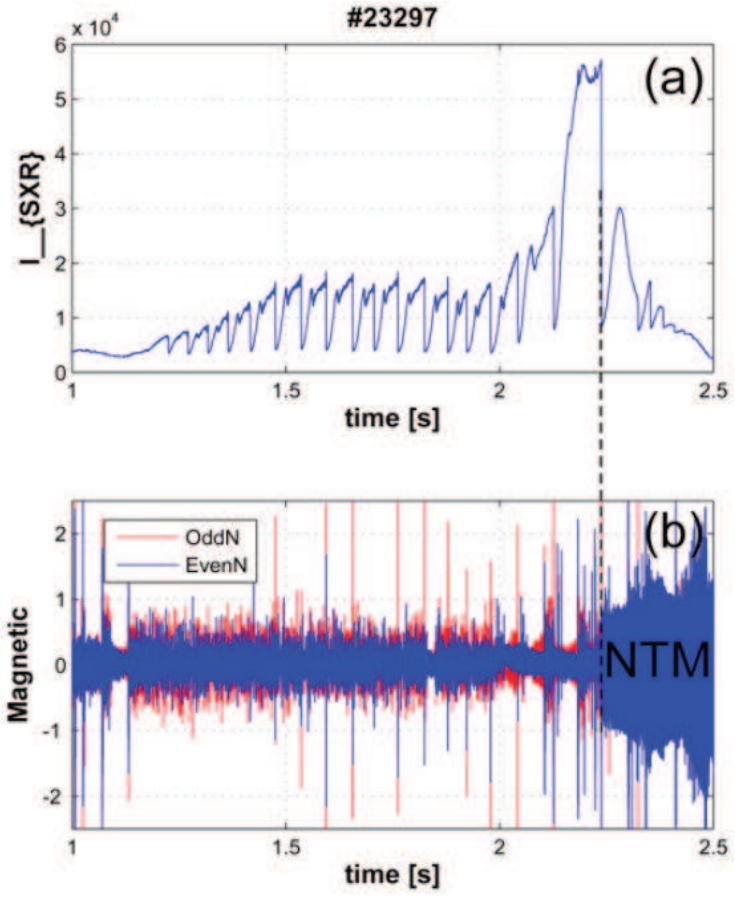

Figure 9.1: A time trace of the soft X-ray diagnostic signal on ASDEX Upgrade (above) which illustrates the sawtooth crash. Analysed data from Mirnov coils show time traces of the modes with even and odd toroidal number. Figure is taken from reference 95.

I_p, MA	1
B_t, T	2.5
n_e, m^{-3}	$8 \cdot 10^{19}$
q_{95}	4.7
P_{NBI}, MW	2.5
P_{ICRH}, MW	4.3 - 4.4
P_{ECRH}, MW	0.8
P_{ECCD}, MW	1

Table 9.1: Key experimental parameters of the sawtooth destabilization experiments on ASDEX Upgrade.

discharges. The gyrotron from the new ECRH system on ASDEX Upgrade [147, 148] is used for the central heating at 140 GHz and is always switched on in order to avoid accumulation of heavy impurities in the plasma core [149]. Another 140 GHz gyrotron, from the old ECRH system, is used for electron cyclotron current drive (ECCD). Comparing temperature profiles the ECCD gyrotron power modulation, we concluded that it does not influence the electron temperature profile, so the effect of the ECCD deposition on the electron temperature is neglected. Equilibrium studies showed that ECCD does not perturb it much, but magnetic shear in the vicinity of the $q = 1$ surface is significantly affected. The total current deposited by ECCD is varied between 1.9 and 2.5 kA, which is two orders of magnitude smaller than the total current inside the $q = 1$ surface.
Fast ions which stabilize $(m, n) = (1, 1)$ kink mode are produced by central ICRH.

9.2 Experimental Results

The influence of the location of ECCD deposition on the stabilization or destabilization of the sawtooth instability are studied. The main results are presented in Fig. 9.2. Changes in the deposition location of gyrotron power are achieved by using steerable mirrors which allow to sweep the beam across the plasma cross-section, from inside to outside of the $q = 1$ surface. ECCD is generated in co-current direction. One can clearly see from Fig. 9.2 that ECCD generated inside the $q = 1$ surface reduces the sawtooth period by approximately 40%. Contrarily, current drive generation outside the $q = 1$ surface increases the period of sawtooth oscillations significantly. Broad deposition profiles shown in Fig. 9.3 are due to off-axis injection geometry of the gyrotron beam, thus having purely geometric origin. It also mimics the situation in ITER where deposition profiles are also expected to be broad. In future experiments the new ECRH system will also be used for ECCD generation and will result in the narrower current deposition profile.

9.3 Analysis and Discussion

Simulations of discharge 25856 are performed in order to investigate the stability of it with Porcelli criterion [49]. As it was mentioned above (Section 2.2.4), the criterion does not provide any information on evolution of the crash, but indicates whether plasma is stable to the kink instability or not. The HAGIS code which utilizes a drift-kinetic approach is used to evaluate a contribution of fast ions to stability of the kink mode. It is needed to estimate how efficient the shear of magnetic field next to the $q = 1$ surface can be to trigger or stabilize the crash. The MISHKA-1 linear MHD stability code is used for MHD modelling of the discharge. The wave-particle

interaction code HAGIS [40] is also used for modelling of the influence of fast ions on the stability of kink mode. The fast ion distribution function originating from ICRH is considered to be bi-Maxwellian [150]:

$$f_{ICRH} = \sqrt{\left(\frac{m}{2\pi}\right)^3}\frac{n_c(r)}{T_\perp(r)\sqrt{T_{||}(r)}} exp\left(-\frac{\mu B_c}{T_\perp(r)} - \frac{|E-\mu B_c|}{T_{||}(r)}\right) \qquad (9.1)$$

where μ is the magnetic moment, B_c is the critical magnetic field at the resonance, n_c is the local density where $B = B_c$, E is the kinetic energy of hydrogen, $||$ and $\perp$ denote components along and perpendicular to the magnetic field. NBI-born fast ions are represented by asymmetric slowing-down distribution function which is Gaussian radially and angularly [151]:

$$f_{NBI} = Cexp\left(\frac{\psi-\psi_0}{\Delta\psi}\right) exp\left(\frac{\lambda-\lambda_0}{\Delta\lambda}\right)\frac{1}{E^{3/2}-E_c^{3/2}} Erf\left(\frac{E-E_0}{\Delta E}\right) \qquad (9.2)$$

Here $\Delta\psi = 0.1$, $\lambda_0 = 0.5$, $E_0 = 80$ keV, $E_c = 3$ keV, $\Delta E = 3.5$ keV.
By creating an external current drive, the equilibrium profile is perturbed. This perturbation is taken into account by the HELENA code, the current drive profiles are calculated using the beam-tracing code TORBEAM [78]. According to SXR observations, the radius of $q = 1$ surface is fixed, however the central value of the safety factor changes during the sawtooth period slightly (by approximately 10%). The safety factor, magnetic shear and the ECCD deposition profiles are shown in Fig. 9.3 at three different moments of time, when ECCD is deposited at different poloidal locations. One can clearly see that the magnetic shear plays the strongest role in stabilization/destabilization of the sawteeth. Fig. 9.4 shows changes in the potential energy of the internal kink mode at three different moments in discharge 25856. The fast ion contribution did not really experience any changes due to immobility of the $q = 1$ surface. However, the fluid drive varies significantly because the current is deposited at a different location in the plasma (the scan is made from inside to outside of $q = 1$ surface). The Porcelli threshold for the instability [49] is depicted by the black line. One can clearly see that when the ECCD is deposited inside the sawtooth inversion radius, the change of modes potential energy is getting closer to the threshold which yields more frequent sawteeth. The same is observed in experiment (Fig. 9.2). It is worth to notice that these results also agree with the results from Tore-Supra [146].

9.4 Conclusions

The experiments on sawtooth destabilization by ECCD revealed a large potential of this method for the sawtooth period control in tokamaks. The total

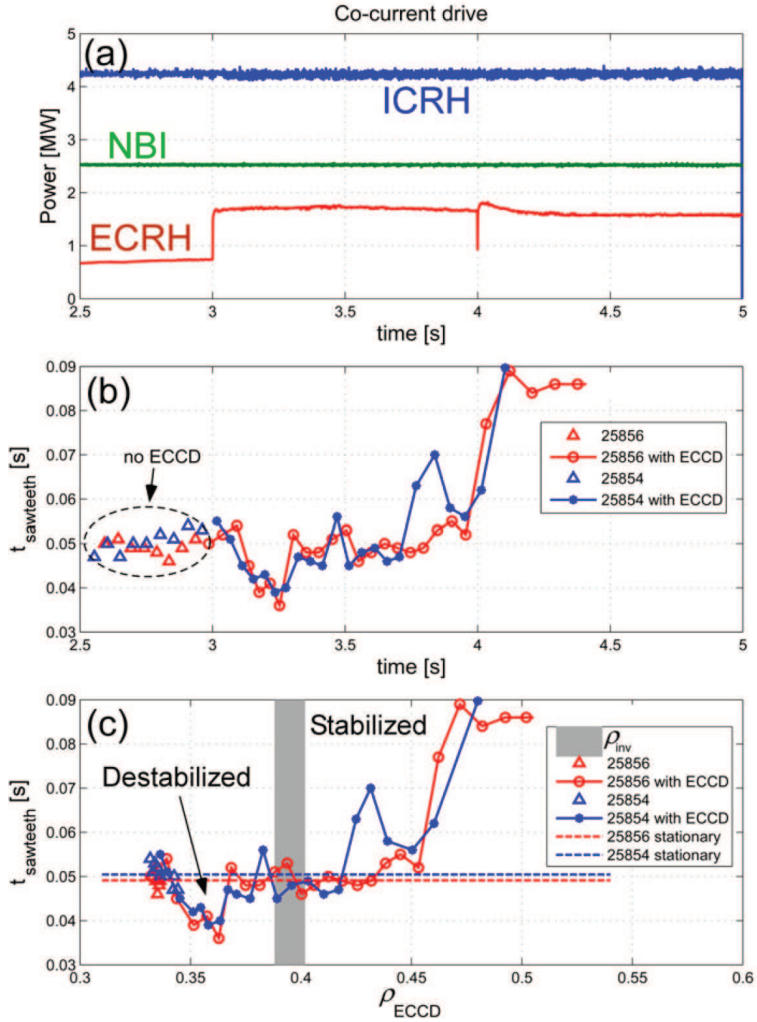

Figure 9.2: (a) Heating power during the experiment; (b) Changes of sawtooth period in the course of the discharge; (c) Sawtooth period as a function of the deposition location of ECCD. Figure is taken from reference 143.

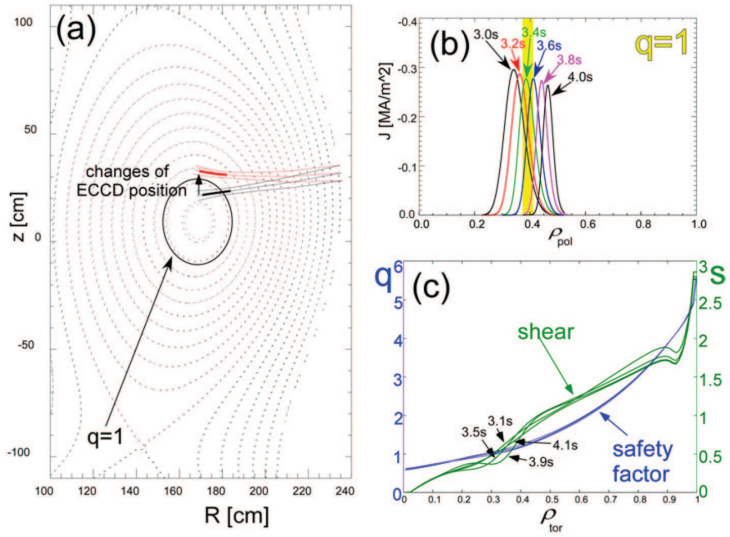

Figure 9.3: (a) Changes of co-current ECCD deposition profile due to the mirror sweep in shot 25856; (b) ECCD deposition profiles at different moments in shot 25856; (c) Magnetic shear and q profiles at different moments in shot 25856. Figure is taken from reference 143.

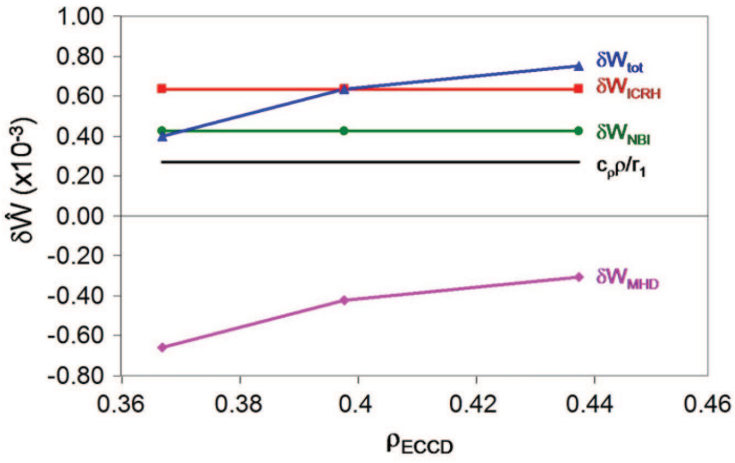

Figure 9.4: Change of potential energy of the internal kink mode. Stabilizing effect of fast particles is depicted as δW_{ICRH} and δW_{NBI}, MHD contribution is represented by δW_{MHD} and the total change of the mode's potential energy is shown as δW_{tot} in discharge 25856 at three different moments of time: 3.25 s, 3.50 s and 3.75 s when the location of the deposition of ECCD was different. Porcelli triggering criterion is shown in black. Figure is taken from reference 143.

microwave-driven current needed for destabilization and seeded by a single gyrotron, is rather moderate and is in the order of 1% of the total current enclosed into the $q = 1$ magnetic surface. The reduction of the sawtooth period of the fast ion stabilized sawtooth by co-I_p ECCD is approximately 40%. Counter-I_p ECCD deposition does not reveal a destabilization effect on the sawteeth. The stability analysis reveals that the magnetic shear in the vicinity of $q = 1$ plays an important role in changing the potential energy of the mode, bringing it closer or further away from the crash.
Even though the experiments showed a significant reduction in the sawtooth period by applying ECCD, further experiments are planned in order to find an optimal deposition of the current in the plasma and investigate an influence of the destabilization method on fast ion confinement. In order to do that, a work on scenario development is necessary because the discharges described in this chapter and in reference [143] had a very high density when the fast ion measurements are limited.

Chapter 10

Conclusions

This chapter concludes the thesis and summarizes the results of the author's work as a PhD student. It also contains a brief overview of the future work.
The cross-calibration software developed by the author (described in Section 4.4.2) allowed calibration of the ASDEX Upgrade CTS receiver, including the transmission line.
A feasibility study for the calibration of the CTS receiver with a hot source (an improvement for the liquid nitrogen calibration), described in Section 4.4.1, showed impossibility of its installation at the present CTS system on ASDEX Upgrade, but it can be considered for future CTS diagnostics.
The secondary emission (Section 4.5) signal was studied. Even though there is still no firm conclusion on the origin of it, the CTS group got a hint that the signal is related to possible reflections of the incident radiation from construction elements of a vacuum vessel. This hypothesis requires further experimental investigation.
A technique for the elevation alignment check, based on the measurements of the shape of the sawtooth oscillations, was introduced. The technique, implemented at TEXTOR, could allow the precision of the alignment of 1.5°. Even greater precision can be achieved after additional analysis. A journal publication will be prepared based on these results.
A comprehensive comparison of the measured and simulated fast ion velocity distribution functions was performed at TEXTOR, see Chapter 6. The experimental results, obtained by the CTS diagnostic at different radial locations and projection angles, were compared to the simulations performed by the Monte Carlo codes ASCOT and VENUS. The comparison showed a good agreement between the measurements on the magnetic axis for two different projection angles and the numerical simulations. A significant discrepancy was found for the off-axis case. Sensitivity analysis performed by ASCOT showed that for the measurements with a more parallel projection angle the discrepancy cannot be explained by uncertainties in plasma parameters. Thus, anomalous fast ion transport was proposed.

The influence of resonant magnetic perturbations (RMP) on fast ion confinement was studied in the TEXTOR tokamak. The experiments are described in Chapter 7. The dynamic ergodic divertor, DED, which produces the RMP, operated in the DC mode and had $(m, n) = (3, 1)$ and $(m, n) = (6, 2)$ configurations. The experiments intended to measure the influence by detecting fast ions slowing-down time during the modulations of the NBI power. Unfortunately, no firm conclusion could be drawn because the CTS data for the $(m, n) = (3, 1)$ DED configuration were contaminated with the secondary emission signal or the DED seeded a locked mode in the plasma. The results from the CTS experiments with the $(m, n) = (6, 2)$ DED configuration revealed that the difference in the slowing down time between shots with and without DED can be explained by the effect of density. The slowing down time in the experiment with the decaying magnetic island $(m, n) = (2, 1)$ was similar to the those in the reference experiment. However, the evolution of noise in the CTS data was significantly different from the reference experiment. The fast ion velocity distribution function was not inferred due to the lack of time and computer problems. However, this is foreseen for the future.

During counter-I_p NBI operation at TEXTOR, a strong spiky signal was found in the CTS spectra (described in Chapter 8). Similar signal was observed during the injection from the low power diagnostic injector RUDI, which launches a beam perpendicular to the magnetic field. Detailed investigation of the spectra allowed to classify the observed signal and compare it to the previous observations from JET, TFTR and Wendelstein 7-AS. Stability analysis of the lower hybrid instability using the simulated velocity distribution functions (ASCOT) did not show a positive growth rate at frequencies where the activity was observed. Future experiments are foreseen on TEXTOR using the ICRH antenna for receiving the signal. This will be done in order to make more detailed comparison between the results from TEXTOR and the results from other machines. The TEXTOR CTS results are not compared directly because different frequency ranges are covered at different machines. The results from JET and TFTR primarily cover a frequency range from zero to the first several harmonics of ICE. The CTS results report emission at frequencies which correspond the ion cyclotron harmonic number of more than ten, the first harmonics of ICE are not observable due to the notch filters.

In order to prevent sawtooth stabilization due to fast ions in ITER, and therefore reduce the risk of triggering NTM, a sawtooth destabilization by means of ECCD technique was implemented at ASDEX Upgrade. By depositing ECCD right inside the $q = 1$ surface, the sawtooth period was reduced by 40%. Modelling showed that the effect is achieved by changing the magnetic shear in the vicinity of the $q = 1$ surface. The results agree well with previous findings from Tore Supra. Future experiments on the influence of destabilized sawtooth on the fast ion confinement are foreseen

on ASDEX Upgrade.

Bibliography

[1] D Moseev, F Meo, S B Korsholm, T Koskela, M Albergante, O Asunta, H Bindslev, A Bürger, V Furtula, M Kantor, F Leipold, P K Michelsen, S K Nielsen, M Salewski, O Schmitz, M Stejner, and E Westerhof. Comparison of measured and simulated fast ion velocity distributions in the TEXTOR tokamak. *Plasma Physics and Controlled Fusion*, 53(10):105004, 2011.

[2] A Grubler and A McDonald. *Global Energy Perspectives*. Cambridge University Press, 1998.

[3] J Ongena and G Van Oost. Energy for future centuries: Prospects for fusion power as a future energy source. *Fusion Science and Technology*, 57(2T):3–15, 2010.

[4] J D Lawson. SOME CRITERIA FOR A POWER PRODUCING THERMONUCLEAR REACTOR. *Proceedings of the Physical Society of London Section B*, 70(1):6–10, 1957.

[5] George H Miller, Edward I Moses, and Craig R Wuest. The National Ignition Facility: enabling fusion ignition for the 21st century. *Nuclear Fusion*, 44(12):S228–S238, December 2004.

[6] R V Budny. Fusion alpha parameters in tokamaks with high DT fusion rates. *Nuclear Fusion*, 42(12):1383–1393, December 2002.

[7] G Taylor, J Strachan, R V Budny, and D Ernst. Fusion Heating in a Deuterium-Tritium Tokamak Plasma. *Physical Review Letters*, 76(15):2722–2725, April 1996.

[8] P Thomas, P Andrew, B Balet, D Bartlett, J Bull, B de Esch, A Gibson, C Gowers, H Guo, G Huysmans, T Jones, M Keilhacker, R Koenig, M Lennholm, P Lomas, A Maas, F Marcus, F Nave, V Parail, F Rimini, J Strachan, K-D Zastrow, and N Zornig. Observation of Alpha Heating in JET DT Plasmas. *Physical Review Letters*, 80(25):5548–5551, June 1998.

[9] M J Mantsinen, M-L Mayoral, V Kiptily, S E Sharapov, B Alper, A Bickley, M de Baar, L-G Eriksson, A Gondhalekar, T Hellsten, K Lawson, F Nguyen, J-M Noterdaeme, E Righi, A Tuccillo, and M Zerbini. Alpha-Tail Production with Ion-Cyclotron-Resonance Heating of H4e-Beam Ions in JET Plasmas. *Physical Review Letters*, 88(10), February 2002.

[10] Y Takeiri, O Kaneko, Y Oka, K Tsumori, M Osakabe, R Akiyama, T Kawamoto, and E Asano. Construction of negative-ion-based NBI system in Large Helical Device. In *17th IEEE/NPSS Symposium Fusion Engineering (Cat. No.97CH36131)*, volume 1, pages 409–412. IEEE.

[11] M Kuriyama. Operation of the negative-ion based NBI for JT-60U. *Fusion Engineering and Design*, 39-40(1-4):115–121, September 1998.

[12] S Mochalskyy, A F Lifschitz, and T Minea. 3D modelling of negative ion extraction from a negative ion source. *Nuclear Fusion*, 50(10):105011, October 2010.

[13] M A Van Zeeland, W W Heidbrink, and J H Yu. Fast ion D α imaging in the DIII-D tokamak. *Plasma Physics and Controlled Fusion*, 51(5):055001, May 2009.

[14] W W Heidbrink. Fast-ion Dα measurements of the fast-ion distribution (invited). *The Review of scientific instruments*, 81(10):10D727, October 2010.

[15] V G Kiptily, J M Adams, L Bertalot, A Murari, S E Sharapov, V Yavorskij, B Alper, R Barnsley, P de Vries, C Gowers, L-G Eriksson, P J Lomas, M J Mantsinen, A Meigs, J-M Noterdaeme, and F P Orsitto. Gamma-ray imaging of D and 4 He ions accelerated by ion-cyclotron-resonance heating in JET plasmas. *Nuclear Fusion*, 45(5):L21–L25, May 2005.

[16] M Tardocchi, L I Proverbio, G Gorini, G Grosso, M Locatelli, I N Chugonov, D B Gin, A E Shevelev, A Murari, V G Kiptily, B Syme, A M Fernandes, R C Pereira, and J Sousa. Gamma ray spectroscopy at high energy and high time resolution at JET. *Review of Scientific Instruments*, 79(10):10E524, October 2008.

[17] W W Heidbrink and G J Sadler. The behaviour of fast ions in tokamak experiments. *Nuclear Fusion*, 34(4):535–615, April 1994.

[18] D Testa and A Gondhalekar. Fast ion density measurements using high energy neutral particle analysis in JET. *Nuclear Fusion*, 40(5):975–988, May 2000.

[19] M Garcia-Muñoz, H-U Fahrbach, and H Zohm. Scintillator based detector for fast-ion losses induced by magnetohydrodynamic instabilities in the ASDEX upgrade tokamak. *Review of Scientific Instruments*, 80(5):053503, May 2009.

[20] D Jiménez-Rey, B Zurro, J Guasp, M Liniers, A Baciero, M Garcia-Muñoz, A Fernández, G García, L Rodríguez-Barquero, and J M Fontdecaba. A flexible luminescent probe to monitor fast ion losses at the edge of the TJ-II stellarator. *The Review of scientific instruments*, 79(9):093511, September 2008.

[21] M Nishiura, M Isobe, T Saida, M Sasao, and D S Darrow. Scintillator probe diagnostic for high energy particles escaped from Large Helical Device. *Review of Scientific Instruments*, 75(10):3646, October 2004.

[22] G Tardini, A Zimbal, B Esposito, F Gagnon-Moisan, D Marocco, R Neu, and H Schuhmacher. First neutron spectrometry measurements in the ASDEX Upgrade tokamak. In *FNDA*, page 60, Ein Gedi, Dead Sea, Israel, 2011.

[23] H Bindslev, S K Nielsen, L Porte, J A Hoekzema, S B Korsholm, F Meo, P K Michelsen, S Michelsen, J W Oosterbeek, E L Tsakadze, E Westerhof, and P Woskov. Fast-Ion Dynamics in the TEXTOR Tokamak Measured by Collective Thomson Scattering. *Physical Review Letters*, 97(20):205005, November 2006.

[24] F Meo, M Stejner, M Salewski, H Bindslev, T Eich, V Furtula, S B Korsholm, F Leuterer, F Leipold, P K Michelsen, D Moseev, S K Nielsen, B Reiter, J Stober, D Wagner, and P Woskov. First results and analysis of collective Thomson scattering (CTS) fast ion distribution measurements on ASDEX Upgrade. *Journal of Physics: Conference Series*, 227(1):012010, May 2010.

[25] S K Nielsen, H Bindslev, L Porte, J A Hoekzema, S B Korsholm, F Leipold, F Meo, P K Michelsen, S Michelsen, J W Oosterbeek, E L Tsakadze, G Van Wassenhove, E Westerhof, and P Woskov. Temporal evolution of confined fast-ion velocity distributions measured by collective Thomson scattering in TEXTOR. *Physical Review E*, 77(1):016407, January 2008.

[26] F Meo, H Bindslev, S B Korsholm, V Furtula, F Leuterer, F Leipold, P K Michelsen, S K Nielsen, M Salewski, J Stober, D Wagner, and P Woskov. Commissioning activities and first results from the collective Thomson scattering diagnostic on ASDEX Upgrade (invited). *The Review of scientific instruments*, 79(10):10E501, October 2008.

[27] S B Korsholm, H Bindslev, V Furtula, F Leipold, F Meo, P K Michelsen, D Moseev, S K Nielsen, M Salewski, and M Stejner. Collective Thomson scattering capabilities to diagnose fusion plasmas. *Nuclear Instruments and Methods in Physics Research Section A: Accelerators, Spectrometers, Detectors and Associated Equipment*, 623(2):677–680, November 2010.

[28] B Streibl, A Zeisberg, and P Gagliardi. The ASDEX upgrade TF coils: design to acceptance. *IEEE Transactions on Magnetics*, 24(2):1248–1251, March 1988.

[29] S D Pinches, V G Kiptily, S E Sharapov, D S Darrow, L-G Eriksson, H-U Fahrbach, M Garcia-Muñoz, M Reich, E Strumberger, and A Werner. Observation and modelling of fast ion loss in JET and ASDEX Upgrade. *Nuclear Fusion*, 46(10):S904–S910, October 2006.

[30] S D Pinches, H L Berk, D N Borba, B N Breizman, S Briguglio, A Fasoli, G Fogaccia, M P Gryaznevich, V Kiptily, M J Mantsinen, S E Sharapov, D Testa, R G L Vann, G Vlad, and F Zonca. The role of energetic particles in fusion plasmas. *Plasma Physics and Controlled Fusion*, 46(12B):B187–B200, December 2004.

[31] G Sadler, P Barabaschi, E Bertolini, S Conroy, S Corti, E Deksnis, K J Dietz, H P L de Esch, A Gondhalekar, B Green, M Huart, M Huguet, J Jacquinot, O N Jarvis, A Khudoleev, M J Loughlin, R Konig, J Last, A Maas, M Petrov, S Putvinskii, C Sborchia, D Stork, B Tubbing, and P van Belle. Effects of enhanced toroidal field ripple on JET plasmas. *Plasma Physics and Controlled Fusion*, 34(13):1971–1976, December 1992.

[32] V Basiuk, L-G Eriksson, V Bergeaud, M Chantant, G Martin, F Nguyen, R Reichle, J C Vallet, L Delpeche, and F Surle. Ripple losses during ICRF heating in Tore Supra. *Nuclear Fusion*, 44(1):181–192, January 2004.

[33] S J Zweben, D S Darrow, S H Batha, R V Budny, M Diesso, H W Herrmann, J Giarrusso, M H Redi, H Takahashi, S von Goeler, R B White, and R M Wieland. Effects of q (r) on the alpha particle ripple loss in TFTR. *Nuclear Fusion*, 38(5):739–760, May 1998.

[34] H Kawashima, M Sato, K Tsuzuki, Y Miura, N Isei, H Kimura, T Nakayama, M Abe, and D S Darrow. Demonstration of ripple reduction by ferritic steel board insertion in JFT-2M. *Nuclear Fusion*, 41(3):257–263, March 2001.

[35] M Sato, H Kimura, Y Miura, T Nakayama, K Tobita, H Kawashima, K Tsuzuki, and N Isei. Investigation on ripple loss reduction by ferritic

steel plate insertion in JFT-2M: comparison between experimental and computational data. *Nuclear Fusion*, 42(8):1008–1013, August 2002.

[36] K Shinohara, H Kawashima, K Tsuzuki, K Urata, M Sato, H Ogawa, K Kamiya, H Sasao, H Kimura, S Kasai, Y Kusama, Y Miura, K Tobita, O Naito, and D S Darrow. Effects of complex magnetic ripple on fast ions in JFT-2M ferritic insert experiments. *Nuclear Fusion*, 43(7):586–593, July 2003.

[37] A Fasoli, C Gormenzano, H L Berk, B N Breizman, S Briguglio, D S Darrow, N N Gorelenkov, W W Heidbrink, A Jaun, S V Konovalov, R Nazikian, J-M Noterdaeme, S E Sharapov, K Shinohara, D Testa, K Tobita, Y Todo, G Vlad, and F Zonca. Chapter 5: Physics of energetic ions. *Nuclear Fusion*, 47(6):S264–S284, June 2007.

[38] K McGuire, R Goldston, M Bell, M Bitter, K Bol, K Brau, D Buchenauer, T Crowley, S Davis, F Dylla, H Eubank, H Fishman, R Fonck, B Grek, R Grimm, R Hawryluk, H Hsuan, R Hulse, R Izzo, R Kaita, S Kaye, H Kugel, D Johnson, J Manickam, D Manos, D Mansfield, E Mazzucato, R McCann, D McCune, D Monticello, R Motley, D Mueller, K Oasa, M Okabayashi, K Owens, W Park, M Reusch, N Sauthoff, G Schmidt, S Sesnic, J Strachan, C Surko, R Slusher, H Takahashi, F Tenney, P Thomas, H Towner, J Valley, and R White. Study of High-Beta Magnetohydrodynamic Modes and Fast-Ion Losses in PDX. *Physical Review Letters*, 50(12):891–895, March 1983.

[39] C P von Thun, A Perona, T Johnson, S E Sharapov, M Reich, V G Kiptily, M Cecconello, A Salmi, V Ya Goloborod'ko, S D Pinches, M Garcia-Muñoz, D S Darrow, M Brix, and I Voitsekhovitch. MeV-range fast ion losses induced by fishbones on JET. *Nuclear Fusion*, 50(8):084009, August 2010.

[40] S D Pinches. The HAGIS self-consistent nonlinear wave-particle interaction model. *Computer Physics Communications*, 111(1-3):133–149, June 1998.

[41] S von Goeler, W Stodiek, and N Sauthoff. Studies of Internal Disruptions and m=1 Oscillations in Tokamak Discharges with Soft—X-Ray Tecniques. *Phys. Rev. Lett.*, 33(20):1201–1203, November 1974.

[42] John Wesson. *Tokamaks*. Clarendon Press, 2003.

[43] B B Kadomtsev. Disruptive instability in tokamaks. *Soviet Journal of Plasma Physics*, 1:389, 1976.

[44] B B Kadomtsev. *Collective Phenomena in Plasmas*. Pergamon Press, 1982.

[45] M Yamada, F M Levinton, N Pomphrey, R V Budny, J Manickam, and Y Nagayama. Investigation of magnetic reconnection during a sawtooth crash in a high-temperature tokamak plasma. *Physics of Plasmas*, 1(10):3269, 1994.

[46] F M Levinton, S H Batha, M Yamada, and M C Zarnstorff. q-profile measurements in the Tokamak Fusion Test Reactor. *Physics of Fluids B: Plasma Physics*, 5(7):2554, 1993.

[47] Masaaki Yamada, Russell Kulsrud, and Hantao Ji. Magnetic reconnection. *Rev. Mod. Phys.*, 82(1):603–664, March 2010.

[48] H K Park, A J H Donne, N C Luhmann, I G J Classen, C W Domier, E Mazzucato, T Munsat, M J van de Pol, and Z Xia. Comparison Study of 2D Images of Temperature Fluctuations during Sawtooth Oscillation with Theoretical Models. *Phys. Rev. Lett.*, 96(19):195004, 2006.

[49] F Porcelli, D Boucher, and M N Rosenbluth. Model for the sawtooth period and amplitude. *Plasma Physics and Controlled Fusion*, 38(12):2163–2186, December 1996.

[50] Y Todo, H L Berk, and B N Breizman. Simulation of intermittent beam ion loss in a Tokamak Fusion Test Reactor experiment. *Physics of Plasmas*, 10(7):2888, July 2003.

[51] R O Dendy, C N Lashmore-Davies, and K F Kam. The magnetoacoustic cyclotron instability of an extended shell distribution of energetic ions. *Physics of Fluids B: Plasma Physics*, 5(7):1937, 1993.

[52] A Jaun, S Briguglio, G Fogaccia, C Gormezano, F Zonca, G Vlad, A Fasoli, D Testa, S V Konovalov, L Chen, W W Heidbrink, K Tobita, M Takechi, K Shinohara, A Fukuyama, and K Miyamoto. Collective Modes and Fast Particle Confinement in ITER. In *19th International Conference on Fusion Energy*, Lyon, 2002.

[53] M Garcia-Muñoz, N Hicks, R van Voornveld, I G J Classen, R Bilato, V Bobkov, M Bruedgam, H-U Fahrbach, V G Igochine, S Jaemsae, M Maraschek, and K Sassenberg. Convective and Diffusive Energetic Particle Losses Induced by Shear Alfvén Waves in the ASDEX Upgrade Tokamak. *Phys. Rev. Lett.*, 104(18):185002, 2010.

[54] M Garcia-Muñoz, N Hicks, R van Voornveld, I G J Classen, R Bilato, V Bobkov, M Brambilla, M Bruedgam, H-U Fahrbach, V G Igochine, S Jaemsae, M Maraschek, and K Sassenberg. Fast-ion losses induced by ACs and TAEs in the ASDEX Upgrade tokamak. *Nuclear Fusion*, 50(8):084004, August 2010.

[55] B N Breizman and S E Sharapov. Major minority: energetic particles in fusion plas. *Plasma Physics and Controlled Fusion*, 53(5):054001, May 2011.

[56] T Hauff, M Pueschel, T Dannert, and F Jenko. Electrostatic and magnetic transport of energetic ions in turbulent plasmas. *Physical Review Letters*, 102(7), February 2009.

[57] S Günter, G Conway, S DaGraça, H-U Fahrbach, C Forest, M Garcia-Muñoz, T Hauff, J Hobirk, V G Igochine, F Jenko, K Lackner, P Lauber, P McCarthy, M Maraschek, P Martin, E Poli, K Sassenberg, E Strumberger, G Tardini, E Wolfrum, and H Zohm. Interaction of energetic particles with large and small scale instabilities. *Nuclear Fusion*, 47(8):920–928, August 2007.

[58] W Zhang, Z Lin, and L Chen. Transport of Energetic Particles by Microturbulence in Magnetized Plasmas. *Physical Review Letters*, 101(9), August 2008.

[59] W W Heidbrink, J M Park, M Murakami, C Petty, C Holcomb, and M Van Zeeland. Evidence for Fast-Ion Transport by Microturbulence. *Physical Review Letters*, 103(17), October 2009.

[60] John David Jackson. *Classical Electrodynamics*. John Wiley & Sons, 1998.

[61] E E Salpeter. Electron Density Fluctuations in a Plasma. *Physical Review*, 120(3):1528, 1960.

[62] Donald Gary Swanson. *Plasma Waves*. Taylor & Francis, 2003.

[63] H Bindslev. *On the Theory of Thomson Scattering and Reflectometry in a Relativistic Magnetized Plasma*. PhD thesis, {Risø} National Laboratory, 1992.

[64] H Bindslev. Three-wave mixing and Thomson scattering in plasmas. *Plasma Physics and Controlled Fusion*, 35(11):1615–1640, November 1993.

[65] S K Nielsen. *Fast ion dynamics in TEXTOR plasmas measured by means of collective Thomson scattering (CTS)*. PhD thesis, Danmarks Tekniske Universitet, 2007.

[66] H Bindslev. A quantitative study of scattering from electromagnetic fluctuations in plasmas. *Journal of Atmospheric and Terrestrial Physics*, 58(8):983–989, July 1996.

[67] H Bindslev. Methods for optimizing and assessing diagnostic capability, demonstrated for collective Thomson scattering (invited). *Review of Scientific Instruments*, 70(1):1093, 1999.

[68] M Salewski, S K Nielsen, H Bindslev, V Furtula, N N Gorelenkov, S B Korsholm, F Leipold, F Meo, P K Michelsen, D Moseev, and M Stejner. On velocity space interrogation regions of fast-ion collective Thomson scattering at ITER. *Nuclear Fusion*, 51(8):083014, 2011.

[69] V Furtula, M Salewski, F Leipold, P K Michelsen, S B Korsholm, F Meo, D Moseev, S K Nielsen, M Stejner, and T Johansen. Design and performance of the collective Thomson scattering receiver at ASDEX Upgrade. *submitted to Review of Scientific Instruments*, 2011.

[70] P Woskov, H Bindslev, F Leipold, F Meo, S K Nielsen, E L Tsakadze, S B Korsholm, J Scholten, C Tito, E Westerhof, J W Oosterbeek, F Leuterer, F Monaco, M Muenich, and D Wagner. Frequency measurements of the gyrotrons used for collective Thomson scattering diagnostics at TEXTOR and ASDEX Upgrade. *Review of Scientific Instruments*, 77(10):10E524, October 2006.

[71] S Michelsen, S B Korsholm, H Bindslev, F Meo, P K Michelsen, E L Tsakadze, J Egedal, P Woskov, J A Hoekzema, F Leuterer, and E Westerhof. Fast ion millimeter wave collective Thomson scattering diagnostics on TEXTOR and ASDEX upgrades. *Review of Scientific Instruments*, 75(10):3634, October 2004.

[72] S B Korsholm, H Bindslev, F Meo, F Leipold, P K Michelsen, S Michelsen, S K Nielsen, E L Tsakadze, P Woskov, E Westerhof, J W Oosterbeek, J A Hoekzema, F Leuterer, and D Wagner. Current fast ion collective Thomson scattering diagnostics at TEXTOR and ASDEX Upgrade, and ITER plans (invited). *Review of Scientific Instruments*, 77(10):10E514, October 2006.

[73] S B Korsholm, M Stejner, H Bindslev, V Furtula, F Leipold, F Meo, P K Michelsen, D Moseev, S K Nielsen, M Salewski, M de Baar, E Delabie, M Kantor, and A Bürger. Measurements of Intrinsic Ion Bernstein Waves in a Tokamak by Collective Thomson Scattering. *Phys. Rev. Lett.*, 106(16):165004, April 2011.

[74] M Stejner, S K Nielsen, H Bindslev, S B Korsholm, and M Salewski. Principles of fuel ion ratio measurements in fusion plasmas by collective Thomson scattering. *Plasma Physics and Controlled Fusion*, 53(6):065020, June 2011.

[75] M Stejner, S K Nielsen, S B Korsholm, M Salewski, H Bindslev, V Furtula, F Leipold, F Meo, P K Michelsen, D Moseev, A Bürger, M Kantor, and M de Baar. Collective Thomson scattering measurements with high frequency resolution at TEXTOR. *Review of Scientific Instruments*, 81(10):10D515, October 2010.

[76] D Moseev, M Stejner, S B Korsholm, F Meo, H Bindslev, A Bürger, V Furtula, F Leipold, A A Listopad, P K Michelsen, S K Nielsen, M Salewski, and E Westerhof. CTS observations of NBI-induced instabilities in TEXTOR plasmas. In *38th EPS Conference on Plasma Physics*, page P4.079, 2011.

[77] L D Landau and E M Lifshitz. *The Classical Theory of Fields, Fourth Edition*. Butterworth-Heinemann, 1980.

[78] E Poli, G V Pereverzev, A G Peeters, and M Bornatici. EC beam tracing in fusion plasmas. *Fusion Engineering and Design*, 53(1-4):9–21, January 2001.

[79] D L Jassby, D R Cohn, B Lax, and W Halverson. Tokamak diagnostics with the 496-μm CH 3 F laser. *Nuclear Fusion*, 14(5):745–747, November 1974.

[80] R Behn, D Dicken, J Hackmann, S Salito, M Siegrist, P Krug, I Kjelberg, B Duval, B Joye, and A Pochelon. Ion temperature measurement of tokamak plasmas by collective Thomson scattering of D_{2}O laser radiation. *Physical Review Letters*, 62(24):2833–2836, June 1989.

[81] M Born, H D Dicken, J Hackmann, and J Uhlenbusch. Local ion temperature measurements in the tokamak UNITOR by collective Thomson scattering. *Plasma Physics and Controlled Fusion*, 35(3):391–396, March 1993.

[82] R K Richards, D P Hutchinson, and C H Ma. Design of a CO2-laser Thomson scattering ion-tail diagnostic for Alcator C-Mod. *Review of Scientific Instruments*, 66(1):497, 1995.

[83] J S Machuzak, P Woskov, J Gilmore, N L Bretz, H K Park, R E Aamodt, P Y Cheung, D A Russell, and H Bindslev. TFTR 60 GHz alpha particle collective Thomson scattering diagnostic. *Review of Scientific Instruments*, 66(1):484, 1995.

[84] H Bindslev, L Porte, J A Hoekzema, J Machuzak, P Woskov, D Van Eester, J Egedal, J Fessey, and T Hughes. Fast ion collective Thomson scattering, JET results and TEXTOR plans. *Fusion Engineering and Design*, 53(1-4):105–111, January 2001.

[85] E V Suvorov, V Erckmann, E Holzhauer, W Kasparek, Y A Dryagin, S E Fil'chenkov, A A Fraiman, T Geist, M Kick, L M Kukin, A V Kostrov, L V Lubyako, A M Shtanyuk, N K Skalyga, and O B Smolyakova. Ion temperature and beam-driven plasma waves from collective scattering of gyrotron radiation in W7-AS. *Plasma Physics and Controlled Fusion*, 37(11):1207–1213, 1995.

[86] H Bindslev, S K Nielsen, L Porte, J A Hoekzema, S B Korsholm, F Meo, P K Michelsen, S Michelsen, J W Oosterbeek, E L Tsakadze, E Westerhof, and P Woskov. Fast-ion dynamics in the TEXTOR tokamak measured by collective Thomson scattering. *Plasma Physics and Controlled Fusion*, 49(12B):B551–B562, December 2007.

[87] S K Nielsen, H Bindslev, M Salewski, A Bürger, E Delabie, V Furtula, M Kantor, S B Korsholm, F Leipold, F Meo, P K Michelsen, D Moseev, J W Oosterbeek, M Stejner, E Westerhof, and P Woskov. Fast-ion redistribution due to sawtooth crash in the TEXTOR tokamak measured by collective Thomson scattering. *Plasma Physics and Controlled Fusion*, 52(9):092001, September 2010.

[88] S K Nielsen, M Salewski, H Bindslev, A Bürger, V Furtula, M Kantor, S B Korsholm, H R Koslowski, A Krämer-Flecken, F Leipold, F Meo, P K Michelsen, D Moseev, J W Oosterbeek, M Stejner, and E Westerhof. Dynamics of fast ions during sawtooth oscillations in the TEXTOR tokamak measured by collective Thomson scattering. *Nuclear Fusion*, 51(6):063014, 2011.

[89] F Orsitto, A Brusadin, Yu Brodsky, S Filchenkov, G Grosso, E Giovannozzi, L Lubyako, A Perminov, E V Suvorov, U Tartari, and F Volpe. Characterization and preliminary results of the collective Thomson scattering system on FTU tokamak. *Review of Scientific Instruments*, 70(1):1158, 1999.

[90] M Salewski, F Meo, M Stejner, O Asunta, H Bindslev, V Furtula, S B Korsholm, T Kurki-Suonio, F Leipold, F Leuterer, P K Michelsen, D Moseev, S K Nielsen, J Stober, G Tardini, D Wagner, and P Woskov. Comparison of fast ion collective Thomson scattering measurements at ASDEX Upgrade with numerical simulations. *Nuclear Fusion*, 50(3):035012, March 2010.

[91] M Nishiura, S Kubo, K Tanaka, N Tamura, T Shimozuma, T Mutoh, K Kawahata, T Watari, T Saito, Y Tatematsu, and T Notake. Initial result of collective Thomson scattering using 77 GHz gyrotron for bulk and tail ion diagnostics in the Large Helical Device. *Journal of Physics: Conference Series*, 227:012014, May 2010.

[92] T Notake, T Saito, Y Tatematsu, S Kubo, T Shimozuma, K Tanaka, M Nishiura, A Fujii, La Agusu, I Ogawa, and T Idehara. Subterahertz gyrotron developments for collective Thomson scattering in LHD. *The Review of scientific instruments*, 79(10):10E732, October 2008.

[93] E Westerhof, J W Oosterbeek, M De Baar, M A van den Berg, W Bongers, A Bürger, M F Graswinckel, R Heidinger, B Hennen, J A Hoekzema, S B Korsholm, O G Kruijt, B Lamers, F Leipold, S K Nielsen, D Thoen, B C E Vaessen, and P M Wortman. The TEXTOR line-of sight ECE system for feedback controlled ECRH power deposition. In *35th EPS Conference on Plasma Physics*, page P1.081, Hersonissos, 2008.

[94] E Gusakov and A Popov. Low Threshold Parametric Decay Backscattering Instability in Tokamak Electron Cyclotron Resonance Heating Experiments. *Physical Review Letters*, 105(11):115003, September 2010.

[95] E Westerhof, S K Nielsen, J Oosterbeek, M Salewski, M De Baar, W Bongers, A Bürger, B Hennen, S B Korsholm, F Leipold, D Moseev, M Stejner, and D Thoen. Strong Scattering of High Power Millimeter Waves in Tokamak Plasmas with Tearing Modes. *Physical Review Letters*, 103(12):125001, September 2009.

[96] R White, P Rutherford, P Colestock, and M Bussac. Sawtooth Stabilization by Energetic Trapped Particles. *Physical Review Letters*, 60(20):2038–2041, May 1988.

[97] M Zabiego, X Garbet, A Becoulet, F Nguyen, and B Saoutic. Sawtooth stabilization with on-axis ICRH on Tore Supra. *Nuclear Fusion*, 34(11):1489–1495, November 1994.

[98] H Kimura, T Fujii, M Saigusa, S Moriyama, M Sato, M Nemoto, T Kondoh, and K Hamamatsu. Recent ion cyclotron range of frequencies experiments in JT-60U. *Fusion Engineering and Design*, 26(1-4):95–102, January 1995.

[99] Deng Zhou, Shaojie Wang, and Cheng Zhang. Sawtooth stabilization by barely trapped energetic electrons. *Physics of Plasmas*, 12(6):062512, June 2005.

[100] I T Chapman, S D Pinches, J P Graves, R J Akers, L C Appel, R V Budny, S Coda, N J Conway, M de Bock, L-G Eriksson, R J Hastie, T C Hender, G T A Huysmans, T Johnson, H R Koslowski, A Krämer-Flecken, M Lennholm, Y Liang, S Saarelma, S E Sharapov, and I Voitsekhovitch. The physics of sawtooth stabilization. *Plasma Physics and Controlled Fusion*, 49(12B):B385–B394, December 2007.

[101] I T Chapman, V G Igochine, J P Graves, S D Pinches, A Gude, I Jenkins, M Maraschek, and G Tardini. Sawtooth control and the interaction of energetic particles. *Nuclear Fusion*, 49(3):035006, March 2009.

[102] I T Chapman, S D Pinches, H R Koslowski, Y Liang, A Krämer-Flecken, and M de Bock. Sawtooth stability in neutral beam heated plasmas in TEXTOR. *Nuclear Fusion*, 48(3):035004, March 2008.

[103] S B Korsholm, M Stejner, H Bindslev, V Furtula, F Leipold, F Meo, P K Michelsen, D Moseev, S K Nielsen, M Salewski, M de Baar, E Delabie, M Kantor, and A Bürger. Measurements of Intrinsic Ion Bernstein Waves in a Tokamak by Collective Thomson Scattering. *Physical Review Letters*, 106(16), April 2011.

[104] M Stejner, S K Nielsen, H Bindslev, S B Korsholm, and M Salewski. Principles of fuel ion ratio measurements in fusion plasmas by collective Thomson scattering. *Plasma Physics and Controlled Fusion*, 53(6):065020, June 2011.

[105] M Stejner, S B Korsholm, S K Nielsen, M Salewski, H Bindslev, S Brezinsek, V Furtula, F Leipold, P K Michelsen, F Meo, D Moseev, A Bürger, M Kantor, and M de Baar. Measurements of plasma composition in the TEXTOR tokamak by collective Thomson scattering. *Plasma Physics and Controlled Fusion*, 54(1):015008, January 2012.

[106] M Salewski, L-G Eriksson, H Bindslev, S B Korsholm, F Leipold, F Meo, P K Michelsen, and S K Nielsen. Impact of ICRH on the measurement of fusion alphas by collective Thomson scattering in ITER. *Nuclear Fusion*, 49(2):025006, February 2009.

[107] M Salewski, O Asunta, L-G Eriksson, H Bindslev, V Hynönen, S B Korsholm, T Kurki-Suonio, F Leipold, F Meo, P K Michelsen, S K Nielsen, and J Roenby. Comparison of collective Thomson scattering signals due to fast ions in ITER scenarios with fusion and auxiliary heating. *Plasma Physics and Controlled Fusion*, 51(3):035006, March 2009.

[108] J A Heikkinen and S K Sipila. Power transfer and current generation of fast ions with large-kθ waves in tokamak plasmas. *Physics of Plasmas*, 2(10):3724, 1995.

[109] T Kurki-Suonio, O Asunta, T Hellsten, V Hynönen, T Johnson, T Koskela, J Lönnroth, V Parail, M Roccella, G Saibene, A Salmi, and S Sipilä. ASCOT simulations of fast ion power loads to the plasma-facing components in ITER. *Nuclear Fusion*, 49(9):095001, September 2009.

[110] O Fischer, W A Cooper, M Yu Isaev, and L Villard. Neoclassical transport and α particle confinement in novel 3-D reactor systems. *Nuclear Fusion*, 42(7):817–826, July 2002.

[111] M Kantor, A J H Donne, R Jaspers, and H J van der Meiden. Thomson scattering system on the TEXTOR tokamak using a multi-pass laser beam configuration. *Plasma Physics and Controlled Fusion*, 51(5):055002, May 2009.

[112] Xin Tao, Anthony A Chan, and Alain J Brizard. Hamiltonian theory of adiabatic motion of relativistic charged particles. *Physics of Plasmas*, 14(9):092107, September 2007.

[113] Allen H Boozer and Gioietta Kuo Petravic. Monte Carlo evaluation of transport coefficients. *Physics of Fluids*, 24(5):851, 1981.

[114] S Suzuki, T Shirai, M Nemoto, K Tobita, H Kubo, T Sugie, A Sakasai, and Y Kusama. Attenuation of high-energy neutral hydrogen beams in high-density plasmas. *Plasma Physics and Controlled Fusion*, 40(12):2097, 1998.

[115] M Albergante, J P Graves, A Fasoli, M Jucker, X Lapillonne, and W A Cooper. Numerical modelling of electromagnetic turbulent transport of energetic ions in burning plasmas. *Plasma Physics and Controlled Fusion*, 53(5):054002, 2011.

[116] G A Cooper, M Jucker, W A Cooper, J P Graves, and M Yu Isaev. Exact canonical drift Hamiltonian formalism with pressure anisotropy and finite perturbed fields. *Physics of Plasmas*, 14(10):102506, October 2007.

[117] H P Zehrfeld. Resistive equilibrium states of axisymmetric plasmas with compressible viscous fluid flow. In *26th EPS Conf. on Contr. Fusion and Plasma Physics*, volume 23, pages 1421 – 1424, Maastricht, 1999.

[118] H Zohm. Edge localized modes (ELMs), 1996.

[119] T E Evans, R A Moyer, K H Burrell, M E Fenstermacher, I Joseph, A W Leonard, T H Osborne, G D Porter, M J Schaffer, P B Snyder, P R Thomas, J G Watkins, and W P West. Edge stability and transport control with resonant magnetic perturbations in collisionless tokamak plasmas. *Nature Physics*, 2(6):419–423, May 2006.

[120] M Mori. Overview of the recent experimental results in JT-60 and JFT-2M. *Plasma Physics and Controlled Fusion*, 36(7A):A39, 1994.

[121] Y Liang, H R Koslowski, P Thomas, E Nardon, B Alper, P Andrew, Y Andrew, G Arnoux, Y Baranov, M Bécoulet, M Beurskens, T Biewer, M Bigi, K Crombe, E De La Luna, P de Vries, W Fundamenski, S Gerasimov, C Giroud, M P Gryaznevich, N C Hawkes, S Hotchin, D F Howell, S Jachmich, V Kiptily, L Moreira, V Parail, S Pinches, E Rachlew, and O Zimmermann. Active Control of Type-I Edge-Localized Modes with n=1 Perturbation Fields in the JET Tokamak. *Physical Review Letters*, 98(26), June 2007.

[122] O Schmitz, M W Jakubowski, H Frerichs, D Harting, M Lehnen, B Unterberg, S S Abduallaev, S Brezinsek, I G J Classen, T Evans, Y Feng, K H Finken, M Kantor, D Reiter, U Samm, B Schweer, G Sergienko, G W Spakman, M Tokar, E Uzgel, and R C Wolf. Identification and analysis of transport domains in the stochastic boundary of TEXTOR-DED for different mode spectra. *Nuclear Fusion*, 48(2):024009, February 2008.

[123] K Shinohara, T Kurki-Suonio, D Spong, O Asunta, K Tani, E Strumberger, S Briguglio, T Koskela, G Vlad, S Günter, G J Kramer, S Putvinski, and K Hamamatsu. Effects of complex symmetry-breakings on alpha particle power loads on first wall structures and equilibrium in ITER. *Nuclear Fusion*, 51(6):063028, June 2011.

[124] H R Koslowski, Y Liang, A Krämer-Flecken, K Löwenbrück, M von Hellermann, E Westerhof, R C Wolf, and O Zimmermann. Dependence of the threshold for perturbation field generated m / n = 2/1 tearing modes on the plasma fluid rotation. *Nuclear Fusion*, 46(8):L1–L5, August 2006.

[125] O Schmitz, J W Coenen, H Frerichs, M Kantor, M Lehnen, B Unterberg, S Brezinsek, M Clever, T Evans, and K H Finken. Particle confinement control with resonant magnetic perturbations at TEXTOR. *Journal of Nuclear Materials*, 390-391:330–334, June 2009.

[126] Q Yu and S Günter. Effect of resonant magnetic perturbations on particle confinement. *Nuclear Fusion*, 49(6):062001, June 2009.

[127] S Cauffman and R Majeski. Ion cyclotron emission on the Tokamak Fusion Test Reactor. *Review of Scientific Instruments*, 66(1):817, 1995.

[128] S Cauffman, R Majeski, K G McClements, and R O Dendy. Alfvenic behaviour of alpha particle driven ion cyclotron emission in TFTR. *Nuclear Fusion*, 35(12):1597–1602, December 1995.

[129] J Strachan, H Adler, P Alling, C Ancher, H Anderson, J Anderson, D Ashcroft, Cris Barnes, G Barnes, S Batha, M Bell, R Bell,

M Bitter, W Blanchard, N L Bretz, R V Budny, C Bush, R Camp, M Caorlin, S Cauffman, Z Chang, C Cheng, J Collins, G Coward, D S Darrow, J DeLooper, H Duong, L Dudek, R Durst, P Efthimion, D Ernst, R Fisher, R Fonck, E Fredrickson, N Fromm, G Fu, H Furth, C Gentile, N N Gorelenkov, B Grek, L Grisham, G Hammett, G Hanson, R Hawryluk, W W Heidbrink, H W Herrmann, K Hill, J Hosea, H Hsuan, A Janos, D Jassby, F Jobes, D Johnson, L Johnson, J Kamperschroer, H Kugel, N Lam, P LaMarche, M Loughlin, B LeBlanc, M Leonard, F Levinton, J Machuzak, D Mansfield, A Martin, E Mazzucato, R Majeski, E Marmar, J McChesney, B McCormack, D McCune, K McGuire, G McKee, D Meade, S Medley, D Mikkelsen, D Mueller, Murakami, A Nagy, R Nazikian, R Newman, T Nishitani, M Norris, T OConnor, M Oldaker, M Osakabe, D Owens, H K Park, W Park, S Paul, G Pearson, E Perry, M Petrov, C Phillips, S Pitcher, A Ramsey, D Rasmussen, M Redi, D Roberts, J Rogers, R Rossmassler, A Roquemore, E Ruskov, S Sabbagh, M Sasao, G Schilling, J Schivell, G Schmidt, S Scott, R Sissingh, C Skinner, J Snipes, J Stevens, T Stevenson, B Stratton, E Synakowski, W Tang, G Taylor, J Terry, M Thompson, M Tuszewski, C Vannoy, A von Halle, S von Goeler, D Voorhees, R Walters, R Wieland, J Wilgen, M Williams, J Wilson, K Wong, G Wurden, M Yamada, K Young, M Zarnstorff, and S Zweben. Fusion power production from TFTR plasmas fueled with deuterium and tritium. *Physical Review Letters*, 72(22):3526–3529, May 1994.

[130] G A Cottrell, V P Bhatnagar, O Da Costa, R O Dendy, J Jacquinot, K G McClements, D C McCune, M F F Nave, P Smeulders, and D F H Start. Ion cyclotron emission measurements during JET deuterium-tritium experiments. *Nuclear Fusion*, 33(9):1365–1387, September 1993.

[131] G A Cottrell and R O Dendy. Superthermal Radiation from Fusion Products in JET. *Physical Review Letters*, 60(1):33–36, 1988.

[132] K G McClements, C Hunt, R O Dendy, and G Cottrell. Ion Cyclotron Emission from JET D-T Plasmas. *Physical Review Letters*, 82(10):2099–2102, 1999.

[133] M Ichimura, H Higaki, S Kakimoto, Y Yamaguchi, K Nemoto, M Katano, M Ishikawa, S Moriyama, and T Suzuki. Observation of spontaneously excited waves in the ion cyclotron frequency range on JT-60U. *Nuclear Fusion*, 48(3):35012, 2008.

[134] A G Shalashov, E V Suvorov, L V Lubyako, and H Maassberg. NBI-driven ion cyclotron instabilities at the W7-AS stellarator. *Plasma Physics and Controlled Fusion*, 45(4):395–412, April 2003.

[135] E V Suvorov, E Holzhauer, W Kasparek, A B Burov, Y A Dryagin, S E Fil'chenkov, A A Fraiman, L V Lubyako, D A Ryndyk, N K Skalyga, O B Smolyakova, V Erckmann, T Geist, M Kick, and N Rust. Lower hybrid turbulence excited by a fast transverse ion beam in a magnetized plasma. *Nuclear Fusion*, 38(5):661–671, 1998.

[136] R O Dendy, K G McClements, C N Lashmore-Davies, G A Cottrell, R Majeski, and S Cauffman. Ion cyclotron emission due to collective instability of fusion products and beam ions in TFTR and JET. *Nuclear Fusion*, 35(12):1733–1742, December 1995.

[137] R O Dendy, K G McClements, C N Lashmore-Davies, R Majeski, and S Cauffman. A mechanism for beam-driven excitation of ion cyclotron harmonic waves in the Tokamak Fusion Test Reactor. *Physics of Plasmas*, 1(10):3407, 1994.

[138] R O Dendy. Interpretation of ion cyclotron emission from fusion and space plasmas. *Plasma Physics and Controlled Fusion*, 36(12), 1994.

[139] T Fulop, Ya I Kolesnichenko, M Lisak, and D Anderson. Origin of superthermal ion cyclotron emission in tokamaks. *Nuclear Fusion*, 37(9):1281–1293, September 1997.

[140] R O Dendy, C N Lashmore-Davies, K G McClements, and G A Cottrell. The excitation of obliquely propagating fast Alfven waves at fusion ion cyclotron harmonics. *Physics of Plasmas*, 1(6):1918, 1994.

[141] K G McClements, R O Dendy, C N Lashmore-Davies, G A Cottrell, S Cauffman, and R Majeski. Interpretation of ion cyclotron emission from sub-Alfvenic fusion products in the Tokamak Fusion Test Reactor. *Physics of Plasmas*, 3(2):543, 1996.

[142] A A Listopad, J W Coenen, V I Davydenko, P P Deichuli, A A Ivanov, V V Mishagin, V Ya Savkin, W Schalt, B Schweer, G I Shulzhenko, N V Stupishin, and R Uhlemann. Operation and upgrade of diagnostic neutral beam injector RUDI at TEXTOR tokamak. *The Review of scientific instruments*, 81(2):02B104, February 2010.

[143] V G Igochine, I T Chapman, V Bobkov, S Günter, M Maraschek, D Moseev, G Pereversev, M Reich, and J Stober. Destabilization of fast particle stabilized sawteeth in ASDEX Upgrade with electron cyclotron current drive. *Plasma Physics and Controlled Fusion*, 53(2):022002, February 2011.

[144] O Sauter, E Westerhof, M-L Mayoral, B Alper, P A Belo, R J Buttery, A Gondhalekar, T Hellsten, T C Hender, D F Howell, T Johnson, P Lamalle, M J Mantsinen, F Milani, M F F Nave, F Nguyen, A L

Pecquet, S D Pinches, S Podda, and J Rapp. Control of Neoclassical Tearing Modes by Sawtooth Control. *Phys. Rev. Lett.*, 88(10):105001, February 2002.

[145] J P Graves, I T Chapman, S Coda, T Johnson, M Lennholm, B Alper, M de Baar, K Crombe, L-G Eriksson, R Felton, D F Howell, V Kiptily, H R Koslowski, M-L Mayoral, I Monakhov, I Nunes, and S D Pinches. Experimental verification of sawtooth control by energetic particles in ion cyclotron resonance heated JET tokamak plasmas. *Nuclear Fusion*, 50(5):052002, May 2010.

[146] M Lennholm, L-G Eriksson, F Turco, F Bouquey, C Darbos, R Dumont, G Giruzzi, M Jung, R Lambert, R Magne, D Molina, P Moreau, F Rimini, J-L Segui, S Song, and E Traisnel. Demonstration of Effective Control of Fast-Ion-Stabilized Sawteeth by Electron-Cyclotron Current Drive. *Physical Review Letters*, 102(11):100–103, March 2009.

[147] D Wagner, J Stober, S Baumel, T Franke, F Leuterer, E Poli, F Monaco, M Munich, H Schutz, H Zohm, M Thumm, T Scherer, A Meier, G Gantenbein, J Flamm, W Kasparek, C Lechte, H Hohnle, A G Litvak, G G Denisov, A Cirkov, L G Popov, V O Nichiporenko, V E Myasnikov, E M Tai, E A Solyanova, and S A Malygin. Multi-frequency ECRH system at ASDEX upgrade. In *2009 34th International Conference on Infrared, Millimeter, and Terahertz Waves*, pages 1–2. IEEE, September 2009.

[148] F Leuterer. Plans for a new ECRH system at ASDEX upgrade. *Fusion Engineering and Design*, 66-68:537–542, September 2003.

[149] R Neu, R Dux, A Geier, A Kallenbach, R Pugno, V Rohde, D Bolshukhin, J C Fuchs, O Gehre, O Gruber, J Hobirk, M Kaufmann, K Krieger, M Laux, C Maggi, H Murmann, J Neuhauser, F Ryter, A C C Sips, A Stäbler, J Stober, W Suttrop, and H Zohm. Impurity behaviour in the ASDEX Upgrade divertor tokamak with large area tungsten walls. *Plasma Physics and Controlled Fusion*, 44(6):811–826, June 2002.

[150] R O Dendy, R J Hastie, K G McClements, and T J Martin. A model for ideal m=1 internal kink stabilization by minority ion cyclotron resonant heating. *Physics of Plasmas*, 2(5):1623, 1995.

[151] I T Chapman, V G Igochine, J P Graves, S D Pinches, A Gude, I Jenkins, M Maraschek, and G Tardini. Sawtooth control and the interaction of energetic particles. *Nuclear Fusion*, 49(3):035006, March 2009.

Risø DTU is the National Laboratory for Sustainable Energy. Our research focuses on development of energy technologies and systems with minimal effect on climate, and contributes to innovation, education and policy. Risø has large experimental facilities and interdisciplinary research environments, and includes the national centre for nuclear technologies.

Risø DTU
National Laboratory for Sustainable Energy
Technical University of Denmark

Frederiksborgvej 399
PO Box 49
DK-4000 Roskilde
Denmark
Phone +45 4677 4677
Fax +45 4677 5688

www.risoe.dtu.dk

Report number Risø-PhD-91